Solvo-hydrothermal growth and photoluminescence studies of micro and nano structured Zinc Sulfide for bio-imaging applications

Thesis submitted to

COCHIN UNIVERSITY OF SCIENCE AND TECHNOLOGY

in partial fulfillment of the requirements

for the award of the degree of

DOCTOR OF PHILOSOPHY

in

Physics

by

Sajan P.

Nano Functional Materials Lab
Department of Physics
Cochin University of Science and Technology
Cochin - 682 022, Kerala, India

June 2016

Solvo-hydrothermal growth and photoluminescence studies of micro and nano structured Zinc Sulfide for bio-imaging applications

Ph.D. thesis in the field of Physics

Author:

Sajan P.
Nano Functional Materials Lab
Department of Physics
Cochin University of Science and Technology
Cochin - 682 022, Kerala, India.
Email: sajanp33@gmail.com

Supervisor:

Dr. M. Junaid Bushiri
Professor
Nano Functional Materials Lab
Department of Physics
Cochin University of Science and Technology
Cochin-682 022, Kerala, India.
Email: junaidbushiri@cusat.ac.in

June 2016

Dedicated to my mother

Department of Physics
Cochin University of Science and Technology
Cochin - 682 022

Dr. M. Junaid Bushiri
Professor
Department of Physics
Cochin University of Science and Technology
Cochin 682 022, India.

Certificate

*Certified that the work presented in this thesis entitled "**Solvo-hydrothermal growth and photoluminescence studies of micro and nano structured Zinc Sulfide for bio-imaging applications**" is based on the bonafide record of research work done by Sajan P., under my guidance in the Department of Physics, Cochin University of Science and Technology, Cochin 682 022 in partial fulfillment of the requirements for the award of degree of Doctor of Philosophy and has not been included in any other thesis submitted for the award of any degree. All the relevant corrections and modifications suggested by the audience during the pre-synopsis seminar and recommendations by doctoral committee of the candidate have been incorporated in the thesis.*

Cochin-22
Date:15/06/2016

Dr. M. Junaid Bushiri
(Supervising Guide)

Phone: +91-4842577404 Fax: 91 484 2577595, Email: junaidbushiri@cusat.ac.in

Declaration

*Certified that the work presented in this thesis entitled "**Solvo-hydrothermal growth and photoluminescence studies of micro and nano structured Zinc Sulfide for bio-imaging applications**" is based on the original work done by me under the guidance of Dr. M. Junaid Bushiri, Professor, Department of Physics, CUSAT, Cochin-22 and has not been included in any other thesis submitted previously for the award of any other degree.*

Cochin – 22 **Sajan P.**

Date:15/06/2016

Acknowledgements

At this particular juncture, when I look back with full of memories, I could realize that there are too many peoples to thank for their unconditional love and help. This thesis will not be completed without their support and help. It is a pleasant task and I use this occasion to express my thanks to all my teachers and friends from my school days onwards.

First and foremost, I obliged to Prof. M. Junaid Bushiri, my supervising guide and teacher for his valuable advice, help and support throughout the research period. He was always ready to hear me, discuss with the research problems and share new ideas. I also thank him for his help and support.

I express my sincere thanks to Prof. S. Jayalekshmi, Head, Department of Physics CUSAT, and all the former heads- Prof. B. Pradeep, Prof. M. R. Anantharaman for providing and permitting me to use the research facilities in the department. I sincerely thank Prof. M. R. Anantharaman, my Doctoral committee member, for all his support, advice and help. I express my gratitude to all the teachers and non-teaching staff in Department of Physics CUSAT, for their help and support.

It is my pleasure and proud to thank my mentor Mr. Joseph Sir, Teacher St. Mary's A U P School Mamankara for his cares and support. I would like to thank Sebastian Sir, Madhusoodanan and Eliamma teacher for their support during my school days.

I am obliged to Prof. M. K. Jayaraj, Professor, Department of Physics CUSAT and Department of Physics, Madurai Kamaraj University, Tamilnadu for allowing me to take the Raman and PL measurements.

I thank Dr. Shibu M Eappen and Mr. Melbin SAIF STIC CUSAT for SEM measurements. I would like to thank S. Agouram, Departamento de Fisica Aplicada y Electromagnetismo, Universitat de, Valencia, C/Dr Moliner 50

Burjassot, Valencia 46100, Spain, SAIF IIT Madras, and TEM facility at School of Pure and Applied Physics, MG University Kottayam for TEM measurements.

Words are not enough to thank Dr. R. S. Jayasree, Scientist, Biophotonics and Imaging Laboratory Biomedical Technology Wing, Sree Chitra Tirunal Institute for Medical Sciences & Technology, Poojappura, Thiruvananthapuram for bio-imaging studies of the samples.

I acknowledge University Grants Commission India for providing Rajiv Gandhi National Fellowship during the research period.

The research at my lab, Nano Functional Materials Lab was unforgettable moments and I thank my lab members Bini, Shajira, Vinod, Ganesh, Satheesh, Rasheed, Sagar, Beena, M Phil and M Sc project students for their help and support. I thank all my school, B. Sc, M. Sc classmates, seniors, friends from other labs of the department and Bro Bro team members (Jubeesh, Abhi, Navaneeth, Shijeesh, Anand, Santhu, Deepu, Aravind, Titu, Manoj, Anshad, Jishnu, Dinto, Sreejith, Kurias, Abhay, Manu) for making a joyful life at CUSAT.

I have no words to express my gratitude and feelings towards my Amma for her unconditional love, caring and support throughout my life. I thank all my family members for their help and support.

Finally I thank all my well-wishers and friends who have supported me.

Sajan. P

Contents

List of Figures

Preface

The research on nanocrystalline materials have been of great interest for more than 20 years due to its fundamental properties as well as development of technology based on it. Non-toxic semiconducting nanocrystals are important materials with wide range of applications in the areas of biotechnology, medicine, bio-optics and for the fabrication light emitting and harvesting devices. Majority of the II-VI semiconductors possess wide band gap along with high iconicity and are important materials for optoelectronic devices operating under the UV excitation sources. Among the II-VI semiconductors, ZnS is a material with good optical transmission in the visible region with large exciton binding energy of about 40 meV. ZnS usually crystallizes in cubic form which is zinc blende or sphalerite and its hexagonal form is in wurtzite phase. The cubic sphalerite phase of ZnS has a band gap of 3.68 eV whereas the hexagonal (wurtzite) phase has a band gap of 3.77 eV. Moreover, ZnS is a good host lattice phosphor for photonic applications and electroluminescent devices because of its wide band gap.

The present thesis deals with the synthesis and photoluminescence studies of micro and nanostructured ZnS by hydrothermal and solvo-hydrothermal method. Thesis is also focused on bioimaging application of these materials.

Chapter 1 deals with the basic introduction about semiconductor nanomaterials; its properties, applications, and photoluminescence studies. The fundamental properties and applications of ZnS are also described in this chapter. Literature review in the present area of interest and the motivation behind the present work is also incorporated in the chapter 1. A detailed description of the hydrothermal and solvo-hydrothermal (S-H) synthesis method and the characterization techniques used for the present study are included in the **Chapter 2.** Chapter 2 also discusses the basic working principle of various characterization tools used in the present work.

Chapter 3 briefly discusses the growth of cubic ZnS particles by hydrothermal and solvo-hydrothermal method. This chapter gives the importance of solvo-hydrothermal growth process for synthesizing defect free luminescent ZnS particles. Relatively oxygen free mesoporous cubic ZnS particles are synthesized via facile solvo-hydrothermal route using water-acetonitrile combination. Boosted UV emission at 349 nm is observed from the ZnS prepared by solvo-hydrothermal route. The increased intensity of this UV emission is attributed to activation of whispering gallery modes (WGM) of elliptical microstructures made of porous nanostructures.

Chapter 4 deals with the luminescence properties of hydrothermally and solvo-hydrothermally (water-acetonitrile) grown Mn doped ZnS at a reaction temperature of 200 ^{0}C. The photoluminescence (PL) emission intensity of solvo-hydrothermally grown Mn doped ZnS shows high luminescence intensity as compared to that of grown by hydrothermal method. ZnS:Mn (3wt%) grown by S-H method exhibit high luminescence yield at yellow-orange region and at 367 nm, is contributed to the increase of sulphur vacancy population and the increase in specific area of grain boundary. The chromaticity coordinates (CIE) of the observed yellow-orange emission from the samples are calculated, which fall in the yellow-orange region.

The effect of surfactants like cetyl trimethylammonium bromide (CTAB), ethylenediamine (EDA), polyethylene glycol (PEG) and polymethyl methacrylate (PMMA) on the solvo-hydrothermal growth properties are described in the **Chapter 5.** Among these, ZnS microspheres with an average diameter of 3.85 μm are grown by solvo-hydrothermal (S-H) method using water-acetonitrile-ethylenediamine (EDA) solution combination. These ZnS microspheres are characterized by using XRD, SEM, HRTEM, FT-RAMAN, FTIR and PL. An intense Raman band at 257 cm^{-1} was seen from the ZnS microspheres attributed to the increase in carrier concentration which in turn leads to broad PL emission from 380-580 nm.

Chapter 6 describes the ethylenediamine assisted solvo-hydrothermal growth of ZnS:Nd_2O_3 host-guest system. The XRD analysis of the samples shows the presence of mixed phase consists of wurtzite ZnS and Nd_2O_3. The formation of wurtzite phase ZnS in neodymium added samples are attributed to the presence of neodymium acetate and ethylenediamine in the growth medium. The EDAX spectra show the presence of Nd ions in ZnS:Nd_2O_3 samples. The SEM images show that majority of the particles are having spherical morphology. PL spectra show broad blue emission centered at 485 nm (Nd 3 wt%), 490 nm (Nd 4 wt%) and 470 nm (Nd 5 wt%) while exciting the sample with UV radiation at 325 nm. The Nd 4 and 5 wt% added samples shows characteristic intense Nd related emission peaks at 860-905 nm ($^4F_{3/2}$ to $^4I_{9/2}$ transition) and very feeble emission at 1054 and 1071 nm ($^4F_{3/2}$ to $^4I_{11/2}$ transition) with an excitation of 785 nm. The observed excitation dependent Nd related intense emission confirms that the Nd ions are incorporated in to the ZnS host matrix.

The investigations on biocompatibility and imaging efficiency of ethylenediamine assisted solvo-hydrothermally grown ZnS microspheres and solvo-hydrothermally grown Mn doped ZnS nanoparticles are given in **Chapter 7.** This studies reveals that the cytocompatibility and haemocompatibility of ZnS microspheres and ZnS nanoparticles, which can be used for bioimaging applications.

The overall summary of the work and the future scope of the present study are briefly described in **Chapter 8**.

List of Publications

Journal papers.

1) **P. Sajan**, Junaid M. Bushiri, R. Vinod, Appl. Phys. A, **113,** 321 (2013) "Boosted UV emission at 349 nm from mesoporous ZnS" (Included in this thesis).

2) **P. Sajan**, R.Vinod and M. Junaid Bushiri, J Lumin., **158,** 110 (2015). "High luminescent yield from Mn doped ZnS at yellow-orange region and 367 nm" (Included in this thesis).

3) **P. Sajan**, R. S. Jayasree, S. Agouram and M. Junaid Bushiri, Luminescence, **31,** 544 (2016). "Synthesis of cubic ZnS microspheres exhibiting broad visible emission for bioimaging applications" (Included in this thesis).

4) R. Vinod, **P. Sajan**, Sreekumar Rajappan Achary, Carmen Martinez Tomas, Vicente Muñoz-Sanjosé and M Junaid Bushiri, J. Phys. D: Appl. Phys. **45**, 425103 (2013). "Enhanced UV emission from ZnO nanoflowers synthesized by the hydrothermal process",

5) R. Vinod, M. Junaid Bushiri, **P. Sajan**, Sreekumar Rajappan Achary and Vicente Muñoz-Sanjosé, Phys. Status Solidi A, **211** (5), 1155 (2014). "Mn^{2+}-induced room-temperature ferromagnetism and spin-glass behavior in hydrothermally grown Mn-doped ZnO nanorods".

Conference papers

1) "Optical studies of nanocrystalline ZnS grown by hydrothermal method", **P. Sajan**, R. Vinod and M. Junaid Bushiri, The second international conference on optoelectronic materials and thin film for advanced technology (OMTAT-2013), January 3-5 2013, CUSAT, Kochi (Included in this thesis).

2) "Grain size engineering of ZnS quantum dots prepared via molarity variation by chemical method", **P. Sajan**, R. Vinod, K.R. Nithinraj and M. Junaid Bushiri, National conference- NANO INDIA 2013, February 19-20, 2013.CSIR-NIIST Trivandrum,

3) "Optical properties of ZnS quantum dots synthesized by hydrothermal method at a reaction temperature of 200 ^{0}C", (Oral Presentation), P. **Sajan**, R.Vinod and M. Junaid Bushiri, National Conference on Recent Trends in Electronics and Instrumentation, NCRTEI-2013, September 20-21, 2013, Bharathiar University, Coimbatore.

4) "Synthesis and characterization of Mn doped ZnS Nanostructures", **P. Sajan**, R. Vinod and M. Junaid Bushiri, 26th Kerala Science Congress, January 28-31, 2014, Kerala Veterinary and Animal Sciences University, Pookode, Wayanad,

5) "Hydrothermal growth of Manganese Oxide nanostructures", **P. Sajan**, R. Vinod, and M. Junaid Bushiri, National Symposium on Advances in Material Science and Technology (AMST-2012), February 03-04, 2012, Gujarat University, Ahmedabad, Gujarat.

6) "Synthesis of flower like ZnO nanorods", R. Vinod, **P. Sajan** and M. Junaid Bushiri, National Symposium on Advances in Material Science and Technology (AMST-2012), February 03-04, 2012, Gujarat University, Ahmedabad, Gujarat.

7) "Photoluminescence and Raman studies of Mn doped ZnO nanorods", R. Vinod, **P.** Sajan and M. Junaid Bushiri, The second international conference on optoelectronic materials and thin film for advanced technology (OMTAT-2013), January 3-5 2013, CUSAT, Kochi.

8) "Optical studies of Ni doped ZnO nanoflowers", R. Vinod, **P. Sajan** and M. Junaid Bushiri, National conference on Innovative trends in Material Science (ITMS-2013), August 23-24, 2013, Arignar Anna College, Nagarcoil, Tamil Nadu.

1 Basics of Nanoscience and Nanotechnology

Chapter

1.1. Introduction

Nanoscience is one of the important branch of study emerged at the end of 20^{th} century. It is a promising branch of study for the development of miniature technology for the wellbeing of humanity in future. Nanotechnology is based on controlling matter at small scale especially at atomic or molecular dimension. The application of nanoscience and technology spans in different areas, it includes chemistry, biology, and physics, etc [Porter A L *et al*; 2009]. Nano is a Greek word which means 'dwarf' or small. In metric system it means 10^{-9} or one billionth of a meter [Buzea C *et al*; 2007]. The engineering of materials at the atomic level mainly from 1-100 nm range is termed as "nanotechnology" and materials within this range are called "nanomaterials" [Mansoori G A *et al*; 2005]. Study of materials at nanoscale can explore many unbelievable things in comparison with its bulk state. Nanoscience and nanotechnology includes the synthesis, characterization, and the applications of nanostructured materials. The developments and the emergence of new fields like quantum

physics and soft condensed matter physics gave a new dimension to the wide area of materials science. Similar to quantum mechanics, on nanometer scale, materials or structures may have new physical properties or exhibit new physical phenomena. For example, semiconductors band gap can be varied by controlling the material dimension [Smith A M *et al*; 2010]. Another very important consequence of nanotechnology is the miniaturization of electronic devices and machines in displays, biosensors and metal based nanoparticles etc. Nanomachines and nanorobots find its place in different modern equipments as well as for the treatment of different ailments. Nanomaterials are also used in cosmetics, and sunscreens etc. The semiconductor nanocrystals (i.e., quantum dots) are rapidly emerging with wide application in biotechnology, medicine, optics, and will require the same attention with respect to their toxicity [Bera D *et al*; 2010]. The use of nanomaterials in the medical field has started even before 1980's. Gold nanoparticles are such materials that widely used in medical field [Dykman L A *et al*; 2011].

1.2. Properties of Nanomaterials

1.2.1. Mechanical Properties

Mechanical properties like hardness, toughness, fatigue strength and elastic modulus etc are entirely different in the nanoregime compared to its bulk counterparts. The mechanical properties of the material can be improved by making the materials to nanoscale. The improved mechanical properties of materials find tremendous applications in sensors, high strength materials with light weight, probe tips for various microscopes, cutting tools etc [Stanislaus S W *et al;* 1998]. Among these, carbon nanotubes are well known to us because of its improved mechanical

properties, high strength and strain. Super hard nanocomposites synthesized by borides or nitrides exhibits very good mechanical properties and have many applications [Veprek S *et al;* 2001]. Recently polymer based nanocomposites and polymer fillers attained much more interest due to its enhanced mechanical properties. In nanoregime, crystal perfection is comparatively high because the reduction in size of the material contributed to reduce the chance of imperfection like dislocation and impurities. Impurities or imperfections in the nanoscaled materials can be removed to certain extent upon annealing or purifying. These imperfections will mobile to surface, resulting perfect material structure. These nanomaterials are defect free compared to its bulk form and possess enhanced mechanical properties [Cao G; 2004, Herring C *et al;* 1952].

1.2.2. Thermal properties

Thermal properties of nanostructured materials expected to be different from that of its bulk counterparts similar to its mechanical properties. Physical properties of materials like optical, electrical, magnetic and mechanical properties of nanomaterilas are widely investigated by researchers in the past. But thermal properties of nanostructured materials are limited because of practical difficulties involve in measuring the thermal properties. It is particularly difficult to experimentally measure and control thermal transport in nanoscale dimensions. Recently thermal transport properties and thermally induced chemical reactions of nanomaterials are analyzed by applying thermophysical and thermoanalytical methods [Sagadevan S *et al;* 2014]. The thermal energy applications of nanomaterials were examined by studying its thermal conductivity and thermophysical properties [Taylori R *et al;* 2012, Kandlikar S G *et al;* 2012, Mahian O *et al;* 2013, Sureshkumar R *et al;* 2013, Barber J *et al;* 2011 and

Fan J *et al;* 2011]. The thermal properties of the nanomaterials depend on factors like material size, shape, chemical compositions and the large interfaces. In the case of nanomaterials, thermal properties are mostly related to the phonon transport, with respect to the reduction in size to nanomaterials phonon confinement may occur. The physical phenomena of phonon confinement in nanomaterials lead to modifications in its thermal properties.

1.2.3. Magnetic Properties

The size reduction of materials results in large surface to volume ratio which in turn contributes to evolution of variation in magnetic properties due to magnetic coupling of neighboring atoms. Magnetic properties of nanomaterials find applications in the fields of imaging, magnetic memory storage devices, refrigeration, magnetic read head devices and so on. The magnetism in gold and platinum nanoparticles, ferromagnetism in Au nanoparticles, and giant magnetoresistance in ferromagnets etc are some of the interesting examples of nanomagnetism. It was reported that the magnetic anisotropy as well as the magnetic moment per atom, the Curie (T_C) or Néel (T_N) temperatures and the coercivity field (H_C) of nanoparticles different from its bulk state [Issa B *et al;* 2013]. The metal based (Fe, Co, Ni etc) magnetic materials are widely used in devices like motors, generators, sensors, videotapes, and hard disks etc. At room temperature, magnetic nanoparticles with single domain exhibits superparamagnetism [Bean C P *et al;* 1959 and Bedanta S *et al;* 2009] which have applications in ferrofluids due to viscosity tenability [Colombo M *et al;* 2012]. Again superparamagnetic biomaterials like iron oxide based quantum dots are being used in clinical contrast agents in magnetic resonance imaging [Colombo M *et al;* 2012 and Indira T K *et al;* 2010].

1.2.4. Optical Properties

The most useful and interesting aspect of nanomaterials is its optical properties. A large number of studies on this area are appeared in the past. The optical properties of metallic as well as semiconductor nanomaterials are strongly size dependent. Optical properties originate due to the interaction of matter with radiation. Semiconductor nanomaterials and nanocomposites exhibit interesting linear absorption, photoluminescence emission, and nonlinear optical properties [Kumbakar P *et al;* 2014]. The quantum confinement effect of nanomaterials results in enhanced optical emission and nonlinear optical properties [Kumbakar P *et al;* 2014]. The optical properties of nanomaterials are basically related to the electronic structure and electrical properties. The quantum confinement effect helped to tune the optical properties of materials resulting in tunable emission [Lue J T; 2007]. The quantum confinement effects in nanomaterials are due to the increase in energy gap and surface plasmon resonance. The band gap increases with a decreasing size, results in higher frequency inter band transition or in other words a blue shift in the band gap energy which provide interesting luminescent properties. Intersetingly, luminescence emission and absorption edge can be tuned with the particle size and we could observe change in optical properties without change in chemical composition. The collective in-phase oscillation of coherent free electron excitation in the conduction band is known as the surface plasmon resonance (SPR). And this phenomenon occurs when the size of the material is less than the wavelength of incident radiation. Change in optical properties of materials as a result of size reduction finds application in lasers, sensors, displays, solar cells, photocatalysis, and in all interdisciplinary subjects. The optical properties of nanomaterials finds

technological applications for sensing and detection, optical imaging, light energy conversion, photovoltaics, solar cells, environmental protection, biomedicine, food safety, security and optoelectronics [Zhang J Z; 2009]. The optical properties of nanomaterials, based on surface enhanced Raman scattering (SERS) [Yonzon C R *et al;* 2004, Zhang X *et al;* 2005, Zhang Y *et al;* 2005, and Sirbuly D J *et al;* 2007] or fluorescence [Kagan C R *et al;* 1996 (a & b), Willard D M *et al;* 2001 and Wang S P *et al;* 2002] are used in chemical and biochemical sensors and detection systems. One of the fast growing applications of optical properties of nanomaterials is the biomedical detection and treatment. Further these materials can be used for cancer treatment by photothermal ablation (PTA) and *in vitro* and *in vivo* imaging destruction of human carcinoma [Melancon M P *et al;* 2008 and Lu W *et al;* 2009]. The size dependent emission spectra of quantum wells, quantum wires and quantum dots make them attractive lasing media. Some of these nanostructures can act as laser cavities.

1.2.5. Physicochemical and Biological Properties

Properties like size, shape, chemical composition, physiochemical stability, crystal structure, surface area, surface energy and surface roughness etc are influenced by the reduction in size of materials. Nanomaterials with higher surface area with respect to its volume may contribute to increase in reaction rate and also selectivity and efficiency of chemical reactions [Sanderson P *et al;* 2014]. Nanomaterials also exhibit excellent catalytic properties while comparing to its bulk material. Research of nanomaterial based photocatalysts is progressing well with the synthesis of morphologically modified new material. Physical and chemical properties of nanomaterials are interrelated to each other [Gatoo M A *et al;* 2014]. Some of the nanomaterials binds with protein molecules and has several applications for nano-based

development of drugs. Some of the nanomaterials are capable of attaching drug molecule and are helpful for targeting of drugs at site of action.

High luminescent non-toxic nanomaterials with better chemical and physical properties are exhibiting wide applications in biological and medical fields. But unfortunately some of the materials are toxic to human cells and investigations on nanotoxicity are also going on recently. The nature and functions of bio-molecules can be explored with the help of nanotechnology. Bio-nanotechnology has been using their possible applications in the fields of drug delivery [Sun T M *et al;* 2014, Lu Y *et al;* 2013, Pierobon P *et al;* 2012 a & b, Cash K J *et al;* 2010 a & b, Smith A M *et al;* 2008, Biju V *et al;* 2008 and Gao X *et al;* 2004]. Nanomaterials are used to conjugate with bio-materials since the bio-nanomaterials are having size proportionality with bio molecules and they are used in living cell applications [Haglund E *et al;* 2009, Cheng Y *et al*; 2008, Biju V *et al;* 2008, Michalet X *et al;* 2005 and Dubertret B *et al;* 2002]. Recently quantum dots are finding much more applications in the biomedical fields because of its high luminescence and size dependent properties.

1.3. Semiconductor Nanoparticles

Semiconductors are those materials whose electrical conductivity falls in between a conductor and an insulator. In semiconductors, the valence band is completely filled with electrons whereas the conduction band is almost empty. The conductivity of semiconductors varies from 10^{-8} S/cm to 10^{3} S/cm. In conductors, the charge carriers are electrons, whereas in semiconductors charge carriers are either electrons or positively charged holes. Germanium (Ge) and Silicon (Si) are very popular and commonly used semiconductors. The resistivity of semiconductors can be altered up to

10 orders of magnitude with the help of suitable doping. Research on semiconductor nanoparticles become an important research topic because of its wide range of applications in the fields of biology, chemical industry and optoelectronics.

Solid state materials are categorized in to conductors, semiconductors and insulators on the basis of conductivity. At room temperature the resistivity of metals are around 10^{-6} Ω cm, that of semiconductors lies between 10^{-3} to 10^{9} Ω cm and for insulators its value is 10^{12} to 10^{22} Ω cm. The resistivity of semiconductors is temperature dependent. Semiconductors usually termed as materials with band gap value 1 to 4 eV. On reducing semiconductors to nanoscale, its physical, chemical, optical, electronic and mechanical properties will drastically change. Devices based on semiconductor nanomaterials are having wide applications in solar cells [Tsakalakos L *et al;* 2007], light emitting devices [Garnett E C *et al;* 2007], lasers [Zimmler M A *et al;* 2008], waveguides [Javey A *et al;* 2007], biological applications and sensors [Fan Z Y *et al;* 2005, Mah C *et al;* 2000, Pereiro M *et al;* 2008], catalysis [Haruta M *et al;* 1993], energy storage [Wang J *et al;* 2007] etc. The widely investigated semiconductor nanomaterials are Si, Ge, GaAs, GaN, InP, InGaAs, ZnS, ZnSe, SiC, CdSe, CdS and CdTe etc. Semiconductor nanomaterials are also having potentials applications in luminescence, catalysis, and nonlinear optics etc. Wide band gap semiconductors like SiC and GaN have widely used in power electronics because of their superior properties [Shenai K *et al*; 2013].

1.4. Types of Semiconductor Nanoparticles

The size reduction of the materials can be done by different ways. When one of the dimensions is reduced to the order of electron wavelength, its material properties will be entirely different. These materials are called

low dimensional structures, and the reduction of the size actually contributes to confinement of electrons of holes. On the basis of direction on which dimension is reduced, materials are classified as two dimensional (2D), one dimensional (1D) and zero dimensional (0D) structures [Pradeep T; 2007].

1.4.1. Two Dimensional (2D) Nanostructures: Quantum Well

2D nanostructures are very important type of material which exhibit quantum confinement effect in its physical properties. When one of the dimensions of the material is reduced to the order of wavelength of electron, such structures are called 2D. In this type of materials, electrons can move in two directions and is confined in one direction. The electronic energy levels will be modified and it may have relatively higher band gap corresponds to its bulk counterparts. 2D materials are also called quantum well structures and some of the thin film structures come under this category. The possible energy levels that the electrons can occupy (density of states-DOS) are quantized and exhibit step like behavior. The quantum well structures are synthesized by sandwiching a narrow band gap material between two insulator materials. Instead of that a wide band gap materials like AlGaAs/GaAs/AlGaAs etc can be used [Pradeep T; 2007].

1.4.2. One Dimensional (1D) Nanostructures: Quantum Wire

In quantum wire structures, two dimensions of the bulk are reduced to the electron wavelength regime. In these materials the electrons are allowed to move in only one direction and are confined in two directions. Electronic energy level bands are widened and these materials show higher order of band gap. Quantum wire nanostructures have its crystal growth in one direction; it may be along any one of the axes. Its density of states shows a Lorentzian line shape. Nanorods, nanowires, nanotubes (carbon)

etc, are important 1D nanomaterials. Electronic transport of quantum wires gets less scattered and shows high mobility results in its application in lasers. Quantum wire structures are used for optoelectronic devices, diode lasers etc [Kapon E *et al*; 1992 and Pradeep T; 2007].

1.4.3. Zero Dimensional (0D) Nanostructures: Quantum Dot

In quantum dots, all three dimensions are quantized such that electrons cannot move anywhere and localized to a point. Electronic energy levels of quantum dots are discrete. The materials having dimensions in the range of several hundred to thousands of atoms are quantum dots. In terms of material size it may have size less than 10 nm to around 0.5 nm. Quantum dot structures exhibit strong confinement effect when its size is comparable to the Bohr radius of corresponding material. The spatial confinement of electrons or holes in these materials gives better emission properties. The emission wavelengths of quantum dots can be changed by simply changing the size, because of that these materials attained much more attention in the field of research. These materials can be used for efficient lighting systems, photovoltaic devices and for bio-imaging applications [Pradeep T; 2007].

1.4.4. Confinement Regime

Size of the material is an important consideration in the case of low dimension structures because drastic change in band gap may arise as a result of size reduction. When the particle size approaches to or below the bulk Bohr excitonic radius the effect of quantum confinement occurs and material properties are determined by its size. Bohr radius is [Yoffe A D; 1993, Efros A L *et al;* 2000, Efros A L *et al;* 1982]

$$a_B = \varepsilon\left(\frac{m}{m^*}\right)a_0 \text{ Or } a_B = \frac{\hbar\varepsilon}{\mu e^2}$$

where,

- ε - dielectric constant
- m - electron rest mas
- m^* - particle mass
- a_0 - Bohr radius of hydrogen atom
- μ - exciton reduced mass
- $\hbar$ - Planck's constant

The particle radius 'r' and the bulk exciton radius 'a' are factors which size regime depends.

$r << a_0$ (strong confinement)

In this condition, Coulombic force between electrons and holes are weak compared to the confinement energies. And the electrons and holes can be considered as separate particles [Efros A L *et al;* 2000, Efros A L *et al;* 1982].

$r >> a_0$ (weak confinement)

In this condition, electron-hole interactions is due to the confinement energy and their mobility is correlated which is usually termed as weak confinement regime [Efros A L *et al;* 2000, Efros A L *et al;* 1982].

$r \sim a_0$ (intermediate regime)

In this case, both Coulombic force of interaction between electrons and holes and confinement energies affect the electronic structure of the material [Efros A L *et al;* 2000].

1.5. Nanophosphors

Phosphors are those materials which emit light or produce luminescence when excited with suitable radiations. Nanophosphors have

been studied extensively for the last a few years because of their potential applications in displays and devices with high performance. Nanophosphors are also termed as doped nanocrystals (DNCs). There are several method used for the synthesis of nanophosphors. In order to use the advantage of quantum confinement effect, these synthesis methods should restrict the particle size which is less than twice of Bohr radii of exciton. Nanophosphors were synthesized by a variety of physical (molecular beam epitaxy, sputtering, consolidation etc) and chemical methods (colloidal, sol-gel, etc).

The optical properties of nanophosphors depend on surface morphology because nearly half of their atoms lie on the top of two monolayers [Chander H; 2005]. The enhancement in the optical properties of semiconductor nanophosphors like ZnS, PbS, ZnSe and CdSe were observed [Chander H; 2005]. Wide band gap semiconductors which are intentionally doped with impurities for getting emission in the desired range are also extensively studied. Nanophosphors of different semiconductor materials have been synthesized in powder as well as in thin film forms. These nanophosphors or nanoclustures are mostly sulfides, oxides and selenides of Zn, Cd, Pb [Chander H; 2005] etc. Generally phosphors will have a host material and one or more activators or doped impurities with wide band gap (> 3 eV). The emission from the nanophosphors is usually from host semiconductors as well as from the localized centers. In this the semiconductor luminescence will have band-to-band excitation and the emission from impurity states. But in luminescent centers, the transition occurs between energy levels of single ions. Several phosphors have been synthesized and the applications of phosphors mainly include in displays, imaging purposes and CRT displays etc.

1.6. Luminescence

Luminescence is simply the emission of light from a material which is not resulting from heat energy. Luminescence is a cold body radiation attributed to chemical reactions, electrical energy, subatomic motions and external source of energy etc. Vij interpreted that luminescence is a science related to spectroscopy and the study of general laws of absorption and emission of radiation by matter [Vij D R; 1998]. When a molecular or an atomic system is allowed to interact with external source of energy, the electronic states of the solids are excited and a transition from lower energy level to higher energy level occurs. Later these emitted electronic states undergo decaying to lower energy system with the emission of optical radiation. Luminescence includes a variety of emission processes and is classified based on the sources of energy that causes the excitation form lower energy level to the higher energy level. Luminescence from the material can be activated with different excitation sources and are classified based on it. Cathodoluminescence is activated by the electrons (cathode rays). Nuclear radiations are can also generate luminescence which is termed as radioluminescence. Electric field activated luminescence is called electroluminescence. Sound waves can also generate luminescence from the material which is called sonoluminescence. Chemical energy activated luminescence is called chemiluminescence and biochemical energy activated luminescence is termed as bioluminescence. Finally luminescence generated by material when it is excited with photons or light is called photoluminescence [Vij D R; 1998].

1.6.1. Photoluminescence

Among these types of luminescence in solids, when the system undergoes excitation from lower energy level to higher energy level by absorbing a photon and then decay to lower level with the emission of radiation usually in the visible region is termed as photoluminescence (PL). In photoluminescence process the required energy for excitation is extracted from infrared, ultraviolet, or visible light. The emission of photons from the excited state may be by different process like vibrational relaxation, internal conversion, intersystem crossing and non-radiative de-excitation [Peter TC So *et al;* 2011]. The vibrational relaxation process is mainly the relaxation of excited molecules to the lowest level of excited electronic state. Internal conversion is another relaxation process between the electronic states of like spin multiplicity such as S_1 and S_2. The intersystem crossing occurs with non-radiative relaxation between the excited states of different spin multiplicity. In non-radiative de-excitation process, the relaxation excitation energy leads to the decay of excited molecule to the ground electronic state. The emitted photon cannot have more energy than the excited photons because of these processes. Based on the nature of ground and excited states, photoluminescence is divided as fluorescence and phosphorescence.

1.6.1.1. Fluorescence

Photoluminescence process occurs between energy states with same spin multiplicity or simply emission from singlet electronic state. The decay time is about 10^{-5} to 10^{-8} seconds. Fluorescence arises by the radiative transition from excited state to the ground state of activator. The decay time of fluorescence is independent of temperature. As long as excitation lasts fluorescence occurs, and as excitation stops the fluorescence also stops.

1.6.1.2. Phosphorescence

It is a photoluminescence process which occurs between the energy states having different spin multiplicity (triplet-singlet transition). In this case emission is slightly delayed after initial absorption of radiation and the decay time is greater than 10^{-5} seconds. Phosphorescence is the delayed transition of electrons from traps through the conduction band and it occurs after the removal of excitation source. The decay time depends on the temperature of the emitting source.

1.6.2. Types of Photoluminescence

Photoluminescence is mainly classified as,

1.6.2.1. Intrinsic Luminescence

Intrinsic luminescence occurs in very pure crystals. This is contributed to either band to band transition or excitonic luminescence and the detailed mechanism are given below.

1.6.2.1a). Band-to-band luminescence

Luminescence arises due to the recombination of an ***electron*** in conduction band with a ***hole*** in the valence band, it occurs usually at high temperature. Pure semiconductor crystals like Si,Ge, GaAs, GaN etc exhibit this type of luminescence [Shenai K *et al*; 2013].

1.6.2.1.b). Exciton luminescence

Excitons (electron-hole pair) are the key factor for this kind of luminescence. The recombination of electron and hole will produce this type of luminescence. An exciton is a two particle system which excited electron and hole bound interacting together. There are two types of excitons exists. Electron and hole bound by Coulomb force is called Wannier. In some cases wave

function associated with electron and hole may be smaller than lattice constant of the material, and these types of excitons are called Frenkel [Vij D R; 1998].

1.6.2.1c). Cross luminescence

Luminescence produced by the recombination of an electron in the valence band with a hole created in the outermost core band and is observed in BaF_2 for the first time. Cross luminescence is also observed in alkali halides of alkaline-earth and double metals which satisfies the condition of $\mathbf{E_{c\text{-}v}} < \boldsymbol{E_g}$. The decay time of cross luminescence is very fast [Vij D R; 1998, Peter TC So *et al;* 2011].

1.6.2.2. Extrinsic Luminescence

Luminescence caused by the incorporation of impurities which are doped intentionally or by the presence of crystalline defects like lattice vacancies, dislocations, interstitial and substituted impurities etc. Luminescence properties of activators come under this category [Hu H *et al;* 2006].

1.6.2.2a). Unlocalised Type

The free electron in the conduction band and the free holes in the valence band participate in the luminescence process and the luminescence occurs due to the donors and acceptors. These donors and acceptors acts as luminescence activators. There are two types of transition may occur; one is the transition of a free carrier to a bound carrier. And another one is transition of a bound electron at a donor to a bound hole at an acceptor (donor-acceptor pair transition). This type of luminescence is usually observed in IIIb-Vb and IIb- VIb compounds like CeAs, PrN etc.

1.6.2.2b). Localised Type

In this the excitation and emission processes are confined in a luminescence centre and are produced in ionic crystals and semi conductors by the intentionally incorporated metallic impurities. Some kinds of lattice defects also act as localized luminescence centers [Park S *et al*; 2012].

1.7. II-VI Semiconductors

II-VI semiconductors are wide band gap materials which are considered for optoelectronic devices operating under the excitation of UV sources. CdSe, CdS, CdTe, ZnSe, ZnS, ZnTe, ZnO (i.e, compound of IIb metal with VIa cations) etc are the widely used II-VI compounds [Suresh S; 2013]. Most of the II-VI compounds are crystallizes in zinc blende or wurtzite crystalline structures. Zinc blende crystallites will be obtained at room temperature and wurtzite is usually at the high temperature. Elements belonging to VI group are more electronegative than group II. II-VI elements usually give covalent or ionic bond type compounds. The band gaps of covalently bonded compounds are comparatively less with respect the ionic type. These materials either possess n-type or p-type and sometimes both n and p-type conductivities. CdS, CdSe, ZnS and ZnO are some of n-type semiconductors [Shadia J *et al*; 2014]. Most of the II-VI semiconductors are direct band gap with broad range of band gap values having good optical absorption and emission properties. Moreover they possess lasing properties (in ZnS and ZnO materials) mainly in UV region. Among these ZnS is one of the important II-VI semiconductors, which is the first material among the phosphor compounds used in cathode ray tube displays [Shadia J *et al*; 2014, Suresh S; 2013].

1.8. Zinc Sulfide (ZnS)

ZnS possess high transmission in the visible region and with high refractive index of the order of 2.2. ZnS is covalently bonded material with high exciton binding energy of about 40 meV at room temperature. Cubic crystalline form of ZnS is known as zinc blende or sphalerite, which is the low temperature phase and having band gap of 3.68 eV [Uzar N *et al;* 2011] [Figure 1.1]. The hexagonal form of ZnS is called wurtzite. It is the high temperature phase which has a band gap of 3.77 eV. The zinc blende phase of ZnS has *fcc* arrangement in which S^{2-} ions are at the corners and face centered Zn^{2+} ions are present in alternate tetrahedral voids. But the wurtzite phase has *hcp* structure in which stacking pattern is different. The lattice parameters of sphalerite type ZnS is 'a' = 'b' = 'c' = 5.406 Å, and the space group is F4-3 m. But the unit cell values of wurtzite phase ZnS is 'a' = 'b' = 3.82 Å, 'c' = 6.26 Å, and the space group is P63mc. The ionic radius of zinc is 0.074 nm and sulphur is 0.184 nm. The phase transition temperature from cubic to wurtzite phase is at 1020 °C [Yim WM *et al*; 1972].

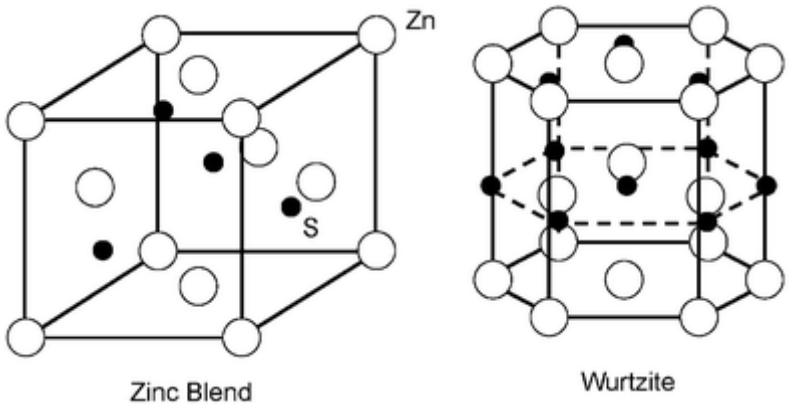

Figure 1.1: Crystal structure of ZnS [Moore D et al; 2006].

ZnS is a good host lattice phosphor for photonic applications and electroluminescent devices because of its wide band gap. ZnS based

phosphors like ZnCdS:Ag, Cl (red) [Huh Y D *et al;* 2004], ZnS:Cu, Al (green) [Kao C C *et al;* 2009], and ZnS:Ag (blue) [Kajiwara K *et al;* 2003], etc with different colours also used for making warm white light sources and white LEDs. ZnS nanostructures with morphologies like needles, rods, sheets, micro-and nanospheres, belts etc can be grown with chemical method by using surfactants or templates [Sookhakian M *et al;* 2013]. Recently semiconductor microspheres obtained much more attention because of its potential applications in the fields of drug targeting, bio-separation, diagnostic analysis and light emitting devices [Yu X *et al;* 2009]. Nanomaterials with UV-blue emission like CdS, ZnCdS, ZnSe, ZnS and their doped materials were widely used for biological applications [Durgadas C V *et al;* 2012, Hsieh J M *et al;* 2006, Wang G *et al;* 2011 and Liab J *et al;* 2013]. ZnS is also best suited for biological systems and applications, since it is less toxic as compared to lead and cadmium based compounds [Chatterjee A *et al;* 2007].

1.9. Review of Literature

ZnS belongs to II-VI compounds; it is an interesting material attained much more attention of academic research community. It is a promising candidate for several technological applications, especially for light emitting devices, hetero junction devices, biological applications etc [Hartmann H *et al*; 1982]. Its versatility over other materials is the key reason for the extensive study of ZnS. The morphology of the ZnS is tunable to spherical, ribbon, sheet, rod, tube, needle fibers and also in the form of thick and thin films [Ummartyotin S; 2016]. Further ZnS has variety of applications in the fields like medical, electronic and optoelectronic devices as well as in catalysis [Ummartyotin S; 2016]. ZnS composites are being employed and have potential applications in portable cell phone, movable sensor as well as

flexible solar cell to overcome brittleness [Ummartyotin S; 2016]. Several researchers have synthesized ZnS nanostructures with variety of morphology. Fang *et al* synthesized nanowires of ZnS by in-situ liquid crystal template formation, electrochemical deposition method, thermal evaporation and organic assisted chemical method etc [Fang X *et al*; 2006].

ZnS nanobelts and nanoribbons were synthesized by diethylenetriamine-assisted solvothermal method [Yao W T *et al*; 2005], hydrogen assisted thermal evaporation synthesis, physical evaporation, thermal evaporation method in an Ar atmosphere with the assistance of H_2S. Solvothermal method is also employed by using enthylenediamine followed by thermal treatment in N_2 flow system [Ma C *et al*; 2003, Jiang Y *et al*; 2003, Zhu Y C *et al*; 2003, Li Q *et al*; 2003, Liu X Y *et al*; 2004 and Kar S *et al*; 2005]. Wang *et al* reported the synthesis of wurtzite ZnS nanobelts [Wang Z W *et al*; 2005]. In 1998, Xu *et al* [Xu S J *et al;* 1998] reported ZnS:Cu, Eu, Mn nanocrystals synthesised with micro emulsion via hydrothermal method and found that 60 times PL enhancement compared to that of conventionally synthesised one.

The emission properties of sulphide based phosphors can be enhanced by doping with co-activators belongs to IIIa or VIIa group of periodic table. A donor level is produced by the co-activator which captures an electron and it combines with a hole in the deep acceptor level. The combining of electron and hole, gives the emission of a photon with energy less than the band gap (band gap energy minus depth of the acceptor and donor levels). The sulfides and selenides of Zn, Cd, Pb semiconductor nanoparticles synthesized by colloidal suspensions were studied since 1980s [Rosetti R *et al;* 1983, Rosetti R *et al;* 1984, Brus L E; 1986, Weller H *et al;* 1984, Fojtik A *et al;* 1984, Nozik A J *et al;* 1985, Rosetti R *et al;* 1986 and

Khosravi A A *et al;* 1995]. The electron beam bombardment study of ZnS phosphors both powder and film form were extensively investigated [Swart H C *et al;* 1998a, 1998b, 1996 and Sebastian J S; 1998].

The study on doped nanocrystals (DNCs) began from 1994 onwards, when Bhargava *et al* reported the Mn doped ZnS nanocrystals with 18% external photoluminescence quantum efficiency [Bhargava R N *et al;* 1994]. This result opened door to new class of doped nanocrystals with high luminescent yield with applications in the fields of displays, lighting, lasers, devices and sensors etc [Hu H *et al;* 2006]. Many groups have reported the synthesis and properties of nanomaterials with different dopants for luminescent applications. These dopants includes Mn^{2+}, Cu^{2+}, Ni^{2+}, Co^{2+}, Cd^{2+}, Pb^{2+}, Eu^{3+} , Tb^{3+}, Sm^{3+}, Er^{3+} etc. Among this Mn^{2+} doped ZnS were extensively studied because of its multiple valency states. ZnS and Mn-doped ZnS nanoclusters have been synthesized by hydrothermal approach [Hoa T T Q *et al;* 2011]. Recently co-doped (two elements together) ZnS were attained much more importance which includes Mn^{2+}- Ni^{2+}, Co^{2+}- Cu^{2+}, Cu^{2+}- RE (Er^{3+}, Ce^{3+}, Nd^{3+}, Tb^{3+}, Y^{3+}), Cu-Al, Mn-Eu, Cu^{2+}-In^{3+}, Pb^{2+}-Cu^{2+} and their combinations [Hu H *et al;* 2006]. Manganese and Cu doped ZnS nanoparticles were reported by Khosravi *et al*. [Khosravi A A *et al;* 1995 and Hu H *et al;* 2006] with different synthesis route like aqueous method and their polymeric chain formation. Yu *et al* [Yu I *et al;* 1996] reported the crystallite size variation in Mn doped ZnS prepared using methanolic solution of zinc acetate, sodium sulphide and manganese acetate. Surfactant assisted Mn doped ZnS synthesised by chemical precipitation method was reported by Yang *et al* [Yang H *et al;* 1997] and its optical properties were studied. They compared the properties of nanophosphors in powder and sol gel form which synthesised with and without surfactant. Manganese doped ZnS

nanocrystalline phosphor was synthesised by Senna *et al* [Senna M *et al;* 1997] from zinc acetate and Na_2S in methanolic solution containing carboxylic acid and its PL intensity increased on addition of acrylic acid during the synthesis process. The PL spectra of Mn-doped ZnS nanoclusters exhibited both the blue (defect related emission) and the orange Mn^{2+} ion-related emission. Peng *et al*, fabricated p-type ZnS NRs using Sb as the dopant via thermal evaporation. In 2001, Yang *et al* synthesised copper co-activated ZnS:Ce, Y, Nd, Er, Tb doped ZnS nanocrystals by solution precipitation method [Yang P *et al;* 2001]. The obtained ZnS quantum dots of size 2-3 nm and 5-6 times PL enhancement was observed. Synthesis of nanocrystals of Cu and halogen doped ZnS with PVP addition were reported [Manzoor K *et al;* 2003]. Later, Lee *et al* studied the effect of temperature on PL and particle size of ZnS:Cu nanocrystals [Lee S *et al;* 2003]. The role of capping agents like polyvinylpyrrolidone and pyridine in ZnS:Mn, ZnS:Cu, ZnS:Cu,Al, nanocrystals were reported by Manzoor *et al* in 2004 [Manzoor K *et al;* 2004] using wet chemical colloidal precipitation method and observed broadening in PLE spectra while grown with pyridine. Cathodoluminescence intensity variation with accelerating potential of ZnS:Cu phosphor were studied [Kingsley J D *et al;* 1972]. Nano SBDs (Schottky barrier diodes) based on the Al/p-ZnS NR Schottky junctions exhibited excellent rectifying behaviors. Co doping in ZnS nanoparticles also resulted in 35 times enhancement in the emission intensity [Peng Q *et al;* 2011]. M. Sharma *et al* synthesised luminescent chitosan capped ZnS:Mn via chemical precipitation route and it can be used for biosensing applications because it give different emission colours with different excitations [Sharma M *et al;* 2010]. PL spectrum of ZnS:Ni shows multiple peaks in the blue region under UV excitation. And it shows visible light emissions under the same UV excitation

wavelength of 310 nm from the above compound [Pathak C S *et al;* 2012]. ZnS NRs with tunable p-type conductivity is not realized on synthesising it with NH_3 and the capability of other V group elements as the p-type dopants is needed to be further exploited [Yuan G D *et al;* 2008]. ZnS:Cr(3 at.%) nanostructures were synthesized by chemical co-precipitation method using zinc acetate, sodium sulphide and chromium oxide as the source materials and EDTA as capping agent [Reddy D A *et al;* 2012]. The samples were annealed in air for 3 h in steps of 100 °C in the temperature range of 200–700 °C. The PL emission wavelength is tunable in the range of 440–675 nm as a function of annealing temperature [Reddy D A *et al;* 2012].

The substitution of rare earth ions in zinc host lattice is complicated [Hu H *et al;* 2006]. There is no confirmed interpretation on the incorporation of divalent transition metal ions or trivalent rare-earth ions in ZnS host lattice [Hu H *et al;* 2006]. Nanocrystals of ZnS doped with rare-earth ions (Eu^{3+}, Tb^{3+} and Er^{3+}) were synthesised by different methods shows that the rare-earth ions were not incorporated in the ZnS host lattice [Hu H *et al;* 2006]. This difficulty in incorporation of rare-earth ions is due to the differences in the chemical properties of Zn^{2+} and its ionic radii with respect to RE^{3+} ions [Bol A A *et al;* 2002]. But the divalent samarium doped ZnS shows optical memory properties [Kushida T *et al;* 2000 and Kurita A *et al;* 2000].

1.10. Biological Applications of Semiconductor Nanomaterials

The utilization of bionanomaterials in biological systems like cells, proteins, other cell components finds much more attraction recent years [Medintz IL *et al;* 2007, Gazit E *et al;* 2007, Soloviev V N *et al;* 2000, Ozin G A *et al;* 2009 and Wang S *et al;* 2007]. Major applications of bio-

nanomaterials include, bio-labelling [Bruchez M *et al;* 1998], *in vivo* and *in vitro* applications [Mah C *et al;* 2000], drug and gene delivery [Mah C *et al;* 2000], tissue engineering [Ma J *et al;* 2003], pathogenic bio detection [Edelstein R L *et al;* 2000], cancer therapy and cell detection[Yoshida J *et al;* 1999], live cell labelling and DNA probing [Mahtab R *et al;* 1995], MRI contrast [Weissleder R *et al;* 1990], and multicolour optical coding for biological assays [Han M *et al;* 2001]. Highly luminescent quantum dots are used as molecular imaging probes and cell tracking material. The cell tracking is possible by binding quantum dots with the proteins and receptors and hence to locate its position in the cell [Darbandi M *et al;* 2005, Nann T *et al;* 2004 and Mulvaney P *et al;* 2000]. The biological applications of quantum dots are achieved by making a hydrophilic surface coating. Another important application of quantum dots is in multiplex imaging in which these quantum dots are having different emissions with a single excitation [Smith A M *et al;* 2008]. QDs absorb continuous wavelengths in which a single excitation source can excite multiple QDs simultaneously. This property of QDs makes them to use as optical probes for different immunoassays, cancer cell imaging and cancer targeting etc [Liu L W *et al*; 2014]. QDs of $CuAlS_2$ nanocrystals and cadmium chalcogenides with PEG coatings finds applications in bio-imaging as well as cancer cell imaging [Aby C P *et al*; 2012 a&b]. Recently graphene attracted much more attention in bioimaging applications [Zhu S *et al*; 2011]. The major challenging problems of these semiconductor nanomaterials are the aqueous solubility and toxicity. Ligand exchange and coating with polymer materials are effective to some extent to overcome this problem.

1.11. Biological Applications of ZnS

The spectral tunability of semiconductor materials along with the high efficiency turned its importance in recent research which explored applications for cell tracking, cancer and cell detection [Fan G *et al;* 2014, Yong K T *et al;* 2010 and Lee J Y *et al;* 2014]. Medical bio-optical imaging has become an advanced research area recently, with the development of nanomaterials and inorganic nanocrystals possessing enhanced emission properties for bio-sensing and bio-imaging. Native biological fluorescence, light absorption and scattering by biological tissue constituents are strongly affecting the visible light imaging process [Luo S *et al;* 2011]. Hemoglobin and amino acids strongly absorbs wavelength below 600 nm [Maestro L M *et al;* 2012, Wang G *et al;* 2011 and Zagorovsky K *et al;* 2013]. Usually cadmium based quantum dots are being used for bioimaging because of its inherent high quantum yield. However, the bio-accumulation of hazardous materials like Cd is harmful to vertebrate system and organs [Pradhan N *et al;* 2007, Poulose A C *et al;* 2012 and Luo P G *et al;* 2013] and its bio-stability [Yong K T *et al;* 2010, Lee J Y *et al;* 2014, Luo S *et al;* 2011, Ruan S *et al;* 2014 and Polavarapu L *et al;* 2011]. Unfortunately, bio-compatible, heavy metal free and high fluorescent non toxic materials which are suitable for bioimaging are less in number. Semiconductor nanomaterials surrounded by organic monolayers having enhanced optical properties with high stability are another option to escape from toxicity of Cd based chalcogenides for bio-imaging. Hsieh *et al* used highly luminescent CdSe/ZnS quantum dots (QDs) as visible imaging dye [Hsieh J M *et al;* 2006]. In-vivo imaging studies and tumor targeting of QD bioconjugates were reported [Yong K T *et al;* 2010]. Ruan *et al* reported carbon based nitrogen-doped nanospheres as advanced materials in this area

[Ruan S *et al;* 2014]. Nanomaterials with UV-blue emission like CdS, ZnCdS, ZnSe, ZnS and their doped materials were widely used for biological applications [Durgadas C V *et al;* 2012, Hsieh J M *et al;* 2006, Wang G *et al;* 2011, and Liab J *et al;* 2013]. The major drawbacks of above luminescent materials are that they required biocompatible surface coating [Durgadas C V *et al;* 2012]. Comparatively less toxic ZnS having high luminescent yield with good biocompatibility are suitable candidate for replacing the traditional toxic cadmium based materials. But there are a few reports based on ZnS; because of ultraviolet-to-blue emissions from the ZnS get escaped in body tissue [Zagorovsky K *et al;* 2013].

In 2005 Yang *et al* reported the biological labelling application of CdS:Mn/ZnS quantum dots. They observed that the reported material is a promising candidate for the *in vivo* bioimaging application [Yang H *et al;* 2005]. Later, in 2008 He *et al* demonstrated that doped QDs are promising for RTP detecting applications. In this particular work they reported room-temperature phosphorescence (RTP) method based on the phosphorescence property of the Mn-doped ZnS QDs for the selective detection of enoxacin in biological fluids [He Y *et al;* 2008]. Geszke-Moritz *et al*, in 2013, reported thioglycerol capped very low cytotoxic Mn doped ZnS quantum dot bioconjugates for bioimaging applications. TG-capped Mn:ZnS nanocrystals can be readily conjugated with folic acid for specific targeted bioimaging applications [Geszke-Moritz M *et al*; 2013]. Bio medical applications of less cytotoxic, biocompatible uncapped and capped ZnS:Mn nanocrystals with chitosan, L-citrulline, L-lysine, L-arginine, L-serine, L-histidine and glycine as capping agents were reported [Sajimol A M *et al;* 2015]. Nanocrystals capped with L-citrulline are less toxic for 0.1 nM concentration and hence highly bio-compatible [Sajimol A M *et al;* 2015].

Positron emission tomography (PET) and optical imaging applications of CuInS/ZnS quantum dots were reported recently [Guo W *et al;* 2015]. Currently several nanomaterials and semiconductor quantum dots are widely used for bio-medical applications by exploring their magnetic and luminescence properties [Mansur H S *et al;* 2015]. Important drawbacks of these quantum dots are regarding its toxicity. Commonly used quantum dots includes toxic elements like Cd^{2+}, Pb^{2+} and organic ligands (like triocytlphosphine - TOP and triocytlphosphine oxide - TOPO) stabilised materials are very toxic and harmful. Synthesis of biocompatible ZnS quantum dot (QD) nano-immunoconjugates by an eco-friendly method for cancer cell detection was investigated [Mansur H S *et al;* 2015]. In this contest zinc chalcogenides and zinc based doped materials (Zn doped with Mn^{2+}, Fe^{3+}, Cu^{+}, Ni^{2+}) are good alternatives since they are less toxic and cadmium free [Mansur H S *et al;* 2015].

1.12. Motivation of the Thesis and Statement of Research Problem

Highly luminescent bio-compatible non toxic semiconductor phosphors are very important material for various applications. Studies on morphology controlled synthesis and optical properties of ZnS phosphors attained much more attention, especially for the application in the biomedical filed. Highly luminescent ZnS have many applications in optoelectronic devices, displays and for imaging of biological tissues. The growth of ZnS with different morphologies can be achieved by several synthesis routes. The motivation behind the present research on ZnS materials is to synthesis highly luminescent ZnS materials by modifying synthesis method. Apart from that the synthesis method should be very

simple, cost effective and eco-friendly. Among several semiconductor phosphors, Cadmium (Cd) based phosphors are being used for the biomedical applications because of its wide and better luminescence properties. But Cd based materials are highly toxic and are coated with polymer or core-shell structures to overcome toxicity. In this context, the less toxic and biocompatible semiconductors like ZnS plays a major role. Tuning the emission properties of ZnS is much easy compared to other semiconductors. Semiconductors with emission above 600 nm are generally used for the bio-imaging applications. Our preliminary aim is to synthesis ZnS materials with emissions in UV, visible and in Near-IR regions. The work is focused on the morphology controlled synthesis of ZnS and tuning the optical properties.

Objectives of the thesis

The brief and specific objectives of the present investigations are given below

- To optimize the reaction condition for the synthesis of highly crystalline ZnS, and to formulate new synthesis route by modifying the reaction procedure in hydrothermal method.
- Synthesis of relatively oxygen free porous ZnS by solvo-hydrothermal method.
- To investigate the structural, luminescence and morphological properties of these porous ZnS.
- To synthesis Mn doped ZnS nanostructures with high luminescence using solvo-hydrothermal method.

- To modify the morphology of ZnS samples and to find the effect of surfactants like Ethylenediamine, Polymethyl methacrylate, Cetyl trimethylammonium bromide, and Polyethylene glycol on morphology of solvo-hydrothermally grown ZnS.
- To synthesis and investigate the photoluminescence nature of Near-IR emitting ZnS: Neodymium host:guest system.
- Studies on the biocompatibility and imaging efficiency of above mentioned materials.
- Correlation of the results.

2 Synthesis Methods and Characterization Tools

Chapter

2.1. Introduction

Synthesis of nanomaterials has attained much more attention due to their size, shape and morphology dependent superior properties. Nanoscale materials have high surface to volume ratio and posses special properties like good adsorption, physical, chemical and optical properties. It is a fact that the properties of the materials are strongly depends on the stoichiometry, morphology and the nature of impurities present during the growth process. Knowledge about the growth mechanism is very important in order to control the size and morphology of these materials. There are several methods used for the synthesis of nanomaterials. This chapter discusses the different methods that were used for the synthesis of nanomaterials. Among these synthesis methods, special attention is given to hydrothermal and solvo-hydrothermal synthesis method as the thesis is focused on these two methods. This chapter also discusses the various characterization techniques employed for the analysis of the samples. These analysis techniques includes X-Ray Diffraction (XRD), Scanning Electron Microscopy (SEM), Energy Dispersive X-ray (EDAX) analysis, UV-Vis-NIR spectroscopy, Diffuse Reflectance Spectroscopy (DRS), Photoluminescence (PL), Transmission Electron Microscope (TEM), Selected Area Electron Diffraction pattern (SAED),

Fourier Transform Infrared (FTIR) spectroscopy, Fourier Transform Raman (FT-Raman) spectroscopy.

2.2. Methods of Synthesis of Nanomaterials

Researchers mainly used two approaches for the synthesis of nanomaterials, viz.: top-down and bottom-up.

2.2.1. Top-down Method

It is one of the initial methods used by the experimentalists for the production of nanomaterials from its bulk counterparts. This method is relatively expensive related to other methods. In this method, a bulk material is reduced to nanosize either by successive cutting or by milling. Light based method like photolithography is one of the important top-down methods. Further, ball milling, etching, sputtering etc are widely used by researchers based on top-down approach.

2.2.2. Bottom-up Method

Bottom-up approach is widely and commonly used method for the synthesis of nanomaterials. In this method, materials are made from its precursors either by atom by atom or molecule by molecule or cluster by cluster. Self assembly of nanoparticles will occur naturally in this process. This method is particularly used to synthesis materials with relatively less defects. Apart from that, homogeneous chemical composition of as grown products can be maintained. Bottom-up approaches mainly come under two broad categories which are 1) physical methods and 2) chemical methods.

(1) Physical Methods

Physical methods need sophisticated instrumentation and in most cases high vacuum condition is required. These techniques include

sputtering, Pulsed Laser Deposition (PLD), Physical Vapour Deposition (PVD), Chemical Vapour Deposition (CVD), Molecular Beam Epitaxy (MBE) and Metal Organic Chemical Vapour Deposition (MOCVD). Spray pyrolysis is a relatively cost effective technique for the production of nanomaterials without vacuum conditions.

(2) Chemical Methods

Chemical methods include Chemical Bath Deposition (CBD), simple chemical precipitation method, sol-gel method, **hydrothermal method, solvothermal method** and electrodeposition.

2.3. Hydrothermal Method

Hydrothermal method is one of the important methods used for the synthesis of nanomaterials as well as bulk crystals. The term hydrothermal was firstly used by Sir Roderick Murchison (1792–1871), a British Geologist to describe the role of water at high temperature and pressure for explaining the formation of various rocks and minerals [Byrappa K *et al;* 2007]. Hydrothermal method simply gives a nanocrystal in the presence of aqueous media facilitated by temperature and autogenous pressure. This method uses water (critical temperature is 374 °C and pressure is 22.1 MPa) or some aqueous solutions which can dilute materials at high temperature and pressure which are insoluble under normal conditions [Hayashi H *et al;* 2010]. Hydrothermal synthesis is usually carried out at a temperature below 300 °C. Metallic oxides, metallic sulfides, silicates etc, can be synthesized by hydrothermal method. Temperature of the reaction process, pH, molarities of the precursor solutions, duration of the reaction and the pressure formed during the reaction process are the important parameters which determines the quality of as grown crystals. In hydrothermal process,

the rate of reaction is enhanced to 1000 times than at normal condition [Hayashi H *et al;* 2010]. The crystallinity of the materials is improved with the hydrothermal method as the dielectric constant of water decreases. It is relatively low cost technique with respect to other chemical based techniques. This technique gives maximum yield from the initial reactants. The hydrothermal process includes hydrothermal decomposition, hydrothermal synthesis, hydrothermal stabilization of structures, hydrothermal sintering and hydrothermal treatment etc.

This method is modified by the researchers and several solvents are being chosen as the growth medium. This technique is nowadays properly known as solvothermal method. This means chemical reaction in the presence of solvents at supercritical condition [Byrappa K; 2007]. Organic solvents such as ethanol, propanol, methanol etc are used as the solvents for the synthesis process. Solubility of salts in these solvents is also critical for determining the quality of the product.

2.3.1. Merits of Hydrothermal/Solvothermal Synthesis

In hydrothermal/solvothermal synthesis solvents are set to be at supercritical condition. The supercritical water (SCW), which is maintained above its critical temperatures and pressures are termed as supercritical fluids (SCF). Properties of SCF mainly depend on temperature and pressure of the system and fluid acts as an intermediate between gas and liquid phase. The density of gas and liquid phases are same at critical point which may have properties of both gas and liquid. The particular atmosphere favours the reaction rate of the reactants and supports the formation of particles with small size. The SCFs are having relatively high diffusivity and low viscosity. This is due to the high solubility of particles and its

mobility with respect to other conditions. The controlled stoichiometry can be achieved in hydrothermal synthesis process with high purity. Apart from that it has several advantages over other methods. It gives particles with narrow size distribution, uniformity, controlled morphology, high crystallinity and less defects etc. More over this technique have advantages like high yield since there is a provision to use equipments with large volume. Further this method is eco-friendly, cost effective, better shape control, low temperature process and having high reaction rate.

2.3.2. Hydrothermal Apparatus

Instrumentation part of hydrothermal apparatus is very important with respect to safety, since the crystal growth is carried out under high temperature and pressure. The main parts of a hydrothermal reactor are hydrothermal oven/furnace, autoclave/pressure vessel, and a teflon lined beaker [Figure 2.1].

2.3.2a. Hydrothermal oven or furnace

The heating of hydrothermal process usually done by the aid of heating coil wounded over the hydrothermal autoclave. So this is relatively expensive and temperature control is also somewhat difficult. So the heating of hydrothermal growth process used in the present study is achieved by means of a heating oven. An oven or furnace is needed for providing required temperature for the reaction. The furnace is attached with programmable Proportional Integral Derivative (PID) control system so as to set reaction at desired time and temperature. The furnace is guarded with other safety conditions.

2.3.2b. Autoclave

The most important part needed for a reaction is the reaction vessel. The reaction vessel for hydrothermal synthesis is called autoclave. In hydrothermal reactions, we often use highly corrosive salts and chemicals. So an autoclave should able to maintain highly corrosive solvents at elevated temperatures and pressures for a long time [Byrappa K *et al;* 2011]. An ideal hydrothermal autoclave should have inertness to acids, bases, oxidizing agents and corrosion resistant. Its parts mainly nuts and bolts or screws should be able to assemble and dissemble easily. Further it needs adequate volume in order to obtain a desired temperature gradient. More importantly it should be leak-proof even at high temperature and pressure range. The material used for the fabrication of autoclave should have capacity to withstand high temperature and pressure for a long time without any kind of damage. Highly corrosion resistant materials like stainless steel, nickel, iron, super alloys, and titanium alloys etc are preferred for making autoclave.

2.3.2c. Teflon Lined Beakers

In hydrothermal method, the chemical reagents used for the reaction may react with the vessel, so a coating with non reactive material having larger thermal expansion coefficient is needed in order to avoid corrosion of autoclave. Quartz beaker, teflon beaker etc are being used for taking reactants in hydrothermal/solvothermal methods instead of making inner line inside the autoclave. Teflon is inert to the reaction materials which expand on heating and contract up on cooling. So Teflon beaker is a suitable material which can be used as liner in hydrothermal reaction system. The major drawback of Teflon is that it dissociates above 300 °C, so hydrothermal reaction above 300 °C is not possible.

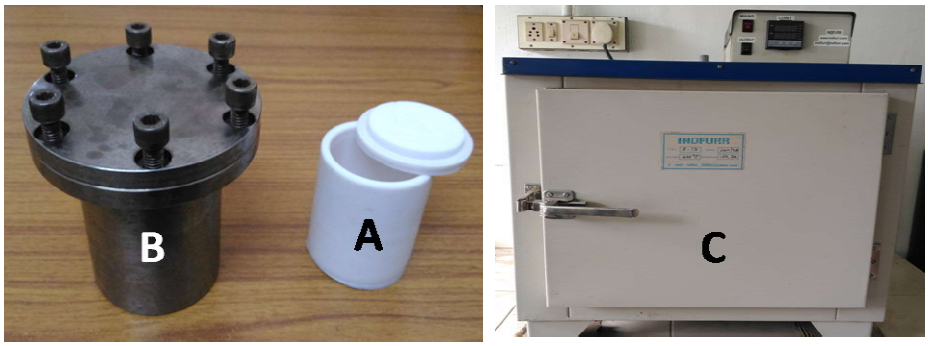

***Figure 2.1**. (A) Teflon beaker,(B) autoclave and (C) hydrothermal furnace used for the synthesis of materials under study.*

2.4. Solvo-hydrothermal (S-H) Method

The synthesis of ZnS nano and microstructures were done both by hydrothermal as well as solvo-hydrothermal method. In the solvo-hydrothermal method, we used a reaction medium containing solvent and water in 1:1 ratio. That's why we used the term 'solvo-hydrothermal'.

In S-H method, different combinations of organic solvents with water can be taken as growth medium. Acetonitrile is an important oxygen free polar organic solvent. In order to reduce the water and oxygen content to a certain extend in the reaction system we chose oxygen free solvent acetonitrile. The reaction is termed as solvo-hydrothermal (S-H) reaction.

2.5. Characterization Tools

Structural characterization

2.5.1. X-ray Diffraction

X-ray diffraction is one of the characteristic tools used for the identification and structure determination of crystalline materials. The wavelength of X-rays is comparable with that of the interatomic distance in

crystal system. X-rays are the electromagnetic radiations having wavelength of the order of inter atomic distance in crystals (0.15-0.4 nm) and these X-ray posses' photon energies of the order of 3-8 keV. The incident X-rays may be scattered by the atom, reflected by the planes and these reflected or scattered radiations produce constructive as well as destructive interference patterns, consequently diffraction.

The basic law governing the X-ray diffraction technique of structural analysis is the Bragg's law. Bragg's law given by

$$n\lambda = 2d\sin\theta$$ [Kittel C; 1996]

where,

n - order of diffraction

λ - wavelength of the X-ray

d - spacing between consecutive planes

θ - angle of incidence

The constituents (atoms, ions, or molecules) of a crystalline solid are arranged in a regular periodic ordered crystal planes. The crystal planes act as diffraction gratings and the interaction of this crystalline solid with X-rays reveals the nature of crystal structure. With the X-ray diffraction analysis, we can determine the structure, i.e. how the atoms pack together in the crystalline state and what the interatomic distance, size and the shape of the unit cell etc. The diffraction pattern of a crystal is unique to that of a particular material. It can give finger print information about the material. As a consequence of the interaction of matter with the X-rays, sample will give characteristic X-ray diffraction peaks corresponding to the material present in the sample, but not in terms of its constituent elements.

Diffraction analysis discloses information regarding the elemental chemical combination state and its phase of growth. X-ray diffraction studies are fast, non-destructive and very small quantity of the sample is needed [Cullity B D *et al;* 2001 and Buerger M J *et al;* 1962]. An X-ray diffractometer consists of X-ray source, sample holder and an X-ray detector. X-ray production is one of the important investigations in the history of science by Wilhelm Conrad Roentgen in 1895. The X-ray tube basically consists of a filament which can be heated by electric current. On heating the filament electrons are produced. This bunch of electrons can be accelerated by applying high voltage. It can be directed towards a target material. These accelerated electrons incident or falling on the target material ejects inner shell electrons from the target material. Transition of inner shell electrons from the target material lead to the production of characteristic X-rays. Most commonly used X-rays consist of K_α and K_β lines. Metals like Cu, Fe, Mo, and Cr are used as target materials for the production of X-rays. Copper (Cu) is one of the important target material. CuK_α radiation from copper with a wavelength of 1.5418 Å is mainly used for X-ray diffraction analysis of materials.

The average crystallite size of the samples can be calculated using the Scherrer's formula [Cullity B D *et al*; 2001],

$$d = \frac{0.9\lambda}{\beta cos\theta}$$

where, λ is the wavelength of the X-ray, β is the full width at half maximum (FWHM) intensity in radians and θ is the corresponding angle at which β is taken. The lattice parameter of the crystal structure can be calculated using the (h k l) values and interplanar spacing d, by the following equations.

For cubic system,

$$\frac{1}{d^2} = \frac{h^2 + k^2 + l^2}{a^2}$$

Tetragonal system,

$$\frac{1}{d^2} = \frac{h^2 + k^2}{a^2} + \frac{l^2}{c^2}$$

Hexagonal system,

$$\frac{1}{d^2} = \frac{4}{3}\left(\frac{h^2 + hk + k^2}{a^2}\right) + \frac{l^2}{c^2}$$

X-ray diffraction analysis gives information about the crystal structure, average crystalline size, orientation etc. The obtained X-ray diffraction patterns are compared with the standard diffraction files reported by **Joint Committee on Powder Diffraction Standards** (**JCPDS**) or **International Centre for Diffraction Data (ICDD).**

In the present study, the X-ray diffraction measurements of the samples were carried out with a Rigaku D Max-C X-ray diffractometer using Cu Kα radiation (λ =1.5418 Å) [Figure 2.2].

Figure 2.2. *Rigaku Geigerflex D Max diffractometer with CuKα radiation (λ=1.5414 Å) used for the analysis of the samples under study.*

Surface morphology

Surface morphology of the samples is one of the important properties of the material. Scanning Electron Microscopy (SEM) is an electron microscopic technique for imaging the surface of materials.

2.5.2. Scanning Electron Microscope (SEM)

A scanning electron microscope (SEM) scans and images the surface of solid materials with beam of electrons. The basic principle of electron microscope is that the electrons will interact with the atoms of the material. The resulting signals contain information about the surface morphology, topography, composition and other properties such as electrical conductivity of the sample [Watt M; 1997]. Data is collected from a selected area of sample's surface and 2-dimensional image of the sample surface is generated from these signals.

The interaction of electrons with the surface of the samples contain secondary electrons, back scattered and diffracted backscattered electrons, X-rays, light and heat. Secondary electrons and backscattered electrons are commonly used for the imaging purpose. Secondary electrons give information about the morphology and topography of the samples. Backscattered electrons usually give contrasts in images related to its composition. Scanning electron microscopes are capable of producing high resolution images of the surface of the sample. Some SEM can give images of the particles below 10 nm. In a scanning electron microscope, electron beams are generated with filaments. Commonly used filament is made of tungsten. The electrons are emitted from the cathode tungsten filament (electron gun) thermionically. These beams of electrons are accelerated towards anode which is positive with respect to filament. This electron

beam has an energy ranging from a few hundred eV to 40 keV. This is allowed to pass through condenser lens and focussed on to a very fine point (1-10 nm in diameter) on the sample by the electromagnetic objective lens. The spatial resolution of the SEM depends mainly on the size of the focussing spot. This focussed electron beam is allowed to hit the sample surface which generate secondary electrons as well as back scattered electrons. Detector is used to collect these electrons converted to voltage, amplified and converted to image.

In the present studies A JEOL model JSM-6390LV scanning electron microscope (SEM) and a Carl Zeiss sigma FE-SEM [Figure 2.3] was used for the morphological analysis of the samples.

Figure 2.3. *Carl Zeiss sigma field-emission scanning electron microscope (FE-SEM) used for the analysis of some of the samples under study.*

Compositional analysis

2.5.3. Energy Dispersive X-ray (EDX) Analysis

The energy dispersive X-ray analysis also referred as EDX or EDAX or EDS is the technique used to identify the elemental composition of a

sample. The EDAX analysis system usually attached or integrated to a scanning electron microscope (SEM) [Flewitt P E J *et al;* 2003 and Schroder D K; 1998]. During the SEM measurement, the material is bombarded with an electron beam. When a high energy electron beam is incident on the sample material, characteristic X-rays are produced from the material. Analysing the energy of the emitted X-rays from the sample the elemental composition of the sample under study can be understood. Generated X-rays are named according to the replacement of outer electrons with the displaced inner-shell electrons of elements. When an electron from the K-shell is ejected, this is then replaced by the electron in the L-shell which produces Kα-X-rays. If it is replaced by M shell electrons, K_β X-rays are produced [Williams D *et al;* 1995]. Lighter elements usually analysed with K lines. The threshold energy for ejecting electron from K-shell increases with atomic number and using K-lines to excite heavy elements are not always possible. In order to detect heavier elements, L-series or M-series X-rays are used [Williams D *et al;* 1995].

Main components of EDAX equipment includes a solid state detector, X-ray processing circuits (pulse processor, preamplifier, energy to digital converter and multi channel analyser) and a data processing unit consists of computer with suitable software. The solid-state detectors can measure X-ray energies in a range 1-20 keV. By measuring the energy of emitted X-rays by a material during electron bombardment, we can identify the atom from where the X-rays are emitted. Peaks in EDAX spectrum corresponds to the energy level for which the X-ray is received by the detector. Each peak represents a unique atom which in turn shows the presence of that particular element. Intensity of the peak corresponds to the concentration of that particular element present in that material.

2.5.5. Transmission Electron Microscope (TEM)

Transmission Electron Microscopy (TEM) is an important three dimensional imaging technique with the aid of electron beams. Transmission electron microscopy is used to determine the shape, size, topography, morphology and the structure of the material. It is almost similar to SEM. TEM images are having high resolution compared to light microscopes and is due to the shorter de Broglie wavelength of the electrons. High resolution TEM can examine even at the atomic level which is thousands of times better resolved than ordinary light microscopes. A beam of electrons is transmitted through the sample, which is then interacts with the sample. An image of the sample can be obtained by focussing the interacted electrons on a photographic film or with a charge coupled device (CCD) camera. The quality of transmitted electron beam depends on the properties of the material under study. The main components of a TEM include an electron source, electromagnetic lenses, aperture, sample holder, and a detector of imaging system. The electron source comprises an anode and a cathode. The electron generation is either by thermionic discharge or by field emission. These electrons are accelerated with high voltage of the order of 100 keV using electric field and focussed on to the sample under investigation by means of electromagnetic lenses. The focussing of electrons by the electromagnetic lenses provides much more resolution with improved depth of vision. The detection of transmitted electron beam can be done by a photographic film or fluorescent screen such that the areas where electrons are scattered appears to be dark on the screen [Flewitt P E T *et al;* 2003]. The accelerated electron beam penetrate through the sample, the transmitted and diffracted electrons are analysed to generate a two dimensional projection of the sample. The diffracted electrons provide the

contrast in the image [Watt M; 1997]. It can generate two types of images, dark field and bright field. This can be achieved by means of suitable placing of objective aperture. In the bright field TEM analysis, transmitted electrons generate bright regions whereas the diffracted electrons form dark regions. The diffracted electrons form the image in dark field image analysis. One of the greatest advantages of TEM is the high resolution or magnification which ranges from 50 to 10^6. The resolution of TEM is given by

$$\boldsymbol{L = \frac{h}{\sqrt{2qmV}}}$$

Where, 'h' is the Planck's constant, 'V' is the electron accelerated potential difference, 'm' is the mass and 'q' is the charge of electron. The high resolution transmission electron microscope (HRTEM) [Figure 2.4] can produce the image of the sample at the atomic level since its resolution is 1 nm or even smaller [Subramanian A *et al;* 2004]. Using HRTEM images grain size of the samples especially for nanoparticles, can be determined. The parallel lines appeared in the HRTEM images corresponds to the planes of the crystal lattice and the distance between them is its'd' spacing.

Figure 2.4. *A typical FEI Tecnai transmission electron microscope (http1)*

2.5.5a. Selected area electron diffraction pattern (SAED)

Selected Area Electron Diffraction (SAED) is a new generation analytical technique. This technique is particularly used for the crystallographic studies of nanoparticles in which electron beams with shorter wavelength is used as source. SAED detector set up is usually attached with TEM. SAED pattern gives information about various crystalline planes corresponds to that particular material. SAED pattern usually consists of arranged spots originated from different crystallographic planes. Single crystalline materials are expected to give spots, but in the case of polycrystalline materials especially in nanomaterials, concentric rings are observed. The d spacing can be calculated from the rings using the relation

$$\boldsymbol{Dd = L\lambda}$$

Where, D is the ring diameter, d is the interplanar spacing, λ is the de- Broglie wavelength and L is the effective camera length [Flewitt P E J *et al;* 2003].

Optical studies

2.5.6. UV-Vis-NIR Spectroscopy

In a UV-Visible spectrophotometer, a given wavelength of light is allowed to pass through the sample. The incident radiation interacts with the sample gets absorbed, scattered and transmitted. The UV-Vis spectroscopy detects and analyses the transmitted light. This technique is actually complimentary to fluorescence spectroscopy in which the absorption measures transition from ground to the excited state. Here the incident photons with energy greater than the band gap energy of the material will be absorbed while those with less than band gap energy will be transmitted. Based on this one can measure the band gap of the material under study [Streetman B G; 1995].

The basic law governing this is the Beer-Lambert law. Based on this law, the absorption coefficient can be related as

$$I = I_0\, e^{-(\alpha)t}$$

Where '*I'* is the transmitted intensity, I_0 is the incident intensity of the light and '*t'* is the thickness of the sample. The plot $(\alpha h\nu)^2$ versus hν will give the value of band gap energy.

2.4.6a. Diffuse Reflectance Spectroscopy (DRS)

Diffuse reflectance spectroscopy is the measurement of diffused radiations that are reflected at a number of angles from the uneven or granular surface of solid materials. Reflection from the surface of single crystallites is specular reflection whereas, the reflection arises from the penetration of radiation in to the interior of the solid, gets scattered many times and re-emerges to the surface. So diffuse reflectance spectroscopy deals with one of the two reflected radiation namely, specular reflected radiation (Rs) and diffusely reflected radiation (Rd). The reflected radiations of DRS have the features from transmission, scattering, specular and internal reflectance. Thus DRS spectrum exhibits absorbance as well as reflectance features.

The diffuse reflectance phenomena are described by several models based on the optical properties of the material. Among these, Kubelka-Munk model proposed in 1931 is widely accepted for the DRS analysis. Based on this model the intensity of the reflected light depends on the absorption coefficient (k) and the scattering coefficient (s). By using Kubelka-Munk relation, we can convert reflectance data to absorbance [Kubelka P *et al;* 1948, Kubelka P *et al;* 1931].

The Kubelka-Munk function states that,

$$log\ [(\frac{(1-r)^2}{2r})] = log\ k - log\ s$$

$$\text{where, } r = \frac{R\ (sample)}{R\ (standard)}$$

The material with reflectance almost unity is used as the standard. In the present studies, $BaSO_4$ is used as the standard and R (standard) is taken as unity. The Kubelka-Munk relation will be simplified to,

$$\frac{(1-R)^2}{2R} = \frac{k}{s}$$

A graph is plotted taking the values $[(k/s)hv]^2$ on y-axis and hν (photon energy) on x-axis. The band gap of the material is estimated by extrapolating the linear portion of the graph to x-axis. For the present studies, the DRS measurements were recorded using a JASCO V 570 spectrophotometer [Figure 2.5].

Figure 2.5. *JASCO V 570 spectrophotometer used for the analysis of samples under study.*

2.5.7. Photoluminescence (PL)

The basic idea about the photoluminescence mechanism in semiconductors is already explained in chapter 1. Regarding the instrumentation part of luminescence, two types of luminescence spectra are to be explained, which includes excitation and emission spectra. In measuring the excitation spectrum, the excitation wavelength range is scanned by fixing the emission wavelength. Here, the wavelength that causes fluorescence is identified and the sample is illuminated with that wavelength. By fixing the emission wavelength, the material is scanned through wavelength of excitation and its intensity is measured [Shinde K N *et al;* 2012]. Similar to the absorption spectrum, the excitation spectrum gives the position of energy levels in the excited states. On the other hand, the emission spectrum gives the spectral distribution of the wavelength that emitted by the sample. Here the sample is excited with a wavelength corresponding to or greater than the band gap energy, and the emission from the sample is collected over a wavelength region [Vij D R; 1998].

PL spectrometer consists of an excitation source, sample holder and detecting system. Xenon lamp is a commonly used as excitation source from which desired wavelength of excitation is selected by means of a grating. The sample holder can handle powder, solid, liquid as well as thin film samples. The detecting system is usually a photo detector since quantum yield from the materials is high compared to other spectroscopic techniques. Nowadays, laser beam with different wavelengths like 325 nm, 405 nm and 785 nm etc are also using as excitation source in order to know the precise emission from the material.

In the present studies, the room temperature PL spectra of the samples were recorded by a Horiba Jobin Yvon Lab Ram HR system with a He–Cd laser (excitation wavelength is 325 nm) [Figure 2.6].

Figure 2.6. *Horiba Jobin Yvon Lab Ram HR system used to record the photoluminescence spectra of the samples under study.*

2.5.7a. CIE colour Coordinates

It is an internationally accepted standard for quantifying visible colours. Commission Intenationale de I'Eclairage (CIE) is established in 1931. The accepted standard colour coordinates are known as CIE colour coordinate standards. Interestingly, with the aid of this colour coordinates one can specify entire visible colours and quantify chromaticity from the sample [Wyszecki G *et al;* 1982]. Visible luminescence spectrum from the sample can be represented by means of a CIE colour coordinates on a two dimensional plane. The two major functions which can be used to distinguish light in the 380-780 nm range are human visual system (HVS) and the spectral power density (SPD). CIE tristimulus values (X, Y, Z) are used to calculate CIE colour coordinates [Figure 2.7]. Any of the visible colours can be represented as a combination of three primary colours which

is represented as tristimulus values (X, Y, Z). The tristimulus values are obtained by integrating the product of the light source P(λ) and the standard CIE colour matching functions $x_\lambda(\lambda)$, $y_\lambda(\lambda)$ and $z_\lambda(\lambda)$ over the entire visible range [BiIlmeyer F W *et al;* 1981]. Since the spectral values are discrete, calculation relation can be represented as,

$$X = \sum_{\lambda=380\ nm}^{780\ nm} x_\lambda\,(\lambda)\ P(\lambda)\Delta\lambda$$

$$Y = \sum_{\lambda=380\ nm}^{780\ nm} y_\lambda\,(\lambda)\ P(\lambda)\Delta\lambda$$

$$Z = \sum_{\lambda=380\ nm}^{780\ nm} z_\lambda\,(\lambda)\ P(\lambda)\Delta\lambda$$

Here Δλ is the interval between points.

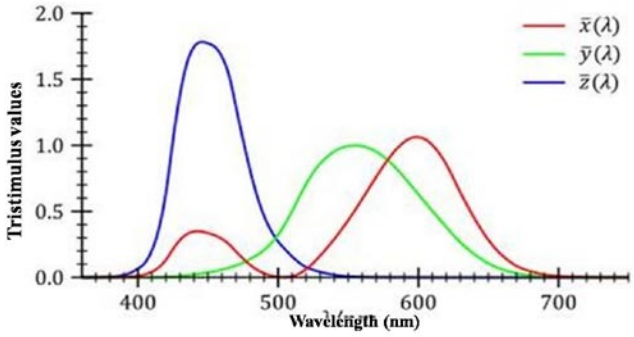

Figure 2.7. *Plot of the CIE tristimulus (x, y and z) functions (http2)*

After the calculation of tri-stimulus values, the CIE coordinates are calculated using the relation

$$x = \frac{X}{X + Y + Z}$$

$$y = \frac{Y}{X + Y + Z}$$

$$z = \frac{Z}{X + Y + Z}$$

In the CIE colour coordinate representation, only x and y values are reported since x + y + z = 1, only two of the three coordinates are independent. The position of the colour in CIE chromaticity diagram is obtained by plotting the x and y values [Figure 2.8].

For white colour, the CIE coordinates is (x, y) = (0.33, 0.33).

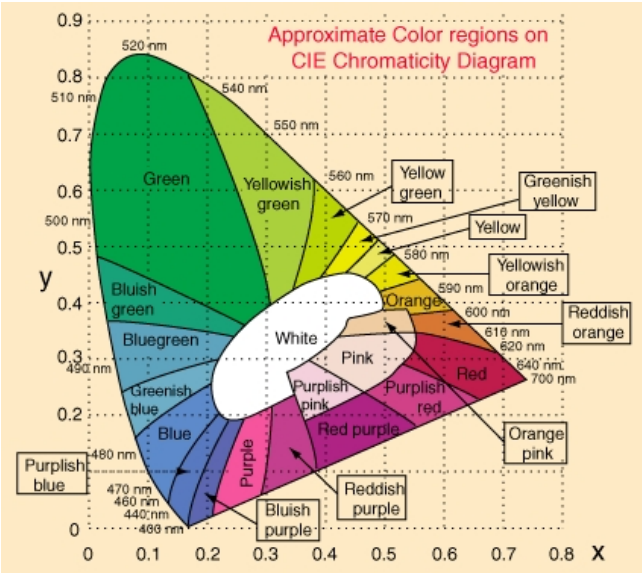

Figure 2.8. *The CIE chromaticity diagram (http3)*

2.5.8. Fourier Transform Infrared (FTIR) Spectroscopy

Infrared (IR) radiation in the electromagnetic spectrum is an important region. This radiation can be effectively used for the characterisation of the material. The IR radiation can be divided in to three regions; one is 50 to 400 cm^{-1} usually referred as far IR, 400-4000 cm^{-1} is called mid IR and 4000-15000 cm^{-1} is near IR. All these spectral regions can

provide valuable information about the material structure [Banwell C N *et al;* 1994]. The 50 to 400 cm^{-1} region is particularly important for lattice vibrations and metal oxygen bonds with higher order bond length. It also gives information about the rotation of the molecule. On the other hand the mid IR region mainly comprises of molecular vibrations. The far IR region can provide much more information about combinations and overtones of fundamental frequencies [Ingle J D *et al;* 1998].

Each molecule has its own vibration frequency based on its molecular structure and symmetry. In order to obtain IR spectrum from the sample, the dipole moment of the system has to undergo change while interacting with that of the IR radiation. The interaction of IR radiation with the molecule gives the activation of fundamental modes of vibrations corresponding to that molecule. Because of this merits, IR spectroscopy is widely used as a material characterization technique. Most of the modern IR spectrometers collect information from the sample simultaneously without much delay. This collected information is separated in to frequency components by means of mathematical operation Fourier Transform.

In a FTIR spectrometer, a parallel beam of IR radiation from the source is directed to the interferometer. The interferometer consists of two mirrors (M_1 and M_2) and a beam splitter (B). The beam splitter is suitably coated such that half of the radiation goes to mirror M_1 and half to M_2. The reflected radiation beams from both the mirrors move along the same path and are recombined to a single beam at the beam splitter. When we use monochromatic radiation for the measurement, the recombined beam at the beam splitter shows constructive or destructive interference patterns depending on the relative path lengths B to M_1 and B to M_2. The spectrometer records the interference pattern without sample in the beam

and keeps this as background. Measurement is done again as the sample is kept in the beam. The final spectrum will be generated by subtracting the background [Banwell C N *et al;* 1994]. In the present studies, the Fourier Transform Infrared spectrum (FTIR) of the samples were recorded on a SHIMADZU IR Affinity-1 FTIR spectrophotometer using KBr pellet technique with a resolution of 4 cm^{-1} [Figure 2.9]. Sample handling in IR spectroscopy is little bit complicated which may leads to the destruction of original sample. KBr pellet technique is an ideal technique used for the measurement of the sample in the mid IR region. Nowadays Attenuated Total Reflection (ATR) technique is also widely used in which samples are examined directly.

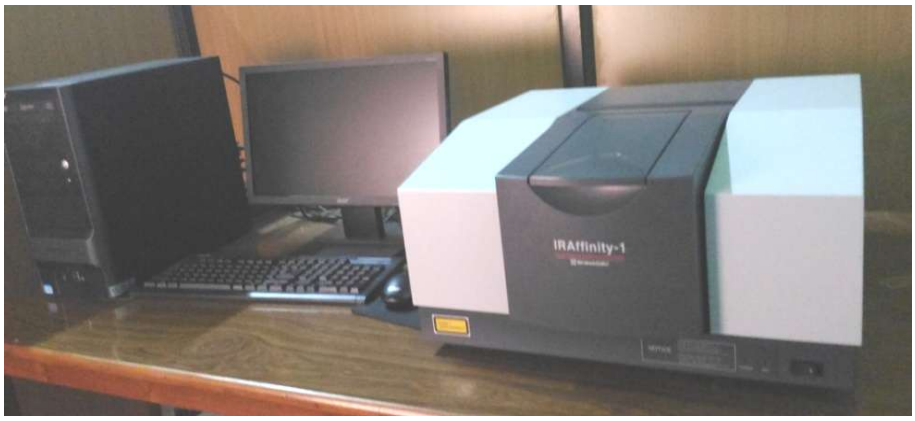

Figure 2.9. *SHIMADZU IR Affinity-1 FTIR spectrophotometer used to analyze the samples under study.*

2.5.9. Fourier-Transform Raman spectroscopy

Raman spectroscopy is one of the non-destructive techniques which give information regarding the presence of functional groups, molecular symmetry, nature of chemical bonds and crystallinity etc. The Raman spectroscopy is based on the Raman effect firstly observed by Sir C. V. Raman in 1928 [Raman C V *et al;* 1928]. When radiations interact with the

molecules, the energy of the scattered radiation will shifted up or down with respect to that of incident radiation. When the incident radiation loses energy to the material the emerging radiation will have lower energy and is called Stokes Raman lines. Anti-Stokes lines have frequency higher than incident radiation. Usually the Stokes lines are more intense than anti-Stokes lines, so the Stokes-mode of Raman scattering is monitored. Since the Raman effect is very weak, different types of laser sources are used for the excitation. Raman spectroscopy reveals the information about the vibrational and rotational motion of the molecules, which can be used to detect the presence of organic and inorganic species.

The Raman spectrometer consists of four major components, which includes, an excitation source (laser), sample illumination system and light collection optics, wavelength selector (filter or spectrophotometer), and a detector (CCD or PMT, photodiode array). Because of the intensity of Raman scattering varies as the fourth power of the frequency, argon and krypton ion sources that emit in the blue and green region have an advantage over the other laser sources. The use of Nd:YAG (1064 nm) laser source is much effective in eliminating fluorescence from the Raman spectrum [Willard H H; 1987]. The Rayleigh scattered light is rejected using a double monochromator. The resulting Raman scattered radiation is detected using a photodetector and photomultiplier [Richter H *et al;* 1981]. Raman spectra of the samples are usually recorded in the range 50-4000 cm^{-1}. Raman spectrum is basically related to the fundamental modes of vibrations. By analysing the Raman spectrum, one can understand the symmetry of the molecule based on Raman activity of the fundamental modes. Vibrational frequencies of the molecule are expected in region 400-4000 cm^{-1}. Rotational as well as lattice modes of the crystal are seen below 400 cm^{-1}. In metal oxide semiconductor system, lattice

vibrations occurs which are basically longitudinal optical (LO) and transverse optical (TO) modes [Tanaka A *et al;* 1992], usually expected below 800 cm^{-1}. The information about vibrational properties, structure, phase, grain size etc can be obtained from Raman spectroscopy. The Raman measurements of bulk samples will not give the acoustic modes because of its low frequencies. Whereas in the case of nanomaterials, acoustic modes can be observed in the frequency range below 100 cm^{-1} [Rajalakshmi M *et al*; 1997 and Tanaka A *et al;* 1993]. The acoustic mode frequency is inversely proportional to the size. The optical phonon confinement results in frequency shift in longitudinal optical (LO) and transverse optical (TO) [Tanaka A *et al;* 1992]. Both infrared spectroscopy and Raman spectroscopy are complimentary to each other. Light scattering is measured in Raman spectroscopy whereas photon absorption is measured in infrared spectroscopy.

Raman analysis of gas, liquid, and solid states can be examined easily. In the present studies, A Horiba Jobin Yvon LabRAM HR system (resolution in the order of 3 cm^{-1}) equipped with a He–Ne laser (632.8 nm) was used to record the Raman spectrum of the samples [Figure 2.10].

Figure 2.10. *Horiba Jobin Yvon Lab Ram HR system used to record the Raman spectra of the samples under study.*

3 Synthesis of Cubic Phase ZnS Particles by Hydrothermal and Solvo-hydrothermal Method

Chapter

3.1. Introduction

Modern technology demands new UV sources especially for scintillation devices [Choube S R *et al;* 2012], CD read heads for reducing data storage space and for bio-imaging applications [Mehta S K *et al;* 2010a]. ZnS is a semiconductor material with large exciton binding energy of about 40 meV at room temperature [Tran T K *et al;* 1997]. Among the different phases of ZnS, cubic sphalerite phase having bandgap of the order of 3.68eV which is suitable to fabricate UV sources operating at ambient conditions [Fujiwara H *et al;* 1998, Taghvaei V *et al;* 2010, Xu J *et al;* 1999, Sun L *et al;* 1999, Yue G H *et al;* 2006, and Zapien J A *et al;* 2004]. ZnS is also best suited for biological systems and applications, since it is less toxic as compared to lead and cadmium compounds [Chatterjee A *et al;* 2007]. Even though, there is a great interest on the photoluminescence properties of 1D ZnS nanostructures, a few studies are available in the literature on possible UV emission at room temperature. The reported UV emission from ZnS are at 365 [Bodo B *et al;* 2010], 322 [Cheng C *et al;* 2006], 333 [Meng X M *et al;* 2003], 375 [Chae W S *et al;* 2004], 374 [Yuan H J *et al;* 2003] and at 380 nm [Li J *et al;* 2006], and these are having less applications in device fabrication because of feeble emissions nature. Enhanced optical properties on ZnS nanocrystals is also obtained by using capping agents and surfactants like TOPO (Trioctylphosphine oxide) [Malik

M A *et al;* 2001 and Manna L *et al;* 2002], chitosan [Sharma M *et al;* 2010], ethylenediamine, odecylthiol [Zhao Q *et al;* 2003], 1-ethyl-3-methylimidazolium ethyl sulphate [Taghvaei V *et al;* 2010], DDAB (Didodecyldimethylammonium bromide) [Li G *et al;* 2010] during synthesis process. Even though the band to band edge emission of ZnS fall in the UV-region, majority of the chemically synthesized ZnS exhibits emission in the region 400-450 nm or, while with doping in the region 500-600 nm [Zhang X *et al;* 2005]. This is mainly due to high sensitivity of the 1D ZnS nanostructures optical properties to the synthetic conditions.

More interestingly, mesoporous materials attained much attention because they possess more active sites with abundant inner spaces and surface area. These materials likely to have better technological performance and useful for the applications in the field of nanodevices, catalysts, sensors, drug delivery etc [Xue K *et al;* 2010 and Xing R *et al;* 2012]. The synthesis of mesoporous ZnS structures is achieved mostly by using surfactants as well as templates [Xue K *et al;* 2010]. Xing *et al* [Xing R *et al;* 2012] used PVP, and Zhang *et al* employed ethylene glycol as surfactant for the synthesis of mesoporous ZnS structures [Zhang Q *et al;* 2012]. Template free solvothermal and hydrothermal method is also getting more attraction, because it is a low-cost method for the synthesis of large scale materials [Muruganandham M *et al;* 2010]. In hydrothermal synthesis process, water is used as solvent for reactants. But the presence of OH radical in the water generally contribute to higher amount of oxygen and sulphur related defects, which results in intense emission in the green and orange region of the spectrum. So this in turn will reduce the intensity of band- to-band UV emission. The present work focuses on hydrothermal and solvo-hydrothermal synthesis of ZnS particles, in which relatively oxygen

free mesoporous cubic phase of ZnS particles were synthesized via solvo-hydrothermal method using water-acetonitrile solution combination.

3.2. Experimental

3.2.1. Synthesis

All the chemicals used for the present synthesis were AR grade. In the present work we used, water-acetonitrile solution combination as a solvent for solvo-hydrothermal reaction. ZnS crystals were synthesized by the reaction of zinc acetate $Zn(CH_3COO)_2.2H_2O$ (0.2 M), and Na_2S(1M). Zinc acetate and Na_2S were taken in separate beakers and dissolved in 40 ml of water-acetonitrile solution (1:1 ratio), each separately. These solutions were allowed to dissolve by constant stirring using a magnetic stirrer for 5 min. Then the two solutions were mixed suddenly and allowed to stir for 1 hr and were transferred to a teflon lined sealed stainless steel autoclave and heated at 200 ^{0}C for a growth time of 12 hrs. After the heating process, the autoclave was allowed to cool naturally to room temperature. The precipitates were filtered out and washed with distilled water and ethanol and dried in air atmosphere.

3.2.2. Characterization

As synthesized samples were characterized by Rigaku (D Max C) X-ray diffractometer, using CuKα radiation (λ = 1.5418 Å) with a scanning speed of 5^0/min in the 2θ range 10^0-80^0. Raman spectra of the samples were recorded with a Horiba Jobin Yvon Lab Ram HR system with He-Ne laser (632.8 nm) as the excitation source with a resolution better than 3 cm^{-1}. The morphological characterization and elemental analysis (SEM-EDAX) of the sample was carried out by JEOL Model JSM-6390LV and JEOL Model JED-2300. TEM images of the sample were recorded with FEI Tecnai G^2 20

S-TWIN, 200 keV Transmission Electron Microscope. UV–visible spectrum was recorded with a Jasco V-570 spectrometer in the wavelength range 220–800 nm and the room temperature photoluminescence (PL) of the sample was recorded by a Horiba Jobin Yvon LabRam HR system with the He–Cd laser (excitation wavelength 325 nm).

3.3. Results and Discussion

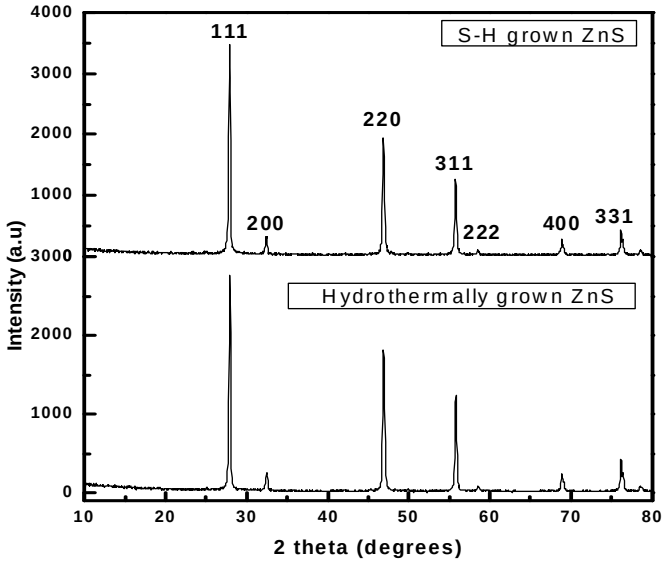

Figure. 3.1. *XRD patterns of hydrothermally grown ZnS and solvo-hydrothermally grown mesoporous ZnS at 200 °C.*

Figure.3.1 show the X-ray diffraction patterns recorded from the solvo-hydrothermally and hydrothermally grown ZnS samples. The X-ray diffraction pattern of the sample shows the formation of cubic sphalerite (zinc blende) ZnS phase (JCPDS 05-0566) with lattice constant 'a' = 5.406 Å for S-H grown and *'a'* = 5.525 Å for hydrothermally grown ZnS [Li Y *et al;* 2008]

Zinc blende structure of ZnS belongs to the T_d (43m) point group [Cheng Y C *et al;* 2009]. The first order Raman spectra of zinc blende ZnS have transverse optical (TO) and longitudinal optical (LO) modes which lies

below 1000 cm^{-1} [Cheng Y C *et al;* 2009]. In the present study, we obtained Raman bands (Figure.3.2) at 286 and 349 cm^{-1} corresponds to TO and LO zone center phonons of cubic ZnS [Kumar S S *et al;* 2006]. The weak nature of the Raman peak at 286 cm^{-1} confirms the cubic structure of the sample [Kumar S S *et al;* 2006]. It is reported that both TO and LO modes of zinc blende structure are allowed for scattering from (1 1 1) face only, TO from (1 1 0) face and LO mode is from (1 0 0) face [Kumar S S *et al;* 2006]. The intense XRD peak at 27.9^0 indicates that the sample is highly crystalline and oriented in (111) plane. Raman LO, TO modes are originated from the scattering of (1 1 1) plane and is in agreement with our XRD observation.

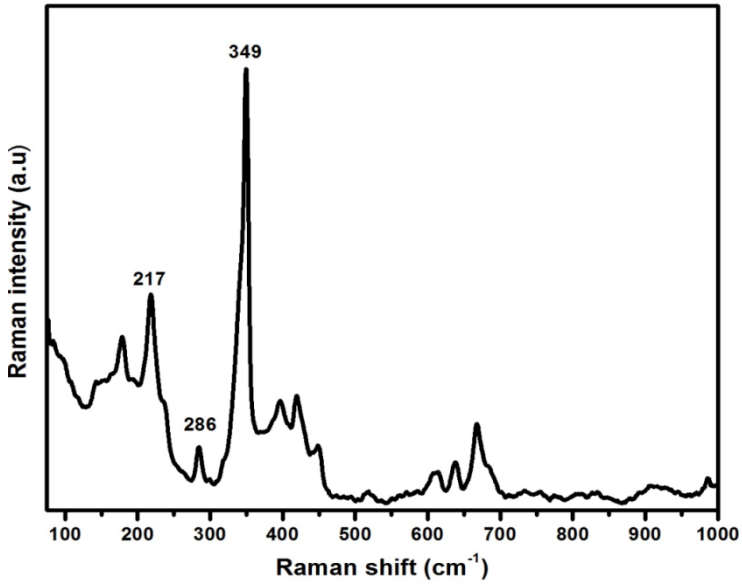

Figure. 3.2. *Raman spectrum of solvo-hydrothermally grown mesoporous ZnS at 200 °C.*

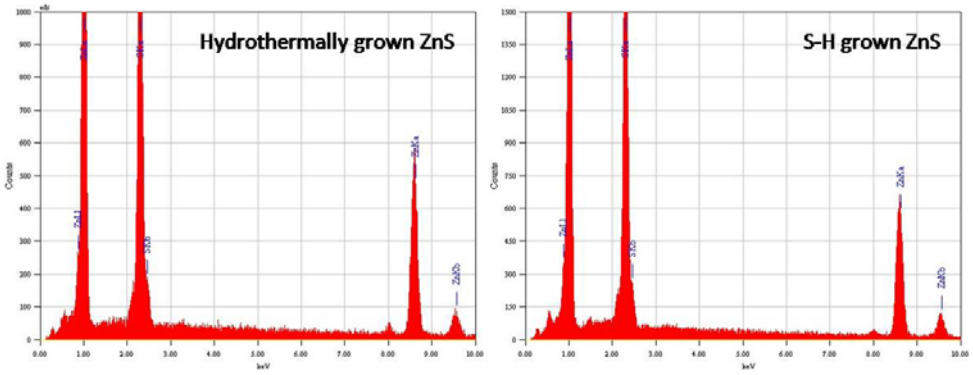

Figure. 3.3. *EDAX spectra of hydrothermally grown ZnS and solvo-hydrothermally synthesized mesoporous ZnS at 200 °C.*

The EDAX (Figure.3.3) spectra of the samples show the presence of sulphur and zinc further supports our XRD observations.

Table 3.1. *EDAX spectral data of hydrothermally grown ZnS and solvo-hydrothermally synthesized mesoporous ZnS at 200 °C.*

Sample	Zn	S
	Atom %	Atom %
Hydrothermally grown ZnS	49.23	50.77
Solvo-hydrothermally grown ZnS	45.74	54.26

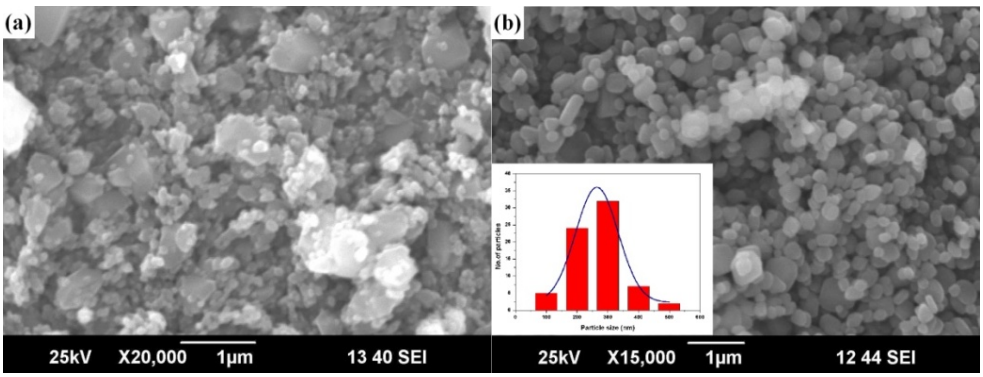

Figure. 3.4. *SEM images of (a) hydrothermally grown ZnS, (b)solvo-hydrothermally grown mesoporous ZnS at 200 °C (Inset shows the particle size distribution histogram).*

Figure 3.4 (a) and (b) is the SEM image of the ZnS sample prepared by using water and water-acetonitrile (1:1 ratio) as solvent respectively. From the SEM images, one can see that the morphology of the sample is getting elliptical/spherical nature and with less agglomeration when water-acetonitrile combination is used. The particle size distribution histogram (showed in the inset of Figure. 3.4b) shows that the average particle size is around 265 nm.

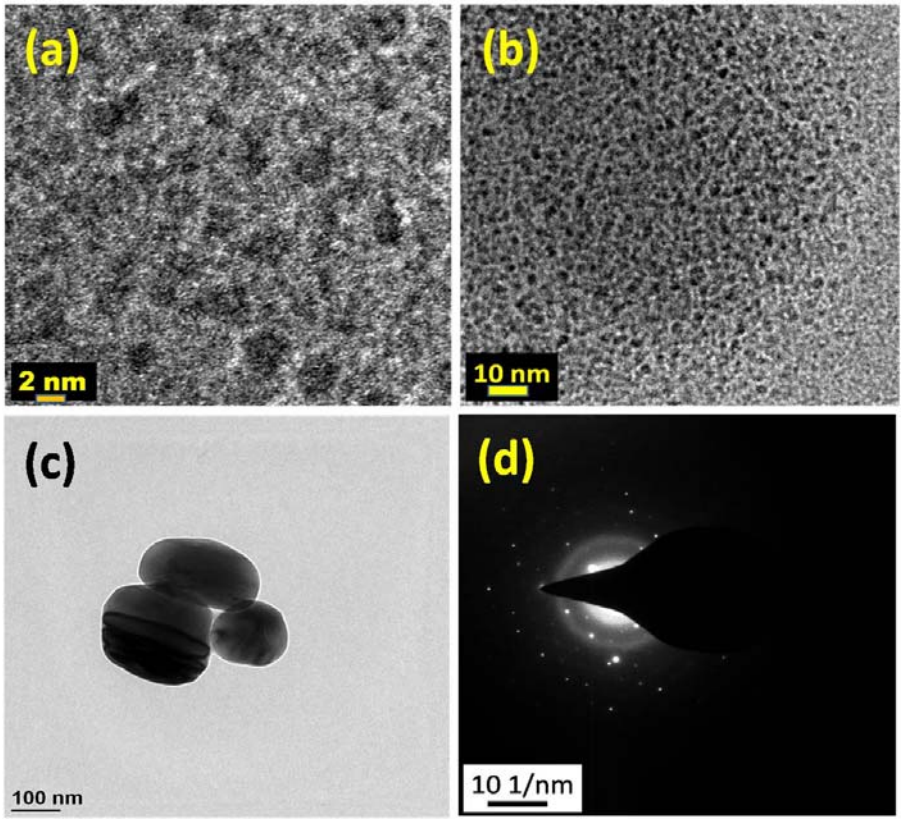

Figure. 3.5. *HRTEM images (a, b, c) and SAED (d) pattern of solvo-hydrothermally synthesized mesoporous ZnS at 200 °C.*

Figure.3.5 shows the HRTEM images of the prepared mesoporous ZnS sample and figure. 3.5d depicts its SAED pattern. One can see the porous nature of the as prepared material from the TEM images.

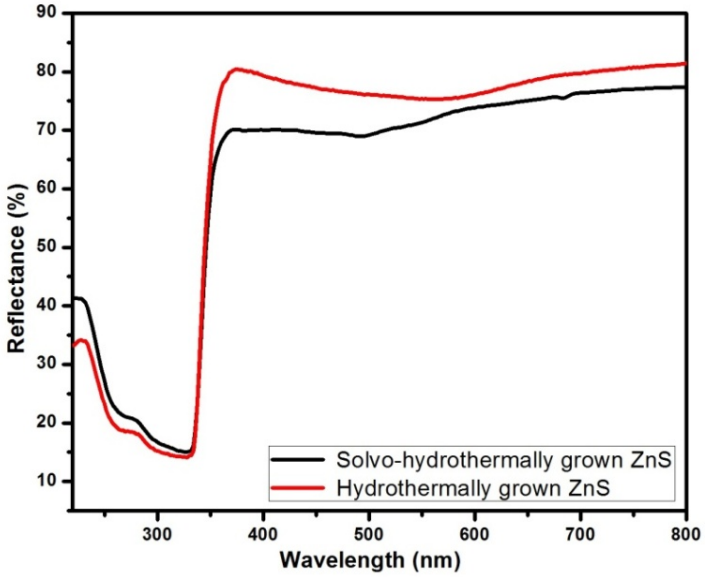

Figure. 3.6. *UV-Visible reflectance spectra of hydrothermally grown ZnS and solvo-hydrothermally synthesized mesoporous ZnS at 200 °C.*

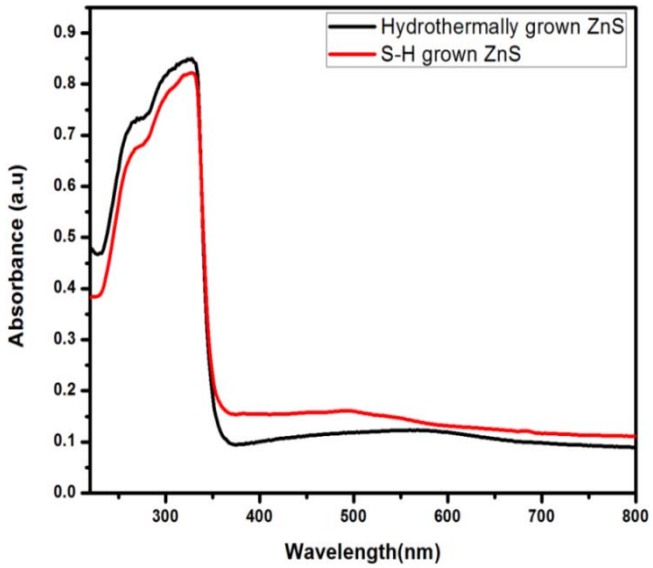

Figure. 3.7. *UV-Visible absorption spectra of hydrothermally grown ZnS and solvo-hydrothermally synthesized mesoporous ZnS at 200 °C.*

Figure.3.6 shows the UV-Visible reflectance spectra and figure 3.7 shows the UV-Visible absorption spectra recorded from the prepared ZnS samples. The steep absorption edge in the vicinity of 332-370 nm represents the transition between valence and conduction band usually seen in direct band gap semiconductors like ZnS. Further the observed absorption shoulder represents the presence of discontinuous energy levels in the band gap [Li Y *et al;* 2008]. From the absorption spectra of the samples, a sharp absorption edge is observed at 340 nm which is same as reported in bulk ZnS [Peng L *et al;* 2010]. The bandgap of the sample is calculated by using Kubelka-Munk relation and is found to be 3.64 eV.

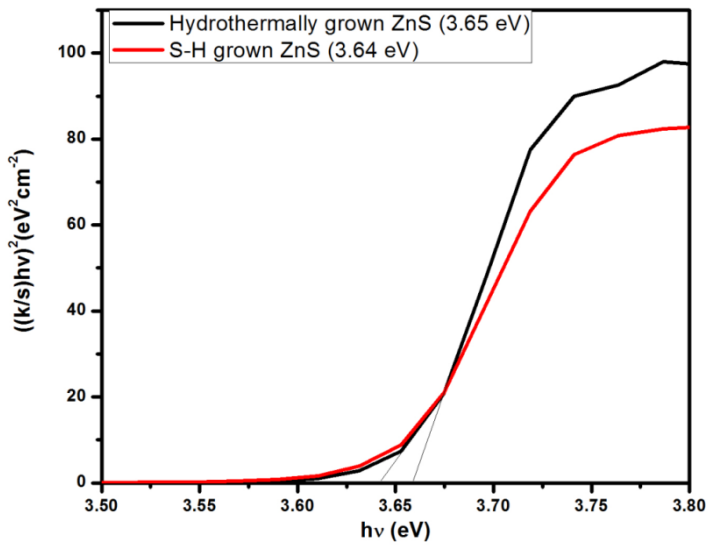

Figure. 3.8. *Tauc plot of solvo-hydrothermally synthesized mesoporous ZnS and hydrothermally grown ZnS at 200 °C.*

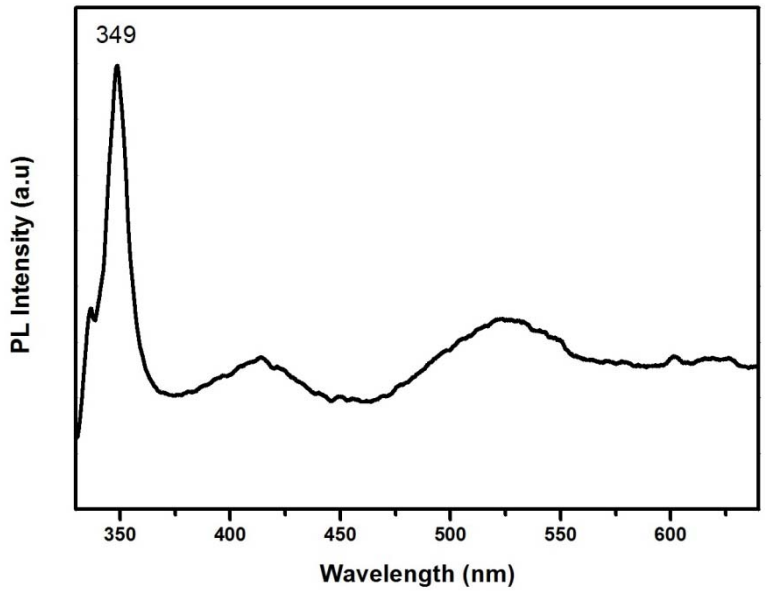

Figure. 3.9. *Room temperature photoluminescence spectrum of solvo-hydrothermally grown mesoporous ZnS at 200 °C.*

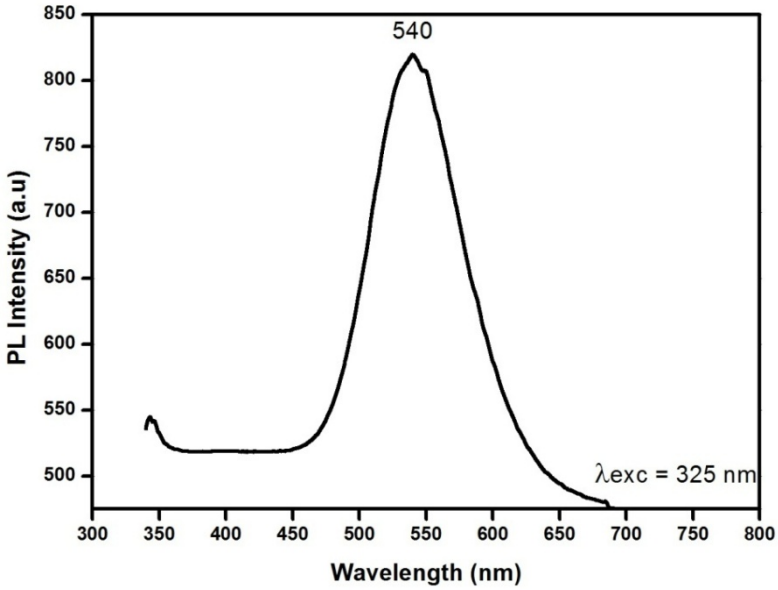

Figure.3.10. *Room temperature photoluminescence spectrum of hydrothermally grown ZnS at 200 °C.*

Figure.3.9 depicts the photoluminescence (PL) spectrum recorded from solvo-hydrothermally synthesized ZnS sample with an excitation wavelength of 325 nm and figure 3.10 is that of hydrothermally grown ZnS. As reported in the literature, the PL emission in ZnS is contributed to different mechanisms viz. near-band edge (NBE) in the region 320–370 nm which is known to be originated from band-to-band, or excitonic transition or quantum size effect. The violet (390 to 400 nm) emission is attributed to deep levels such as Zn^{2+} vacancies, S^{2-} interstitials and dislocations. The blue (430–470 nm), emission is associated with the trapped luminescence arising from the Zn^{2+} vacancies and S^{2-}vacancies [Park S *et al;* 2012]. But the green (510–550 nm) emission is due to the presence of defect levels contributed to dopants or impurity atoms. This emission may also contribute to the electron transfer from sulfur vacancies to interstitial sulfur states [Wang X *et al;* 2011]. In the present samples, the intense green emission at 540 nm from hydrothermally grown ZnS is attributed to the electron transfer from sulfur vacancies to interstitial sulfur states. The PL spectrum shows highly intense emission peak in the UV region at 349 nm with a feeble shoulder peak at 336 nm, weak and broad profiles at 416 and 523 nm. The weak green emission at 523 nm from the sample under investigation can be associated with the electronic transfer from sulphur vacancies to its interstitial states [Wang X *et al;* 2011]. The SEM (Figure 3.4b) and HRTEM (Figure 3.5) images reveals that these microstructures are made of mesoporous nano regime structures which can generate UV radiation correspond to its band gap when this system is suitably pumped by a radiation having higher frequency. Thus generated UV radiation will be amplified by the whispering gallery modes (WGM) of elliptical microstructures [Okazaki K *et al;* 2012]. So the unusual enhancement in the

UV radiation at 349 nm is partially contributed to WGM activation of ZnS microstructures. The observed excitonic UV emission at 349 nm from the present sample is not reported so far in any of the ZnS structures. So the present material has potential application in order to fabricate devices for the production of 349 nm UV sources [Chatterjee A *et al;* 2007].

3.4. Conclusions

In summary, relatively oxygen free mesoporous ZnS microstructures are synthesized by solvo-hydrothermal method. XRD and Raman studies of the samples reveals that hydrothermally and solvo-hydrothermally grown ZnS is having cubic sphalerite phase of ZnS. Boosted UV emission at 349 nm is observed from the ZnS prepared by the solvo-hydrothermal route whereas PL emission at 540 nm is observed from hydrothermally grown ZnS. The increased intensity of the UV emission from S-H grown ZnS is probably attributed to activation of whispering gallery modes (WGMs) of almost elliptical microstructures made of porous nanostructures. This material with the complete elimination of defect related emissions can be used for the fabrication of LEDs, UV lasers and in medical field.

4 Synthesis of Manganese Doped ZnS Nanoparticles by Hydrothermal and Solvo-hydrothermal Method

Chapter

4.1. Introduction

Semiconductor based white light sources attained much attention because of their high luminous efficiency, brightness, low power consumption [Lu X *et al;* 2010] and environmental safety [Dillip G R *et al;* 2013]. Further, warm white light emitting sources are also a new generation product which are being fabricated by using ultraviolet light emitting diode (UV-LED) chip (350–420 nm) coated with blue-green and orange-yellow phosphors. The rare earth based phosphors used for the fabrication of white LEDs (WLEDs) has week red spectral emission. This week emission in turn contribute to high correlated colour temperature (T_c>4500 K) and low colour rendering indexes (R_a<80) which are undesirable [Guo N *et al;* 2013 and Dillip G R *et al;* 2014]. On the other hand most of the warm white light emitting phosphors are nitride and oxynitride based materials. Further inert atmosphere is required for the production of these materials and are costly. Yellow-orange emitting sources are used in combination with blue light emitting InGaN for the generation of WLEDs commercially. Alternatively, ZnS based phosphors like ZnCdS:Ag, Cl (red) [Huh Y D *et al;* 2004], ZnS:Cu, Al (green) [Kao C C *et al;* 2009], and ZnS:Ag (blue) [Kajiwara K *et al;* 2003], etc with different colours are also used for making warm white light sources and WLEDs. High luminescence efficiency of the material is a pre-requisite in order to get better performing white light sources. ZnS:Mn

shows emission in the yellow-orange region [Moritz M G *et al*., 2013, Labiadh H *et al;* 2013, Hoa T T Q *et al;* 2011 and Huang Y *et al;* 2011]. Its energy bands and luminescence centers can be tuned by changing the doping concentration [Ma X *et al;* 2011]. Hydrothermally synthesized Mn doped (0.5, 1, 3, 10 and 20 wt%) ZnS shows a 495 nm (blue) and orange emission at 587 nm attributed to the $_4T_1$ - $_6A_1$ transition of Mn [Hoa T T Q *et al;* 2011]. There is a shift in the absorption band edge to longer wavelength and a broad emission at 580 nm is also reported in ZnS doped with Mn [Huang Y *et al;* 2011].

Highly luminescent, non-toxic yellow-orange emitting sources are also important especially for biological labeling, which can replace the presently using labeling materials like ethidium bromide (EtBr). Synthesis condition of the materials is important in relation to its luminescence properties. In the present chapter we are reporting high luminescence yield from the solvo-hydrothermally (water-acetonitrile combination) grown Mn doped ZnS at yellow-orange region and at 367 nm. Further an attempt is made to understand the role of week hydrophobic polar solvent like acetonitrile on luminescence properties of solvo-hydrothermally (S-H) grown Mn doped ZnS nanocrystals.

4.2. Experimental

4.2.1. Synthesis

Manganese (Mn) doped ZnS were synthesized by the reaction of analytical reagent (AR) grade zinc acetate (0.4 M), manganese acetate and sodium sulphide (1M). Zinc acetate (3.4065gm) and manganese acetate (0.1054 gm) were used for the synthesis of Mn 3 nominal weight percentage (wt%) doped ZnS. But 3.3713 gm zinc acetate and 0.1405 gm of manganese

acetate were used for the synthesis of Mn 4 nominal wt% doped ZnS. The Mn 5 nominal wt% doped ZnS were made using 3.3360 gm zinc acetate and 0.1756 gm of manganese acetate. Whereas the amount of sodium sulphide used for the synthesis of all the compounds described in this communication was 3.1216 gm (1M). For the synthesis of Zn:Mn, zinc acetate and manganese acetate were taken together in a beaker and made to 40 ml solution (either using water or water-acetonitrile combination); sodium sulphide is also made to 40 ml solution in water separately. These two solutions were stirred separately for 5 min and mixed together, stirred again for 1 hr. The resulting solution was kept inside a teflon lined sealed stainless steel autoclave and heated at 200 °C for 12 hrs. The precipitates obtained from the reaction process were filtered out and washed with distilled water and ethanol. The precipitates were allowed to dry in air atmosphere at room temperature (30 °C) and again warmed by using hot air oven at 60 °C for 1hr. Water-acetonitrile combination (1:1) was used as the solvent for the synthesis of Mn doped ZnS by S-H method.

4.2.2. Characterization

Details of material characterizations of the present samples are given in chapter 3 (section 3.2.2). The high resolution transmission electron microscopy (HRTEM) images of the samples were recorded using a JEOL JEM-2100 model transmission electron microscope.

4.3. Results and Discussion

4.3.1. XRD analysis of hydrothermally and S-H synthesized Mn doped ZnS.

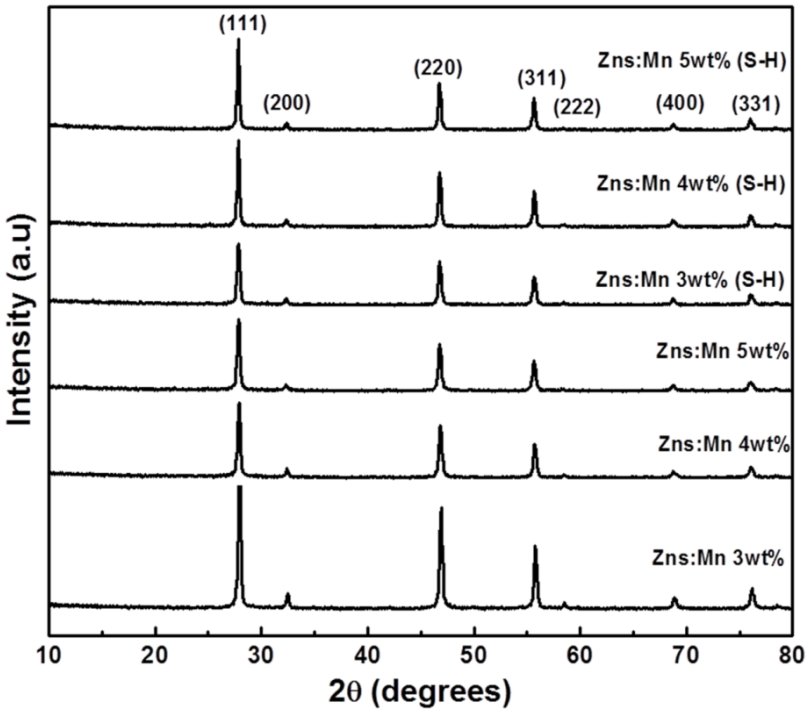

Figure. 4.1. *XRD patterns of hydrothermally and S-H synthesized Mn doped (3, 4 and 5 wt%) ZnS at a reaction temperature of 200 °C.*

The X-ray diffraction patterns (Figure.4.1) of hydrothermally and S-H grown Mn 3, 4 and 5 wt% doped ZnS can be indexed to that of cubic sphalerite ZnS phase with JCPDS 05-0566. The XRD patterns of S-H grown ZnS:Mn is almost identical to that of S-H grown ZnS reported previously [chapter 3]. The calculated lattice constants are found to be matching with that of the standard value 5.406 Å [Li Y *et al;* 2008]. The lattice parameters of all the samples increase slightly with increase in the Mn doping concentration (wt%).

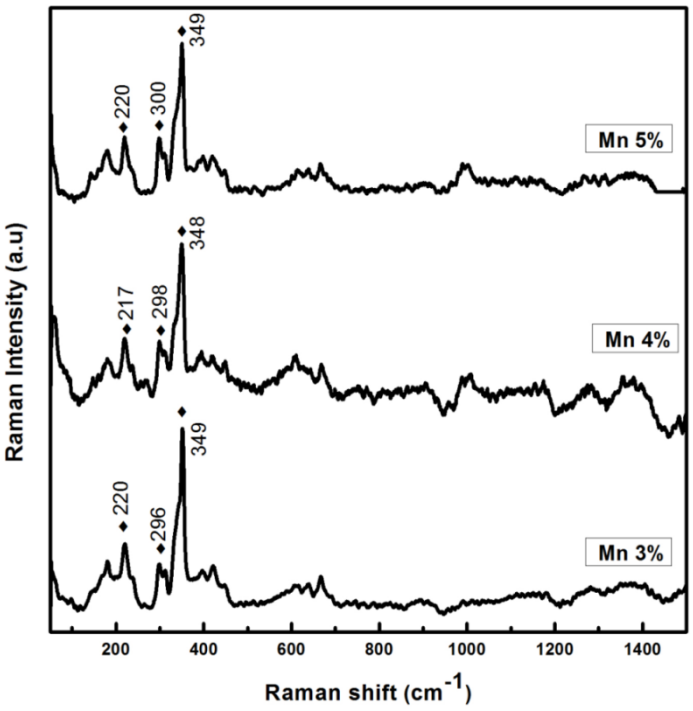

Figure. 4.2. *Room temperature Raman spectra of S-H synthesized Mn doped (3, 4 and 5 wt%) ZnS at a reaction temperature of 200 °C.*

The room temperature Raman spectra of solvo-hydrothermally grown ZnS are shown in figure. 4.2. The Raman bands observed at 349 cm^{-1} is attributed to the LO zone center phonons of cubic ZnS. Whereas the medium Raman bands at 296 (Mn 3 wt%), 298 (Mn 4 wt%) and 300 cm^{-1} (Mn 5 wt%) can be contributed to the TO zone center phonons of cubic ZnS [Cheng Y C *et al;* 2009 and Kumar S S *et al;* 2006]. The strong fluorescence nature of the samples is the reason for the intensity reduction of TO mode as compared to LO mode.

4.3.2. SEM analysis of hydrothermally and S-H synthesized Mn doped ZnS.

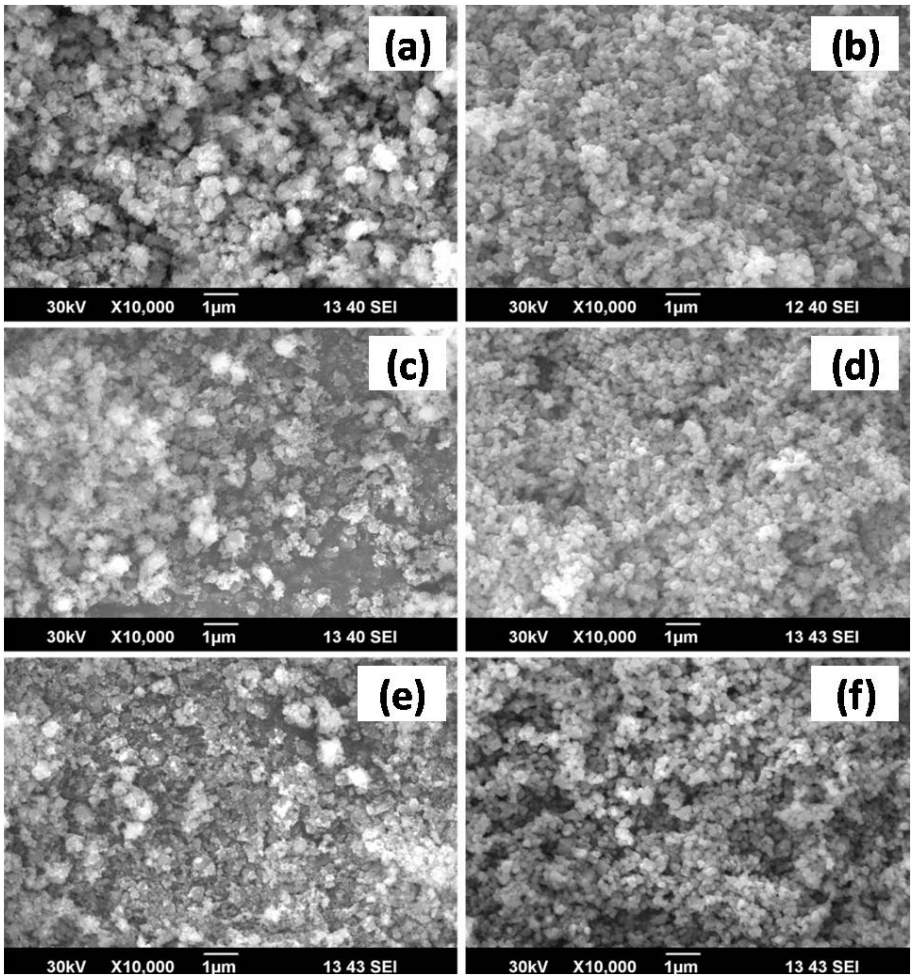

Figure. 4.3. *SEM images of hydrothermally (a) 3 wt%, (c) 4 wt%, (e) 5 wt% and S-H synthesized (b) 3 wt%, (d) 4 wt%, (f) 5 wt%; Mn doped ZnS at a reaction temperature of 200 °C.*

From the SEM images one can see that the morphology of S-H grown Mn doped ZnS are tending to become spherical in nature with less agglomeration unlike its hydrothermally grown counterparts (Figure.4.3). The average crystallite size of the samples was determined from the XRD data using Scherrer equation with respect to major peaks corresponding to

the (1 1 1), (2 2 0) and (3 1 1) planes [Ma X *et al;* 2011 and Li Y *et al;* 2008]. The crystallite size of both the hydrothermally and S-H synthesized Mn doped ZnS samples gets increased as Mn doping wt% increases. Interestingly, the crystallite size of the S-H grown Mn doped ZnS is relatively less than that of hydrothermally grown Mn doped ZnS with the identical doping concentrations (Table. 4.1). In order to know the actual size of the samples, the HRTEM images of the representative samples were taken (Figure.4.4). The particle size and optical properties are likely to change while using different organic solvents for growth process [Ramsden J J *et al;* 1985]. Similarly, crystal structure may change due to the influence of interfacial forces while using organic solvents as a growth medium [Ramsden J J *et al;* 1985]. It is reported that the grain size may increase while increasing the water content in solvo-hydrothermal reaction with acetonitrile-water combination which is in agreement with our observation [Ramsden J J *et al;* 1985].

Table.4.1. *Crystallite size and lattice parameter of the hydrothermally and S-H synthesized ZnS:Mn at a reaction temperature of 200 °C.*

Samples	Average crystallite size (nm)	Standard deviations (±) nm	Lattice parameter (a) Å Unit
ZnS:Mn (3 wt%)	33	1.27	5.535
ZnS:Mn (4 wt%)	37	1.67	5.544
ZnS:Mn (5 wt%)	41	2.49	5.553
ZnS:Mn (3 wt% S-H)	26	2.48	5.554
ZnS:Mn (4 wt% S-H)	31	0.30	5.556
ZnS:Mn (5 wt% S-H)	34	1.27	5.558

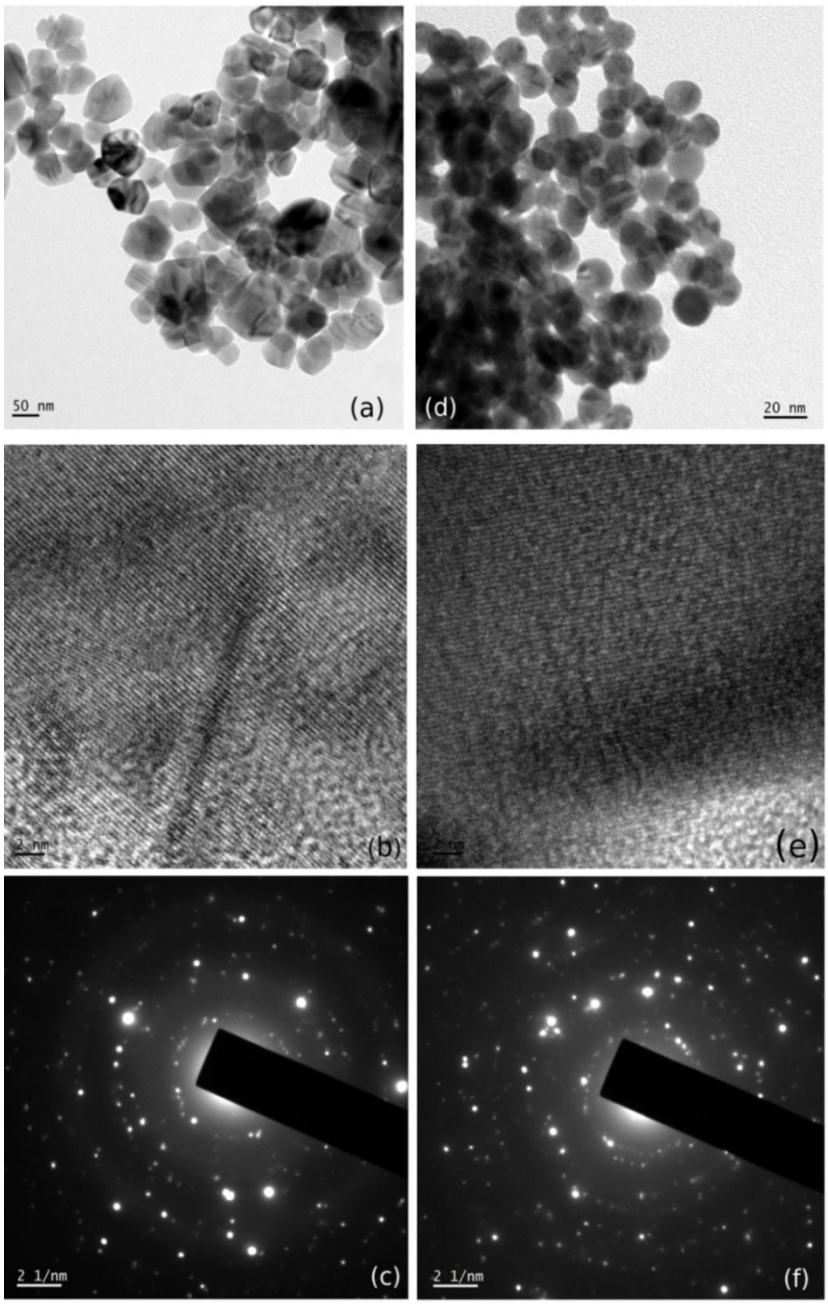

Figure. 4.4. *HRTEM images of hydrothermally (a, b) and S-H synthesised at 200 °C (d, e) 3 wt% Mn doped ZnS. The SAED patterns of hydrothermally (c) and S-H synthesised (f) 3 wt% Mn doped ZnS at a reaction temperature of 200 °C.*

4.3.3. DRS of hydrothermally and S-H synthesized Mn doped ZnS.

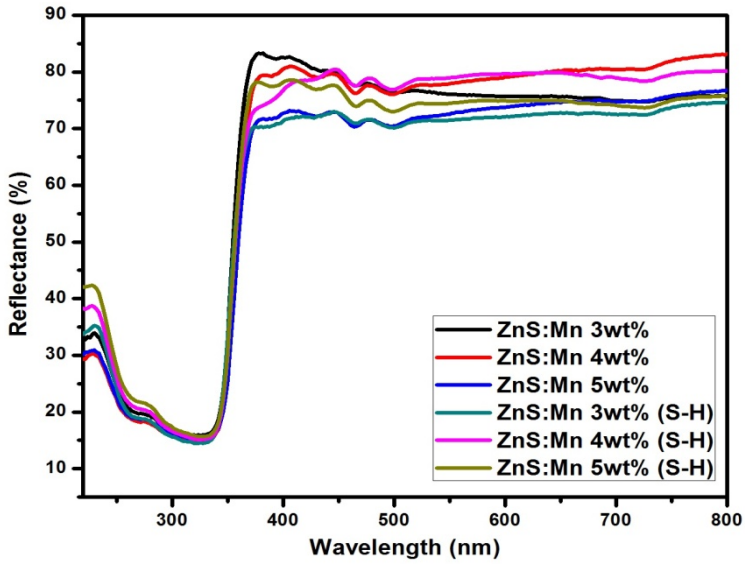

Figure. 4.5. *The room temperature UV-Vis reflectance spectra of hydrothermally and S-H synthesized Mn doped (3, 4 and 5 wt%) ZnS at a reaction temperature of 200 °C.*

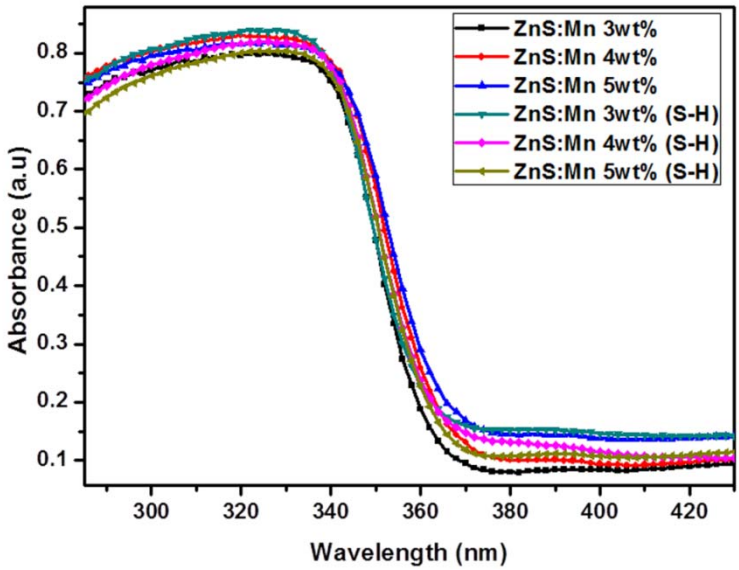

Figure.4.6. *The room temperature UV-Vis absorption spectra of hydrothermally and S-H synthesized Mn doped (3, 4 and 5 wt%) ZnS at a reaction temperature of 200 °C.*

Figure.4.6 depicts the room temperature absorption spectra of hydrothermally and S-H synthesized Mn doped (3, 4 and 5 wt%) ZnS at a reaction temperature of 200 °C and the observed absorption edge is given in Table 4.2.

Table.4.2. *Absorption edge, band gap of the hydrothermally and S-H synthesized Mn doped ZnS with different doping concentrations (3, 4 and 5 wt%).*

Samples	Absorption edge wavelength region (nm)	Band gap (eV)
ZnS:Mn (3 wt%)	(330-370)	3.53
ZnS:Mn (4 wt%)	(330-370)	3.52
ZnS:Mn (5 wt%)	(325-375)	3.50
ZnS:Mn (3 wt% S-H)	(330-365)	3.54
ZnS:Mn (4 wt% S-H)	(330-370)	3.53
ZnS:Mn (5 wt% S-H)	(330-370)	3.525

Figure.4.7. shows the $[(k/s)h\nu]^2$ versus hν plot by using Kubelka-Munk function of the hydrothermally and S-H synthesized Mn doped (3, 4 and 5 wt%) ZnS [Hoa T T Q *et al;* 2011]. It is found that the band gap of hydrothermally and S-H grown ZnS:Mn (3, 4 and 5 wt%) are blue shifted from the bulk ZnS (340 nm - 3.65eV) [Donne A L *et al;* 2013] and its values are slightly decreased with increase in doping concentration (Table. 4.2).

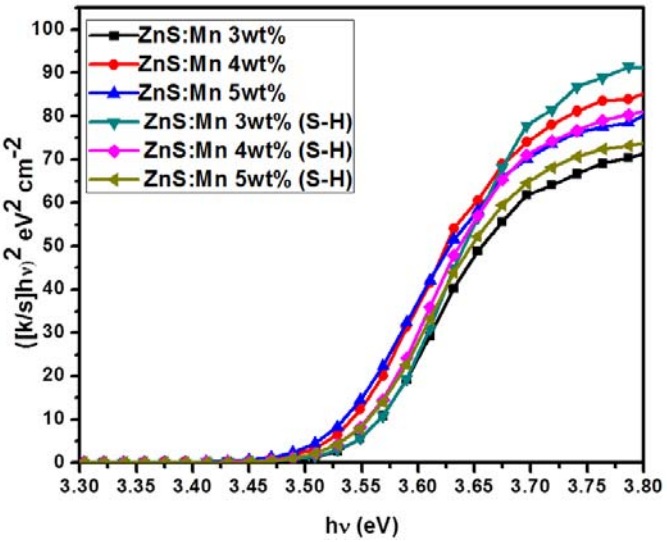

Figure.4.7. *Tauc plot of hydrothermally and S-H synthesized Mn doped (3, 4 and 5 wt%) ZnS at a reaction temperature of 200 °C.*

4.3.4. Photoluminescence analysis of hydrothermally and S-H synthesized Mn doped ZnS.

Room temperature PL spectrum of S-H and hydrothermally synthesized Mn doped (3, 4 and 5 wt%) ZnS samples are shown in figure.4.8. The PL emission spectra of the solvo-hydrothermally grown ZnS:Mn shows higher luminescence intensity as compared to that of grown by hydrothermal method. The hydrothermally grown Mn:ZnS samples show an emission band at 600 nm similar to previously reported one [Kole A K *et al;* 2013a]. The S-H grown ZnS samples with Mn 3 and 4 wt% doping shows emission at 602 nm while 5 wt% ZnS:Mn gives band at 600 nm. Apart from this the 3 wt% S-H grown Mn doped ZnS shows a strong UV band at 367 nm. Similarly 5 wt% S-H grown Mn doped ZnS have a UV emission at 376 nm. But the UV emission is absent in the case of 4 wt% S-H grown Mn doped ZnS. The near-band edge (NBE) emission in the UV region can be attributed to the band-to -band or excitonic

transition [Park S *et al;* 2012]. The emission at 600 nm may be arising from the $_4T_1$- $_6A_1$ transition of Mn^{2+} ions [Murugadoss G *et al;* 2013]. The defect related emission (trap state blue emission) usually seen in ZnS is absent in the samples under investigation. The solubility of sulphur, manganese, and zinc in organic solvents like acetonitrile is a major factor which determines the luminescence property of the materials like ZnS [Ramsden J J *et al;* 1985]. In the present case, the solubility of sulphur in acetonitrile is more as compared to that of zinc, which contributed to the formation of sulphur vacancies (Vs), and increase in population of sulphur vacancy state Vs. On exciting the sample with energy of 3.83 eV (325 nm), the electrons are pumped to the conduction band and these electrons may be trapped in shallow traps formed by Vs. From this level, the electrons reaches to the upper energy level of Mn^{2+} ($_4T_1$) by a non-radiative transition [Kole A K *et al;* 2013a]. As a result of this transition the population at $_4T_1$ level of Mn^{2+} increases. These carriers cannot stay for a long time at that level and radiate to lower level Mn^{2+} ($_6A_1$) with yellow-orange emission as reported previously [Kole A K *et al;* 2013a]. The enhanced intensity in Mn 3wt% doped S-H grown ZnS is attributed to the increase in population of sulphur vacancies contributed to the high solubility of sulphur in acetonitrile [Ramsden J J *et al;* 1985]. The rate of non-radiative transition from the shallow traps (formed by sulphur vacancy) to the $_4T_1$ level of Mn^{2+} and recombination of electrons from shallow traps with the holes in the ground states are almost equal leading to the dual wavelength emission at UV and orange-yellow region with the same intensity [Kole A K *et al;* 2013a]. The observed PL intensity reduction for the higher Mn doping concentrations attributed to the quenching effect by the Mn ions pairing or coagulation [Hoa T T Q *et al;* 2011]. Moreover the presences of organic solvents in the growth medium causes surface passivation and which may also leads to photoluminescence intensity

enhancement [Song K C *et al;* 2006]. The energy band structure showing the emission levels of ZnS:Mn is shown in figure 4.9. The CIE chromaticity coordinates (Table 4.3), of the observed yellow-orange emission from the samples are calculated which fall in the yellow-orange region (Figure 4.10).

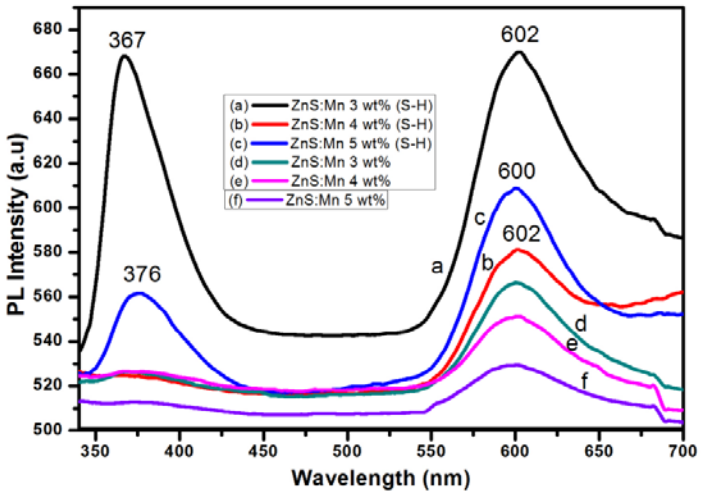

Figure. 4.8. *Room temperature PL spectra of hydrothermally (d, e and f) and S-H synthesized (a, b and c) Mn doped (3, 4 and 5 wt%) ZnS at a reaction temperature of 200 °C.*

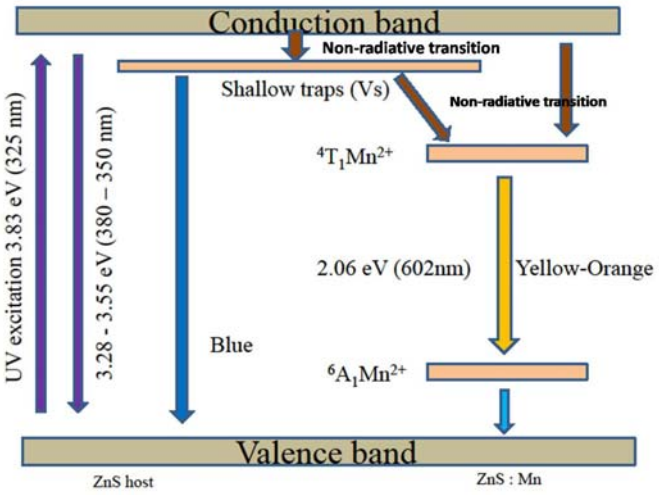

Figure. 4.9. *Schematic energy band diagram of the emission levels of Mn doped ZnS [Kole A K et al; 2013a].*

Table. 4.3. *CIE color coordinates of the hydrothermally and S-H synthesized Mn doped ZnS with different doping concentrations (3, 4 and 5 wt%).*

Samples	CIE Coordinate
ZnS:Mn (3 wt%)	(0.466,0.511)
ZnS:Mn (4 wt%)	(0.464,0.513)
ZnS:Mn (5 wt%)	(0.464,0.513)
ZnS:Mn (3 wt% S-H)	(0.475,0.504)
ZnS:Mn (4 wt% S-H)	(0.469,0.509)
ZnS:Mn (5 wt% S-H)	(0.470,0.508)

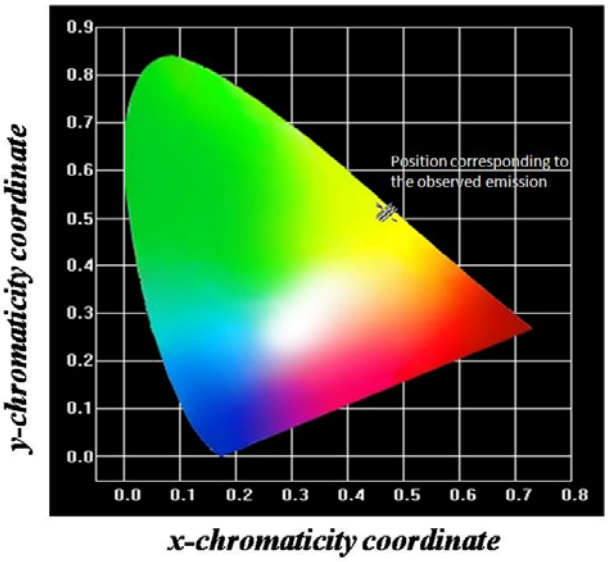

Figure.4.10. *CIE chromaticity diagram showing the colour coordinates of the hydrothermally and S-H synthesized Mn doped ZnS with different doping concentrations (3, 4 and 5 wt%).*

The specific area of grain boundary (s_{GB}) of a material has significant role in its physical and optical properties [Straumal B B *et al;* 2013]. The s_{GB} of S-H ZnS:Mn samples was calculated from the SEM images using the formula for the flattened grains.

$$\mathbf{s_{GB} = 1.65\ a/D},$$

where, '**a**' is the ratio of grain width to grain height and '**D**' is the mean grain width [Straumal B B *et al;* 2013]. It shows values of 9.598 $\times 10^6 m^2/m^3$ (3 wt%), 7.578$\times 10^6 m^2/m^3$ (4 wt%), and 7.99$\times 10^6 m^2/m^3$ (5 wt%) for S-H synthesized ZnS:Mn samples. It is difficult to calculate the s_{GB} values of hydrothermally grown ZnS:Mn samples because of the agglomeration of grains. The increase in s_{GB} value indicates the presence of more grain boundary specific area and the grain boundary angle [Zande A M *et al;* 2013]. There will be the possibility to have large amount of defect states in the grain boundary region, which become charged after trapping free carriers from neighboring grains [Ghosh D *et al;* 2014]. So the increase in specific area of grain boundary of a material will leads to the increase in population of carriers [Ghosh D *et al;* 2014], and these carriers will participate in transition between different energy levels and will boost the intensity enhancement in the PL spectrum. The enhanced luminescence efficiency observed in the Mn 3 wt% ZnS:Mn is contributed to the increase in specific area of grain boundary (9.598 $\times 10^6 m^2/m^3$) as compared to 4 wt% (7.578$\times 10^6 m^2/m^3$), and 5 wt% (7.99$\times 10^6 m^2/m^3$) of ZnS:Mn. In case of 4 wt% ZnS:Mn, UV emission is decreased because of the reduction in population of Vs contributed to decrease in S_{GB}. Further there is a possibility to have more Mn ions in S-H grown systems which contribute to increase in S_{GB} and in turn increase the luminescence intensity [Ghosh D *et al;* 2014]. The organic solvents used for the synthesis of nanocrystal materials contribute to the formation of ion-pair which in turn enhance the PL intensity of the as synthesized samples [Katano H *et al;* 2011 and Xia B *et al;* 2012].

4.4. Conclusions

The PL emission of the ZnS doped with 3 and 5 wt% of Mn, synthesized by S-H method are having intense dual wavelength emission at UV and yellow-orange region. ZnS with Mn 3 wt% exhibit higher luminescence yield at 367 nm and at yellow-orange region. The increase in luminescence yield of S-H grown sample with Mn 3 wt% doping is attributed to the increase in population of sulphur vacancies formed due to the higher solubility of the sulphur in acetonitrile and the increase in specific area of grain boundary as grown crystals. Water-acetonitrile combination is a suitable solvent for the production of better luminescent Mn doped ZnS. The chromaticity coordinates (CIE) of the observed yellow-orange emission from the samples are calculated, which fall in the yellow-orange region. The high luminescence yield at 367 nm and in the yellow-orange region from the sample is useful to fabricate white light sources based on this material and also for bio-imaging.

5 Effect of Surfactants on Morphology of Solvo-hydrothermally grown ZnS and its Optical Properties

Chapter

5.1. Introduction

Recently researchers are focused on the structural manipulation of the nanomaterials because of its optical and physical properties strongly depend on the size and morphology [Kumar S *et al;* 2005]. Several methods are being used for the morphological modification of materials, which includes thermal evaporation [Pan A *et al;* 2005], chemical method [Xu D *et al;* 2005], laser ablation [Ye C *et al;* 2002], hydrothermal, solvothermal [Phuruangrat A *et al;* 2009, Liu X *et al;* 2005 and Zhuang Z *et al;* 2010], and with various capping agents etc. Apart from these methods, materials with different structures are being grown with organic surfactants stabilization method [Kumar S *et al;* 2005 and Mehta S K, *et al;* 2010b]. The morphology and physical properties of the materials have direct relation with surfactant or capping agents used for the synthesis and are not explored well. It is reported that the head group and hydrophobic chain length of surfactants will contribute to the size and the optical emission properties of as synthesized materials [Kumar S *et al;* 2005]. The surface of the grown particles has to be protected during the synthesis process for the controlled growth of the particles. Further particle agglomeration can be avoided by surface passivation with organic stabilizers, surfactants or capping agents. Interestingly, the use of such surfactants not only protects the surface from

aggregation but also affects the chemical as well as physical properties of the material [Singh V *et al;* 2010]. Surfactants provide favorable sites for the particle growth and also control the nucleation, growth and coagulation [Li H *et al;* 2012]. Surfactants like PEG (polyethylene glycol), CTAB (cetyl trimethyl ammonium bromide), PMMA (polymethyl methacrylate), and EDA (ethylenediamine) etc, are being used to tune the morphology and enhance the physical properties of materials. Biocompatibility of the as grown material can be improved by using PEG [Fan H *et al;* 2005]. Apart from that, the use of PEG as surfactant will control the size of hollow nanospheres and monodispersibility [Dong L *et al;* 2007]. Further, size of the particle depends on the concentration of capping agent and also enhancement in PL intensity of PEG [Cholan S *et al;* 2014]. The particle aggregates can also be controlled by the use of surfactant like PMMA [Murugadoss G; 2013 and Li Y *et al;* 2014]. The addition of CTAB in the growth medium favours the formation of wurtzite phase of ZnS rather than cubic phase [Singh V *et al;* 2010]. It is reported that surfactant modified materials will have high luminescence quantum yield, because it removes the localized surface-trap states [Singh V *et al;* 2010]. The surfactant tunable hierarchical nanostructures and their effect on growth using PVP and CTAB were reported in literature [Bhirud A *et al;* 2011]. The effect of surfactants like CTAB [Chakraborty M *et al;* 2012, Nagaraju G *et al;* 2012 and Bhirud A *et al;* 2011], and EDA [Mandal A *et al;* 2011, Kole A K *et al;* 2013b and Acharya S A *et al;* 2013] on ZnS are also reported.

ZnS nanostructures with morphologies like needles, rods, sheets, micro- and nanospheres, belts etc are synthesized with chemical method by using surfactants or templates [Sookhakian M *et al;* 2013]. Recently semiconductor microspheres attained much more attention because of its potential applications

in the fields of drug targeting, bio-separation, diagnostic analysis and light emitting devices [Yu X *et al;* 2009]. The synthesis of ZnS hollow microspheres [Zhong S L *et al;* 2011, Zhang Y *et al;* 2011 and Muruganandham M *et al;* 2010], monodispersive wurtzite-type ZnS microspheres [Wu Q *et al;* 2006], mesoporous ZnS with tunable pore size and surface area [Muruganandham M *et al;* 2010a], hierarchical mesoporous ZnS–RGO (reduced grapheme oxide) composite [Sookhakian M *et al;* 2013] and 2D self-assembly of ZnS microsphere arrays via the vertical deposition technique [Wu Q *et al;* 2006] are reported. The growth of ZnS hollow spheres [Zhang Y *et al;* 2011] and wurtzite ZnS hierarchical microsphere nanostructures by hydrothermal method [Zhao J G *et al;* 2012] etc are also reported. Phosphors with less toxicity and having high luminescent quantum yield are technologically important one to use in electroluminescent devices, light emitting devices [Jian D *et al;* 2007], displays, electronics and biological applications etc [Jayasimhadri M *et al;* 2010]. White light emitting phosphors based LEDs are widely used due to its advantages like long life time, energy conservation etc [Lorbeer C *et al;* 2013, Nakamura S *et al;* 1994, Piao X Q *et al;* 2006 and Dutta D P *et al;* 2011]. Further, improving the efficiency of white light sources is a challenging research problem [Dutta D P *et al;* 2011]. Nowadays, white light emission is achieved by mixing primary coloured monochromatic sources or, by using phosphors that converts light into a combination of RGB (up conversion method) or, by yellow and blue phosphors [Dutta D P *et al;* 2011, Maio J R D *et al;* 2006, and Yang C C *et al;* 2007]. The aforesaid white light sources are unstable and exhibit week emission. In this context, a single phosphor emitting white light is an important one in order to get better luminescent quantum yield. Organic material like oxadiazole–carbazole copolymer (POC) and semiconductor quantum dot InP/ZnS also exhibit white emission [Bruno A *et al;* 2013]. Apart from that,

rare earth based materials like Dy^{3+} ions doped Gd_2O_3 nanophosphors [Jayasimhadri M *et al;* 2010], ceria nanophosphors [Dutta D P *et al;* 2011], $BaYF_5:Ln^{3+}$ (Ln= Yb,Er, Tm) nanocrystals [Zhang C *et al;* 2011] etc also exhibit white emission. White light emission from bio-friendly and relatively cost effective material like ZnS is promising one for future technology requirements and are least reported in the literature. Lu *et al*, reported white emission from Mn^{2+} doped ZnS by a surface chelating of 8 hydroxyquinoline-5-sulfonic acid with the CIE colour coordinates (0.35, 0.34) [Lu X *et al;* 2010], terbium-based infinite coordination polymer hollow microspheres are also good white emitting sources [Zhong S L *et al;* 2011], and Wang obtained white emission by combining the green, blue emission from ZnS with the red emission from porous silicon [Wang C *et al;* 2014].

The present chapter discusses the effect of surfactants like CTAB, PMMA, PEG and EDA on the synthesis, structural and optical properties of ZnS particles grown by solvo-hydrothermal method. Among these, EDA assisted solvo-hydrothermally synthesized ZnS microspheres were studied in detail because of its notable morphology as well as optical properties.

5.2. Experimental Section

5.2.1. Synthesis

ZnS samples were synthesized by using AR grade zinc acetate and thiourea along with water-acetonitrile-ethylenediamine (EDA) or Cetyl trimethylammonium bromide (CTAB) or polyethylene glycol (PEG) or polymethyl methacrylate (PMMA) solution combination as solvent (S-H method). 0.4 M zinc acetate and 0.8 M thiourea were dissolved in 40 ml solvent (18 ml water + 18 ml acetonitrile + 4 ml EDA) each separately and stirred for 5 min using magnetic stirrer. For powder surfactants like CTAB,

PMMA and PEG 0.4 M zinc acetate, 0.8 M thiourea and 0.35118 gm surfactants were dissolved in 40 ml solvent (20 ml water + 20 ml acetonitrile). Then the two solutions were mixed together suddenly and stirred again for 5 min. These solutions were transferred in to a teflon beaker, kept in an autoclave made of stainless steel and sealed. The above chemical reaction system was heated at 180 ^{0}C for a reaction time of 12 hr. After the heating process, the reaction system was allowed to natural cooling. The precipitates were filtered out and washed with water and ethanol. The resulting powder was warmed at 60 ^{0}C for 1 hr in air atmosphere.

5.2.2. Characterization

As synthesized samples were characterized using a Rigaku D/Max-C X-ray diffractometer using CuKα radiation (λ =1.5418 Å) in the 2θ range 10–80^0. A Horiba Jobin Yvon LabRAM HR system (resolution in the order of 3 cm^{-1}) equipped with a He–Ne laser (632.8 nm) was used to record the Raman spectra of the samples. The Fourier transform infrared spectrum (FTIR) of the sample was recorded on a SHIMADZU IR Affinity-1 FTIR spectrophotometer using KBr pellet technique with a resolution of 4 cm^{-1}. A JEOL model JSM-6390LV scanning electron microscope (SEM) and a Carl Zeiss Sigma field-emission scanning electron microscope (FE-SEM) were used for the morphological analysis. The transmission electron microscopy (TEM) images of the sample were taken with a FEI TECNAI G2 F20 transmission electron microscope attached with selected area electron diffraction (SAED) system. The diffused reflectance spectrum (DRS) and absorbance of the sample was recorded using a JASCO V-570 UV-Vis-NIR spectrometer in the wavelength range 220-800 nm. The room temperature photoluminescence measurement of the sample was done with a Horiba

Jobin Yvon LabRAM HR system using a He–Cd laser with an excitation wavelength of 325 nm.

5.3. Results and Discussion

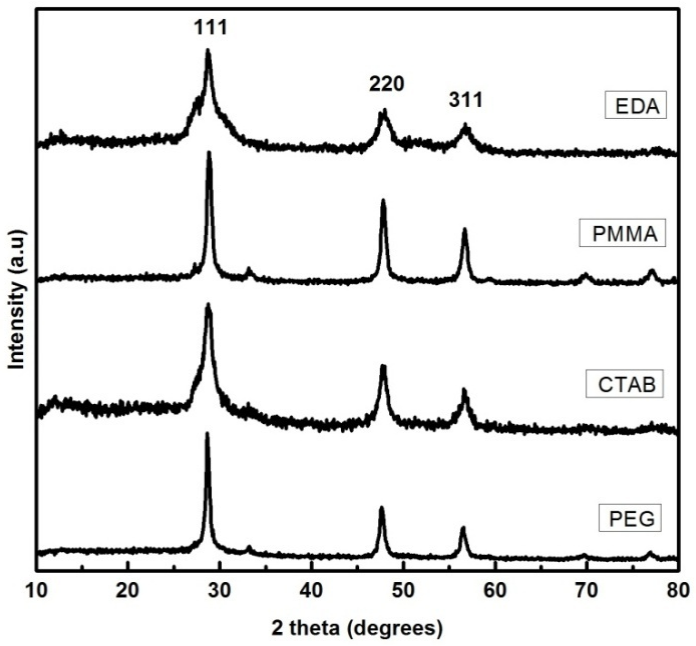

Figure. 5.1. *XRD pattern of surfactants (EDA, PMMA, CTAB, PEG) assisted solvo-hydrothermally grown ZnS synthesized at a growth temperature of 180 °C.*

Figure.5.1. depicts the XRD patterns of the surfactant assisted solvo-hydrothermally grown ZnS synthesized at a temperature of 180 °C. The X-ray diffraction pattern matches with the cubic sphalerite ZnS (JCPDS 05-0566). The calculated lattice constants are found to be matching with that of the standard value 5.406 Å [Table 5.1].

Table: 5.1. *Average crystallites size and lattice parameters of surfactants assisted S-H grown ZnS.*

Sample	Av. cryst. size (nm)	Lattice parameter (Å)
ZnS - CTAB	8	5.387
ZnS - EDA	10	5.36
ZnS - PMMA	14	5.358
ZnS - PEG	17	5.39

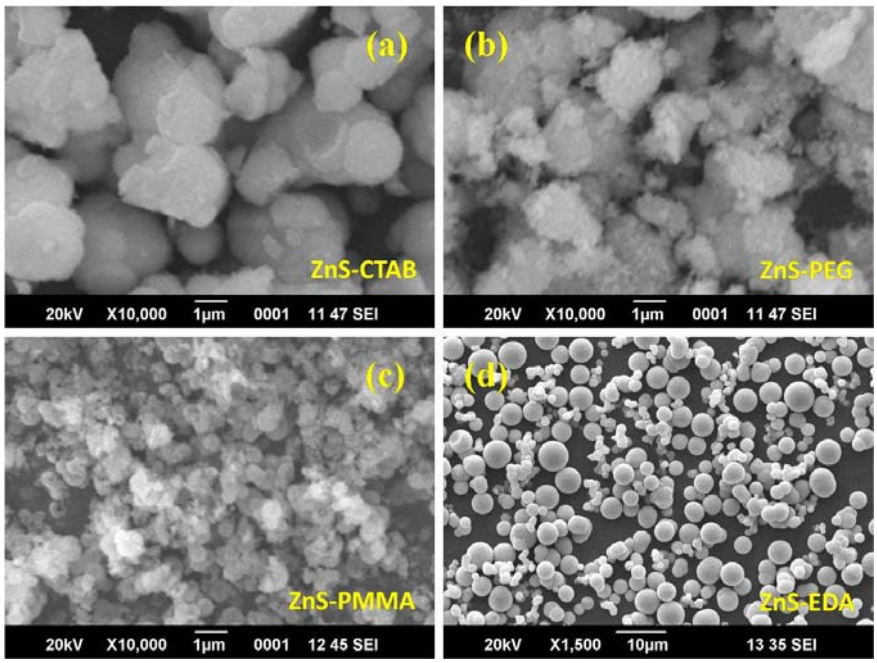

Figure.5.2. *Low resolution SEM images of surfactant assisted solvo-hydrothermally grown ZnS synthesized at a temperature of 180 °C with (a) CTAB, (b)PEG, (c) PMMA and(d) EDA.*

Figure 5.2 shows the low resolution SEM images of surfactant assisted solvo-hydrothermally grown ZnS synthesized at a temperature of 180 °C. ZnS samples grown with CTAB show plate like structure whereas almost agglomerated nano and microstructures are formed with PEG. Spherical agglomerated samples are formed when PMMA is used as surfactant. The

detailed investigations on the morphology of surfactants assisted solvo-hydrothermally grown ZnS were analyzed with high resolution FESEM. Figure 5.3 shows the high resolution FE-SEM images (with different magnifications) of CTAB assisted solvo-hydrothermally grown ZnS synthesized at a temperature of 180 °C. With the use of CTAB, nanoflakes of ZnS having length of 100-150 nm and width of 20-30 nm are formed. These nanoflakes are bundled together as observed from the figure 5.3.

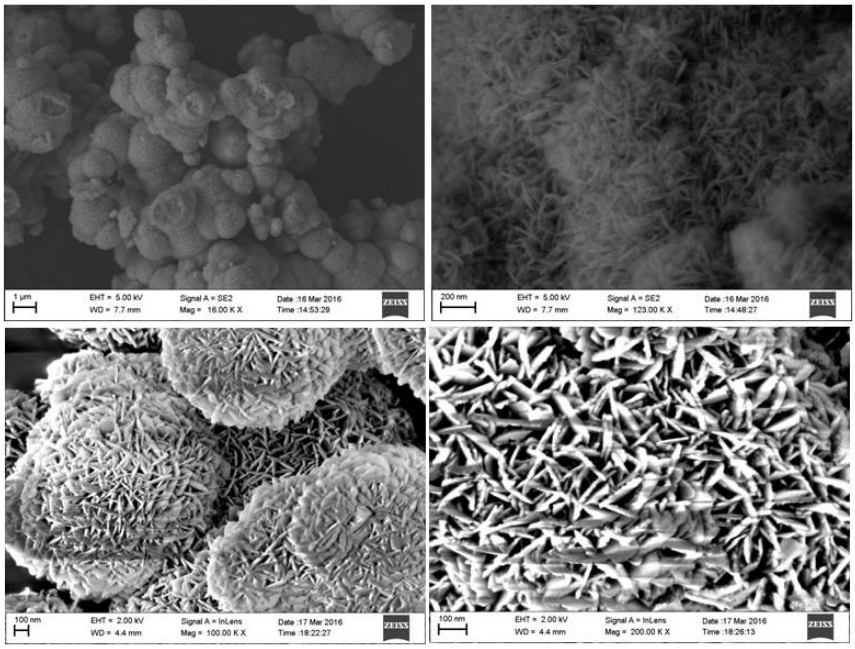

Figure.5.3. *High resolution FE-SEM images of CTAB assisted solvo-hydrothermally grown ZnS synthesized at a temperature of 180 °C.*

The FE-SEM images show that, these nanoflakes bundles are formed as a result of Ostwald ripening process [Mondal C *et al*; 2014]. In this case nanoparticles are initially formed, which come in contact with each other as a result of longer reaction time. These particles agglomerate and forms different structures like nanoflakes [Mondal C *et al*; 2014]. The effect of cationic

surfactant like CTAB, the sulphur ions will accumulate on the surface of CTAB and results in nanoclustures of ZnS [Ibupoto Z H *et al*; 2013].

While using the PEG, figure 5.4 shows that particles having size in the range 100-200 nm are formed. These particles are agglomerated and bundled together.

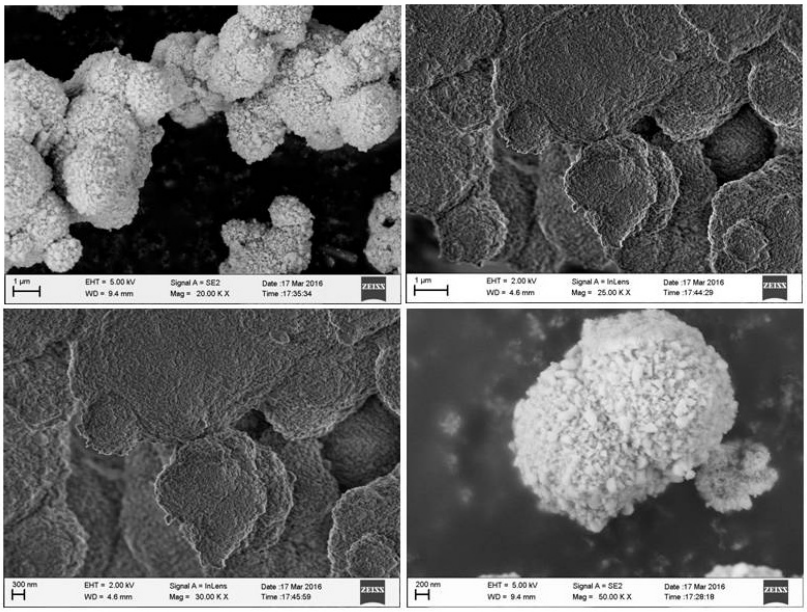

Figure.5.4. *High resolution FE-SEM images of PEG assisted solvo-hydrothermally grown ZnS synthesized at a temperature of 180 °C.*

Figure 5.5 shows the low resolution SEM images(a) & (b) and the high resolution FE-SEM images (c) & (d) of PMMA assisted solvo-hydrothermally grown ZnS synthesized at a temperature of 180 °C. The low resolution SEM images shows that the particles are agglomerated (5.5a &5.5b). Whereas, the high resolution FE-SEM images of PMMA assisted solvo-hydrothermally grown ZnS shows that these agglomerated particles are formed with the nanopartilces of size below 100 nm.

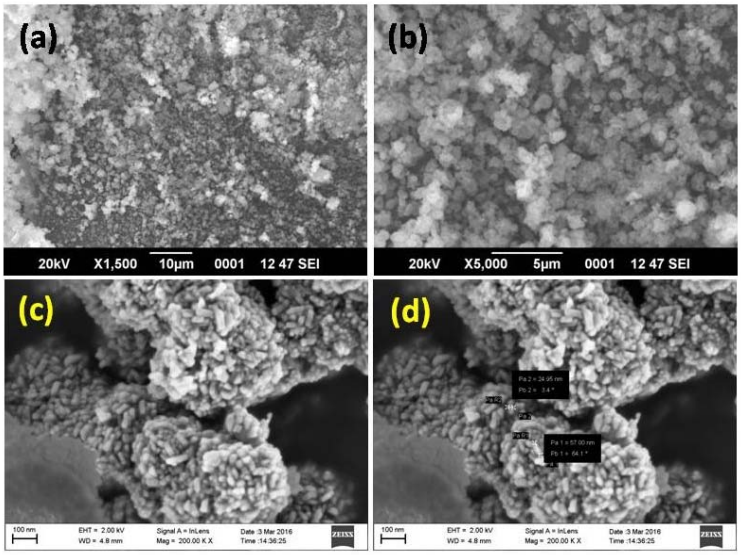

Figure.5.5. *Low resolution SEM images(a) & (b) and the high resolution FE-SEM images (c) & (d) of PMMA assisted solvo-hydrothermally grown ZnS synthesized at a temperature of 180 °C.*

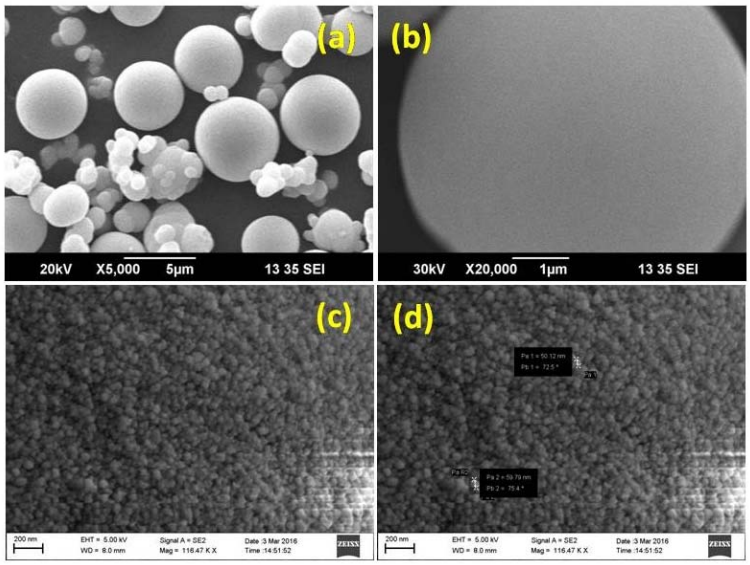

Figure.5.6. *Low resolution SEM images(a) & (b) and the high resolution FE-SEM images (c) & (d) of EDA assisted solvo-hydrothermally grown ZnS synthesized at a temperature of 180 °C.*

Interestingly, microspheres of ZnS are formed when the crystals are grown with EDA in solvo-hydrothermal method (Figure 5.6. a&b). EDA assisted solvo-hydrothermally synthesized ZnS microspheres are studied in detail because of its good morphological features and optical properties.

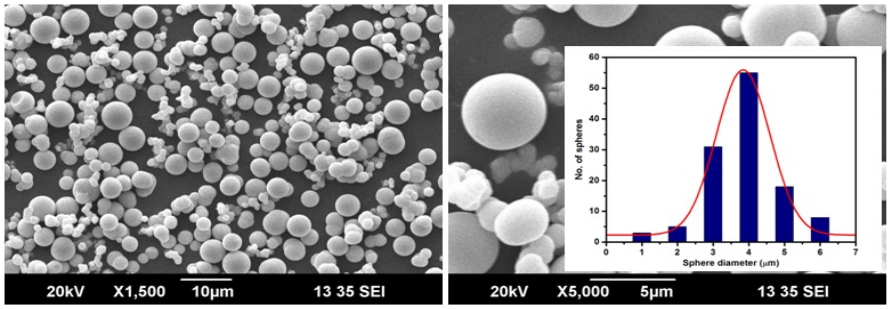

Figure.5.7. *SEM images of ethylenediamine assisted solvo-hydrothermally grown ZnS microspheres synthesized at a temperature of 180 °C.*

Figure.5.7 shows the low resolution SEM images of the solvo-hydrothermally grown ZnS microsphere synthesized at a temperature of 180 °C. The microsphere diameter distribution histogram based on SEM images (inset of Figure.5.7) shows that the size distribution is not uniform, which vary from 1- 6 µm. These microspheres are having an average diameter of 3.85 µm. Our XRD data giving broad diffraction peaks and its corresponding crystallite size calculated using Scherrer formulae, gives a value of about 10 nm. This result indicates that these microspheres are made of nano regime particles and is similar to that of solvo-hydrothermally grown ZnS reported in chapter 4. The high resolution FE-SEM images (Figure 5.6 c&d) reveal that the microspheres are made from nanospheres having size below 60 nm.

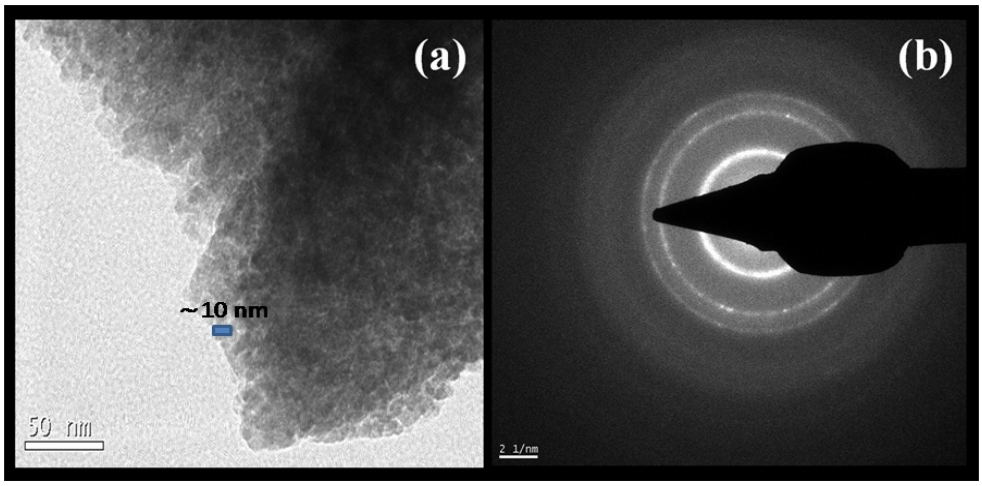

Figure.5.8. *HRTEM (a) image and the SAED pattern (b) of ethylenediamine assisted solvo-hydrothermally grown ZnS microspheres synthesized at a temperature of 180 °C.*

The HRTEM image (Figure 5.8(a)) of the present sample shows its average size is about 10 nm. The appearance of concentric rings in the SAED pattern (Figure 5.8(b)) suggest that the material is made of nano regime particles, which is in conformity with the size of the particle (about 10 nm) calculated using XRD data. So these observations clearly reveal that the microspheres with an average diameter of 3.85 μm are made of hyperfine nanoparticles having dimensions of about 10 nm.

The chemical reaction of the present experiment is complex because of the involvement of the organic solvents like acetonitrile and the growth directing surfactant ethylenediamine. The solvent acetonitrile used in the growth system react with water at higher temperature produces ammonia. Apart from this the decomposition of thiourea at higher temperature will also generate ammonia as per the reaction.

$(NH_2)_2CS \rightarrow H_2S+NH_2CN$ ---------- (1)

And at higher temperature NH_2CN react with water to form ammonia and CO_2 [Bhirud A *et al;* 2011].

$NH_2CN + 2H_2O \rightarrow 2NH_3+CO_2$ ---------- (2)

So NH_3 concentration inside the growth system likely to increase, and as a consequence pH of the system may increase. Since the growth is carried out inside a closed system, the production of volatile gases like ammonia will generate comparatively higher pressure; consequently experimental system may have higher energy. Initially nanoparticles of ZnS are formed and these nanoparticles acts as nucleation centers for the larger sized crystallites. The adjacent particles segregate to form with spherical structure in order to maintain low interfacial energy. The spherical nature of the particles is due to the surface tension at higher temperature [Bhirud A *et al;* 2011]. The shape and morphology of grains also depends on interfacial energy of the system [Bushiri M J *et al;* 2008]. Spherical shape has the minimum interfacial energy and have tendency to form spherical grains [Chen Z W *et al;* 2004]. Ethylenediamine favours the formation of spherical particles as reported by Darius *et al* [Arndt D *et al;* 2014]. The new grains try to accumulate and form some clusters in order to minimize the interfacial energy. Further, the closely lying nanograins segregate together and attain spherical morphology. This will accelerate the growth of micro crystals. From the SEM micrograph, one can see smaller spherical structures having diameters in the range 1-6 micrometers. This observation suggests that the microspheres are formed due to the clustering of smaller grains attributed to surface tension.

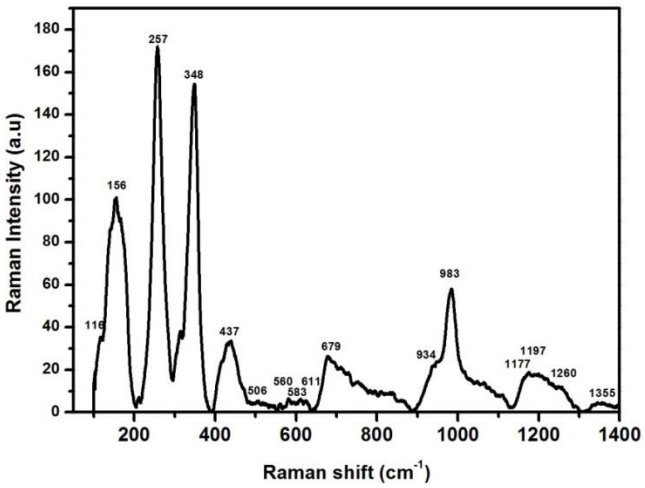

Figure.5.9. *Raman spectrum of ethylenediamine assisted solvo-hydrothermally grown ZnS microspheres synthesised at a temperature of 180 °C.*

Raman bands of cubic ZnS are reported at 266, 349, 430 and 653 cm^{-1} [Scocioreanu M *et al;* 2012]. The present sample gives Raman bands at 257, 348, 437 and 679 cm^{-1} indicates the formation of cubic phase of ZnS in agreement with our XRD results [Figure.5.9]. Raman peak observed at 156 cm^{-1} can be assigned to the disorder activated mode [Scocioreanu M *et al;* 2012]. Raman bands at 257 and 348 cm^{-1} corresponds to the TO and LO zone center phonons of (111) plane scattered cubic ZnS [Kumar S S *et al;* 2006] and also the band at 257 cm^{-1} LO phonon-plasmon coupled modes as reported by Kumar *et al* [Kumar S S *et al;* 2006]. The cubic nature of the as prepared sample is confirmed from the XRD as well as the absence of Raman peak at 286 cm^{-1} [Kumar S S *et al;* 2006]. The presence of highly intense LO phonon-plasmon coupled mode (LOPC- L^-) Raman band at 257 cm^{-1} from the present sample is attributed to the increase in carrier concentration [Kumar S S *et al;* 2006] compared with that of S-H grown ZnS given in chapter 3 and 4. The absence of organic components in the prepared ZnS microspheres is evidenced from the FTIR spectrum (Figure.5.10) and bands are seen at 451, 640 and 1220 cm^{-1} corresponds to Zn-S vibrations [Murugadoss G *et al;* 2013].

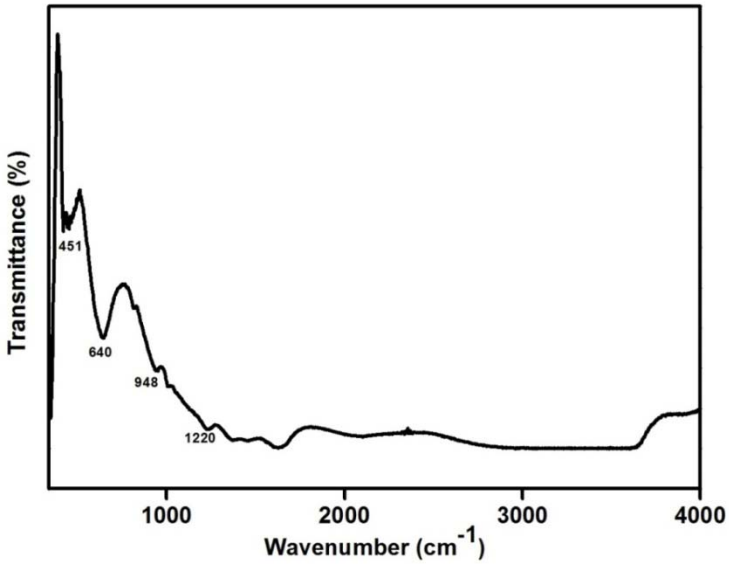

Figure.5.10. *FTIR spectrum of ethylenediamine assisted solvo-hydrothermally grown ZnS microsphere synthesized at a temperature of 180 °C.*

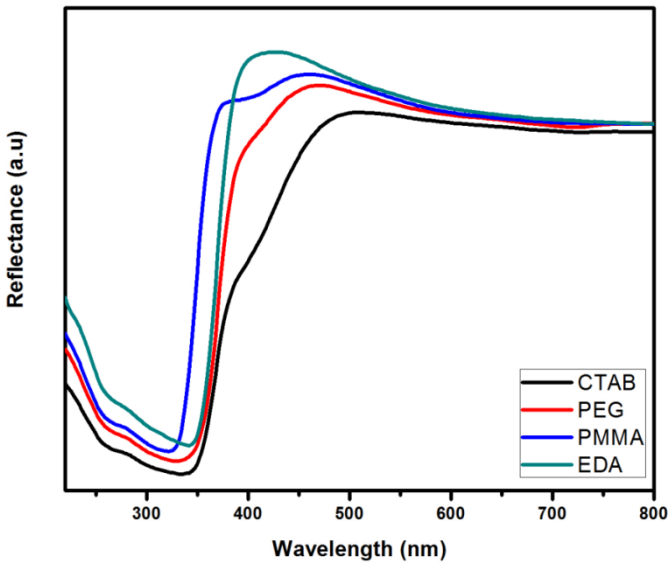

Figure.5.11. *UV-Vis reflectance spectra of surfactant (CTAB, PEG, PMMA, EDA) assisted solvo-hydrothermally grown ZnS synthesized at a temperature of 180 °C.*

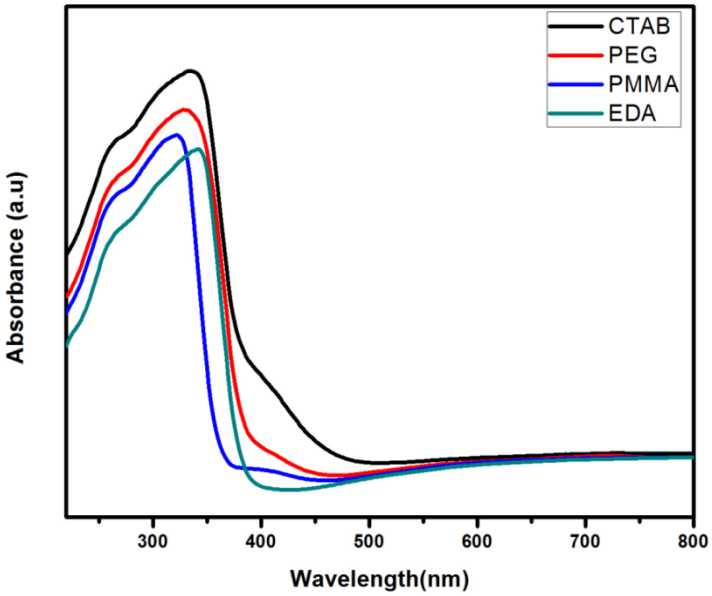

Figure.5.12. *UV-Vis absorbance spectra of surfactant (CTAB, PEG, PMMA, EDA) assisted solvo-hydrothermally grown ZnS synthesized at a temperature of 180 °C.*

The absorption edge and the band gap of the surfactant assisted solvo-hydrothermally grown ZnS are shown in Table 5.2. ZnS is a wide band gap (3.7 eV) semiconductor, which is expected to absorb only UV radiations [Hafeez M *et al;* 2013]. The UV-Visible absorbance spectra (Figure.5.12) and the reflectance spectra (Figure.5.11) recorded from the ZnS microspheres shows that the absorption edge is slightly shifted to 330-428 nm as compared to the reported one in the range 330- 380 nm [Li Y *et al;* 2008]. The maximum absorption is observed at 342 nm with a shift of the order of 2 nm with respect to bulk (340 nm) which is attributed to the microstructure nature of the sample [Peng L *et al;* 2010].

Table: 5.2. *The absorption edge and the band gap values of surfactants assisted S-H grown ZnS.*

Sample	Absorption edge (nm)	Band gap (eV)
ZnS-CTAB	334-510	3.43
ZnS-EDA	342-428	3.45
ZnS-PMMA	322-460	3.63
ZnS-PEG	328-474	3.42

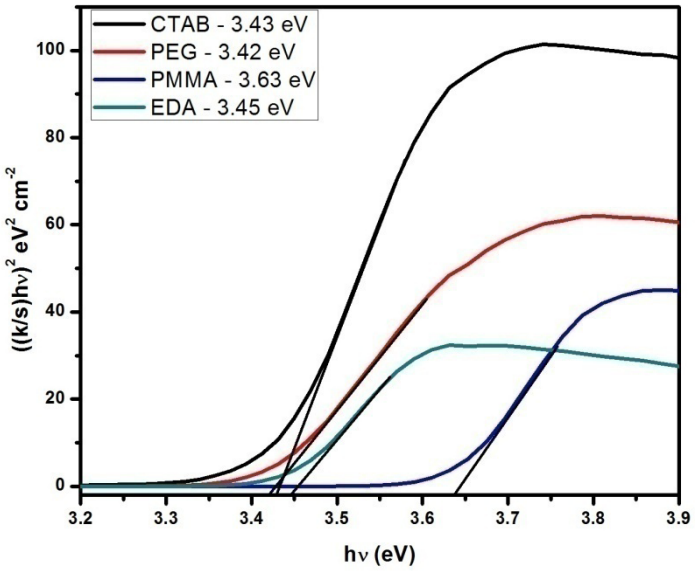

Figure.5.13. *Tauc plot of surfactant (CTAB, PEG, PMMA, EDA) assisted solvo-hydrothermally grown ZnS synthesized at a temperature of 180 °C.*

The band gap values of surfactant assisted solvo-hydrothermally grown ZnS synthesized at a temperature of 180 °C are calculated using Kubelka-Munk relation shown in figure 5.13. The band gap values are blue shifted from bulk ZnS (3.7 eV at room temperature) [Murugadoss G *et al;* 2014].

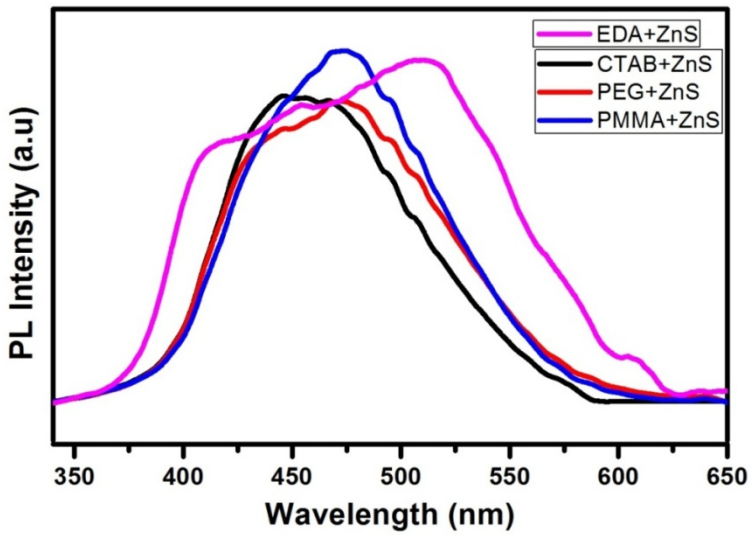

Figure.5.14. *Room temperature photoluminescence spectra of surfactant (CTAB, PEG, PMMA, EDA) assisted solvo-hydrothermally grown ZnS synthesized at a temperature of 180 °C.*

Figure 5.14 shows the room temperature photoluminescence spectra of surfactant assisted solvo-hydrothermally grown ZnS synthesized at a temperature of 180 °C. The CTAB assisted S-H grown ZnS sample shows a visible emission from 402 – 538 nm, which is centered at 456 nm, whereas PMMA and PEG assisted S-H grown ZnS sample shows a broad visible emission from 402 – 550 nm centered at 472 nm. The observed blue emission is attributed to the surface states [Wang X *et al;* 2011] or it is associated with the Zn^{2+} and S^{2-} vacancy trapped emission [Park S *et al;* 2012].

It is previously reported that hollow ZnS microspheres with rough surface feature having PL emission peaks at 3.02 (412 nm) and 2.34 eV (532 nm) [Luo Y *et al;* 2008]. But the room temperature photoluminescence spectrum of EDA assisted S-H grown ZnS sample, shows a broad emission peak in the wavelength region 380-580 nm (Figure.5.14). Hafeez *et al* reported that the visible emissions from ZnS nanostructures are due to the

intrinsic defects like Zn and S vacancies [Hafeez M *et al;* 2013]. Usually, ZnS shows a blue emission under UV excitation, which is attributed to the surface V_S or internal V_S related emission arising from the recombination between V_S donor levels and the valence band. The V_S-V_{Zn} transition in ZnS gives a greenish-yellow band in the PL spectrum [Song H Q *et al;* 2010]. The broad emission from the sample may be related to increase in carrier concentration which is evident from the appearance of intense Raman band at 257 cm^{-1}. The NBE emission from the deep levels of Zn^{2+} vacancies, S^{2-} interstitials and dislocations (390 to 400 nm) are almost absent in the room temperature PL spectrum of the ZnS microspheres. But the broad emission from EDA assisted S-H grown ZnS sample arises as a result of the blue (associated with the Zn^{2+} and S^{2-} vacancy trapped emission), green (due to the dopants or impurity atom contributed defect level emission) and the orange emission is attributed to deep levels [Park S *et al;* 2012]. However the presence of Zn and S vacancies depends strongly on the growth process [Hafeez M *et al;* 2013]. The use of the acetonitrile as a solvent for the growth, probably contributed to the increase in population of sulphur vacancies and consequently more carriers [Sajan P *et al;* 2015]. The appearance of broad visible emission from the above sample may be due to the overlapping of blue and greenish yellow emissions.

5.4. Conclusions

Morphology of ZnS grown by S-H method can be varied by using surfactants like ethylenediamine, polymethyl methacrylate, cetyl trimethylammonium bromide and polyethylene glycol during growth process. ZnS nanoflakes with length of 100-150 nm and width of 20-30 nm are obtained with the use of CTAB whereas particles having size in the

range 100-200 nm are formed while using PEG as surfactant. ZnS nanoparticles of size below 100 nm are obtained with the use of PMMA as surfactant and are agglomerated. ZnS microspheres having average diameter of 3.85 μm made of hyperfine particles with 10 nm size are obtained with solvo-hydrothermally (S-H) method using ethylenediamine surfactant, which exhibits broad visible PL emission from 380-580 nm. The broad visible PL emission from the microspheres is attributed to the increase in carrier concentration as understood from the presence of intense Raman band at 257 cm^{-1}. ZnS microspheres with broad visible emission have potential applications in the fields of bioimaging, diagnostic analysis and for the fabrication of white light sources.

Room Temperature Near-IR Photoluminescence from Ethylenediamine assisted Solvo-hydrothermally grown Wurtzite $ZnS:Nd_2O_3$ Host Guest System

6 Chapter

6.1. Introduction

Zinc sulfide (ZnS) is a wide bad gap phosphor (3.6 eV) with versatile applications due to its nontoxic nature [Reddy D A *et al;* 2012]. ZnS is a good host system for the accommodation of rare-earth (RE) atoms like Neodymium (Nd). ZnS doped with transition metal ions or/and rare-earth metal ions is a new class of materials useful for fabrication of devices like fiber amplifiers, fluorescent lamps, memory devices, lasers and LCD etc [Bouras K *et al;* 2014]. The synthesis of ZnS doped with other elements requires more care, since surface states, size effect and position of the impurities in the crystal are related to the physical and optical properties [Hu H *et al;* 2006]. The incorporation of rare earth ions in ZnS lattice is much complicated and is found to be adsorbed at the surface [Bol A A *et al;* 2002]. Since the ionic radii of rare earth (RE^{3+}) ions are higher than that of Zn^{2+}, the incorporation of RE^{3+} ions will deform the crystal lattice locally. Moreover there could be charge compensation somewhere in the host lattice. But Yan *et al* reported the possibility of RE^{3+} ion incorporation in semiconductor host lattice [Yen W M *et al*; 1999]. The abundant electronic levels of lanthanides give opportunities for the development of variety of new materials [Xu Y *et al*; 2002 and Murray G M *et al*; 1989]. Recently

extensive research is going on in the field of lanthanide doped upconversion nanoparticles especially for biological applications. The emission spectra of trivalent ions like neodymium depends on the site symmetry in the host material [Saleem S S *et al*; 1984, Schwartz R W; 1975].The near-infrared (NIR) emission from such materials have effective penetration depth of photons in tissues, which may help in minimizing the auto-fluorescence background [Tian L *et al;* 2014]. $4f^n$-$4f^n$ electronic transitions emission properties of RE incorporated ZnS synthesized at 900- 1200 °C have been reported previously [Bol A A *et al;* 2002, Zhang H *et al;* 1988 and Stapor A *et al;* 1988]. Among the lanthanides, Neodymium (Nd^{3+}) based systems has attained more investigations due to its better optical properties which have applications in optoelectronic and magnetic devices [Zhao Z *et al;* 2014]. The Nd related NIR luminescence emission from the materials have application in lasers, LEDs, optical fibers, luminescent labels and safety inks etc and are less explored [He L *et al;* 2015]. Solid state materials having emission in the NIR and MIR regions have application in lasers which can be used in bio-chemical agents, remote sensing, in IR spectroscopy etc [Brown E *et al;* 2013]. The Nd ion is more sensitive to its local environment, consequently its emission properties, because of its manifold intermediate excited energy levels [Beeby A *et al;* 2002]. Moreover neodymium doped semiconductors are showing enhanced photocatalytic properties [Zhao Z *et al;* 2014 and Baiju K V *et al;* 2007].

In the present work we are reporting the ethylenediamine assisted solvo-hydrothermal growth and photoluminescence studies of ZnS:Nd_2O_3 host-guest (ZNHG) system.

6.2. Experimental Section

6.2.1. Material Preparation

Samples of ZNHG system were synthesized by using AR grade Zinc acetate, Neodymium (III) acetate and thiourea along with water-acetonitrile-ethylenediamine (EDA) solution combination (1:1) as solvent in S-H method. Zinc acetate (0.4 M) and Neodymium (III) acetate with 3.4065gm and 0.1054gm (Nd 3 nominal wt%), 3.3713gm and 0.1405gm (Nd 4 nominal wt%) and 3.3360gm and 0.1756gm (Nd 5 nominal wt%) respectively were used for the synthesis.

Whereas the amount of thiourea used for the synthesis of all compounds described in this work were 2.4358 gm (0.8 M). Zinc acetate and neodymium acetate were taken together in a beaker and made to 40 ml solution; thiourea is also made to 40 ml solution (18 ml water + 18 ml acetonitrile + 4 ml EDA) separately. These two solutions were stirred separately for 5 min and mixed together, stirred again for 1 hr and transferred in to a teflon beaker, kept in an autoclave made of stainless steel and sealed. The above chemical reaction system was heated at 180 °C for a reaction time of 12 hr. After heating, the system was allowed to cool and the precipitates were filtered out, washed with water and ethanol. The resulting powder was warmed at 60 °C for 1 hr in air atmosphere.

6.2.1. Materials Characterization

The XRD patterns of the as synthesized ZNHG system were characterized with a Bruker D8 Advance diffractometer with CuKα radiation (λ =1.5418 Å) in the 2θ range 10–80^0. A Horiba Jobin Yvon LabRAM HR system (resolution in the order of 3 cm^{-1}) with a He–Ne laser (632.8 nm) was used as the excitation source to record the Raman spectra of

the samples. The morphology and the elemental composition of the samples were examined with a JEOL Model JSM-6390LV scanning electron microscope (SEM) and a JEOL model JED-2300 system respectively. The diffused reflectance spectra (DRS) of the samples were taken with JASCO V-570 spectrometer. PL emission studies of the samples were carried using an inVia Reflex Raman Spectrometer (Renishaw, UK, Model No. M-9836-3991-01-A) offering automated alignment via the WiRE software with an excitation wavelength of 785 nm (300 mW, CW, Model. No. HPNIR 92E371, Class 3B laser product, Renishaw plc, UK) and the exposure time was 10 s.

6.3. Results and Discussion

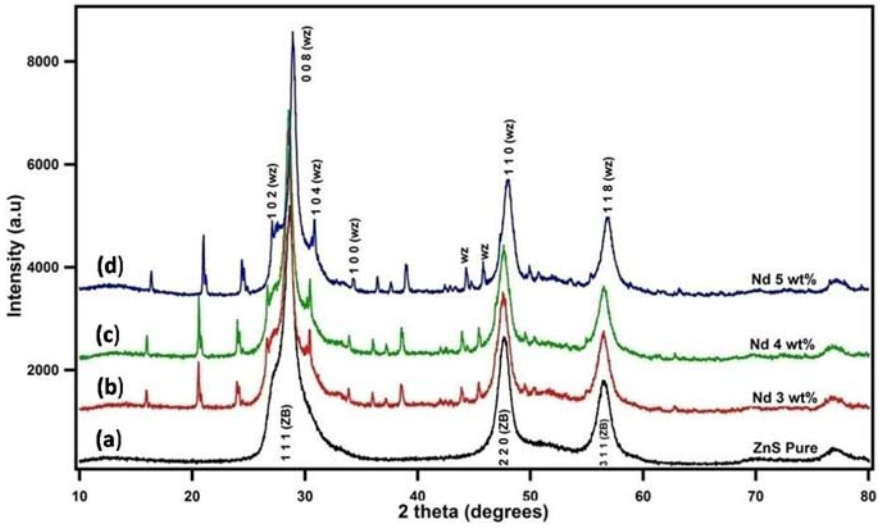

Figure. 6.1. *XRD pattern of ethylenediamine assisted solvo-hydrothermally obtained (growth temperature: 180 °C) (a) ZnS, ZnS:Nd_2O_3 host-guest (ZNHG) system grown with (b) 3 wt%, (c) 4 wt% and (d) 5 wt% Nd acetate in the precursor solution.*

The prominent peaks of S-H grown ZnS show diffraction patterns (Figure. 6.1.) contributed to cubic sphalerite phase of ZnS (JCPDS 05-0566) [Chapter 5]. Whereas it is observed that, on addition of neodymium acetate in the crystal growth system, hexagonal wurtzite phase (JCPDS 39-1363) is obtained. The phase transition of ZnS from zinc blend to wurtzite phase usually takes place at a high temperature of 1020 °C. But the growth of wurtzite phase ZnS at a temperature of 170 °C [Acharya S A *et al*; 2013], 450-500 °C [Nguyen T T *et al*; 2011], 250 °C [Kole A K *et al*; 2012] and 95 °C [Wang L *et al*; 2013] are also reported. The addition of soft template like ethylenediamine in to the growth medium leads to the formation of ZnS wurtzite phase nanorods at a low temperature of 170 °C [Acharya S A *et al*; 2013]. Interestingly, our group reported microspheres of ZnS with the addition of ethylenediamine in to the growth medium of ZnS [Chapter 5]. As stated previously Acharya *et al* reported that ethylenediamine concentration is an important parameter related to crystallinity of ZnS wurtzite structure grown by chemical reaction at a temperature of 170 °C [Acharya S A *et al*; 2013]. In the present study we obtained spherical morphology with wurtzite ZnS phase. It indicates that the addition of neodymium acetate in to the ZnS growth medium consists of ethylenediamine, zinc acetate and thiourea favoured the growth of wurtzite phase of ZnS. The formation of wurtzite phase ZnS may be the combined effect of ethylenediamine and the lattice pressure aroused with the effect of neodymium ions during the reaction and nucleation process. In addition to the wurtzite peaks, some Nd_2O_3 peaks are also observed at around 2theta values 16^0, 21^0, 24^0 and 38.5^0. These observations indicate that the XRD

patterns of ethylenediamine assisted solvo-hydrothermally grown ZNHG system comprises of wurtzite phase ZnS and Nd_2O_3, both of these are in a mixed state. It shows that the neodymium crystallizes as guest Nd_2O_3 in the host wurtzite ZnS crystal. Shift in XRD peaks towards the higher 2 theta side are observed on increasing the concentration of neodymium. The average crystallite size is 12, 10, 11 nm for ZNHG system with Nd 3, 4 and 5 nominal wt% addition to the growth medium respectively. The calculated lattice parameter values are not having much variation with respect to ZnS, which are about a=3.79 Å & c=6.20 Å for 3 wt%, a=3.82 Å & c=6.23 Å for 4 wt% and a=3.83 Å, c=6.26 Å for 5 wt% Nd concentrations respectively.

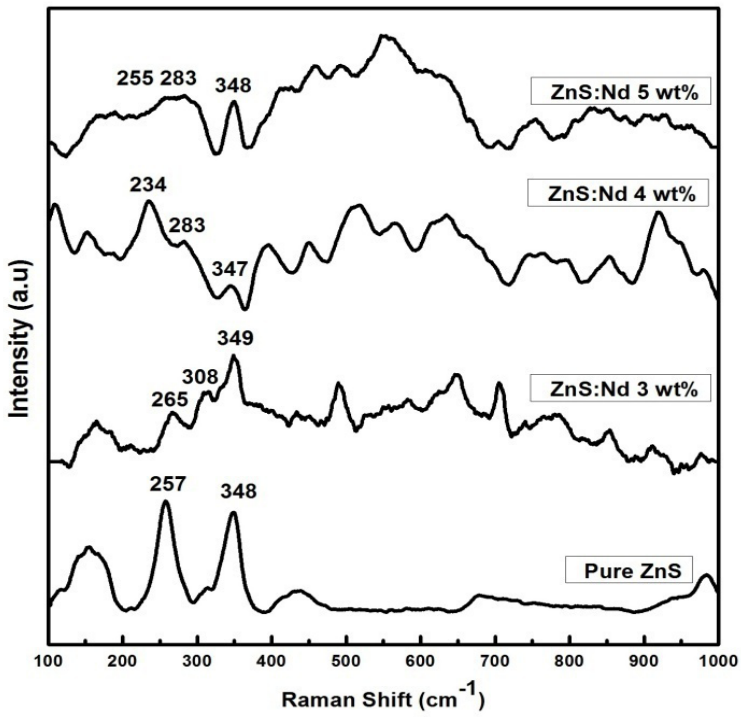

Figure. 6.2. *Room temperature Raman spectra of ethylenediamine assisted solvo-hydrothermally obtained (growth temperature: 180 °C) ZnS:Nd_2O_3 host-guest (ZNHG) system grown with 3, 4 and 5 wt% Nd acetate in the precursor solution.*

***Table 6.1**. Room temperature Raman spectra (cm^{-1}) of ethylenediamine assisted solvo-hydrothermally obtained (growth temperature: 180 °C) ZnS:Nd_2O_3 host-guest (ZNHG) system grown with 3, 4 and 5 wt% Nd acetate in the precursor solution.*

Cubic ZnS (Acharya S A *et al*; 2013 and Scocioreanu M *et al*; 2012)	Nd 3 wt% Wurtzite ZnS	Nd 4 wt% Wurtzite ZnS	Nd 5 wt% Wurtzite ZnS	Assignments (Acharya S A *et al*;2013 and Cheng Y C; 2009)
257 s (TO)	265 w	234 m	255 w	A_1 (TO)
				E_1 (TO)
	308 vw	283 vw	283 w	E_L^2
348 s (LO)	349 m	347 vw	348 m	E_1 (LO)
		393 w		A_1 (LO)
				TA+TO
434 w (TO+LA)	490 m	448 w	458 vw	LA+LO
	648 w		492 vw	TO+LO
	706 w		747 w	2 E_1(LO), 2 LO

s: strong, m: medium, w: weak, vw: very weak

Raman peaks observed in the cubic ZnS samples are given in our previous report [Chapter 5]. As observed from the XRD that, in ZnS:Nd_2O_3 host-guest system, ZnS exist in wurtzite phase. Wurtzite phase of ZnS belongs to the C_{6v} (6 mm) space group [Acharya S A *et al*; 2013] and is having $A_1+E_1+2E_2+2B_1$ optical modes. In this B_1 modes are silent modes whereas A_1 and E_1 are Raman and IR active polar modes. The presence of multiple resonances Raman peaks reveals the good optical quality of the samples [Wang X *et al;* 2011]. The TO mode is seen at 265, 234 and 255 cm^{-1} in 3, 4 and 5 wt% Nd added samples respectively [Figure 6.2]. Bands are also seen at 308, 283 and 283 cm^{-1} in 3, 4 and 5 wt% Nd added samples (Table 6.1) and the LO mode is observed at 348 cm^{-1}. In addition some more peaks are seen above 500 cm^{-1} in wurtzite phase of ZnS indicates the formation of wurtzite ZnS phase with the addition of neodymium in the growth system which is in agreement with the XRD data.

EDAX studies reveal the presence of Nd in different proportions in samples under investigation (Table 6.2). The rare-earth doping on ZnS is difficult because of difference in ionic radii of Zn and rare-earth atoms like Nd. So neodymium oxide is formed which is seen as guest system in ZnS host lattice confirmed with the presence of oxygen in all samples (Figure. 6.3, Table 6.2).

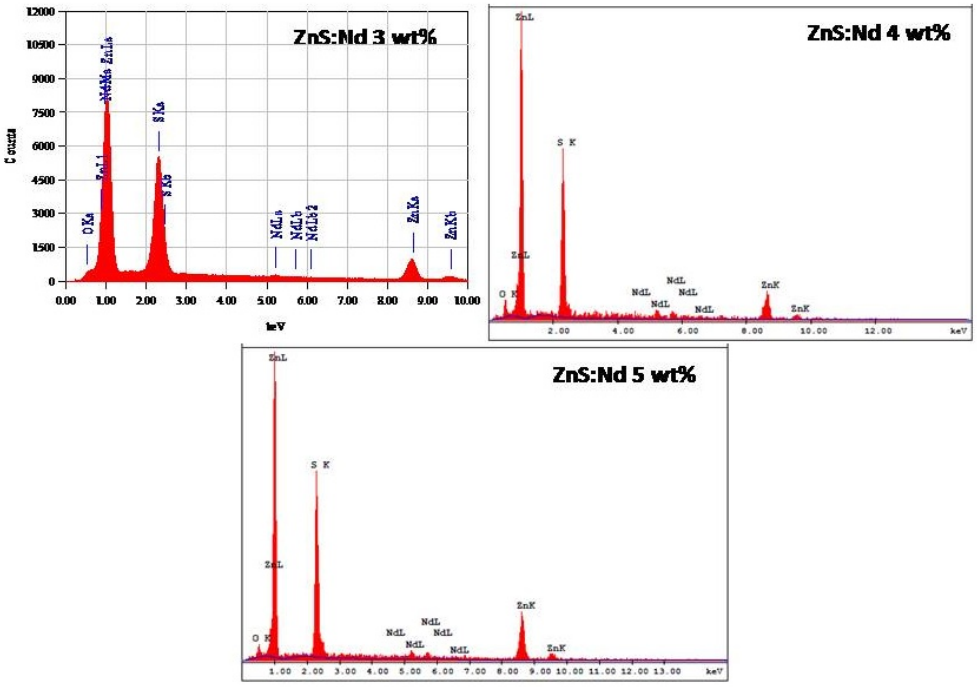

Figure.6.3. *EDAX spectra of ethylenediamine assisted solvo-hydrothermally obtained (growth temperature: 180 °C) ZnS:Nd_2O_3 host-guest (ZNHG) system grown with 3, 4 and 5 wt% Nd acetate in the precursor solution.*

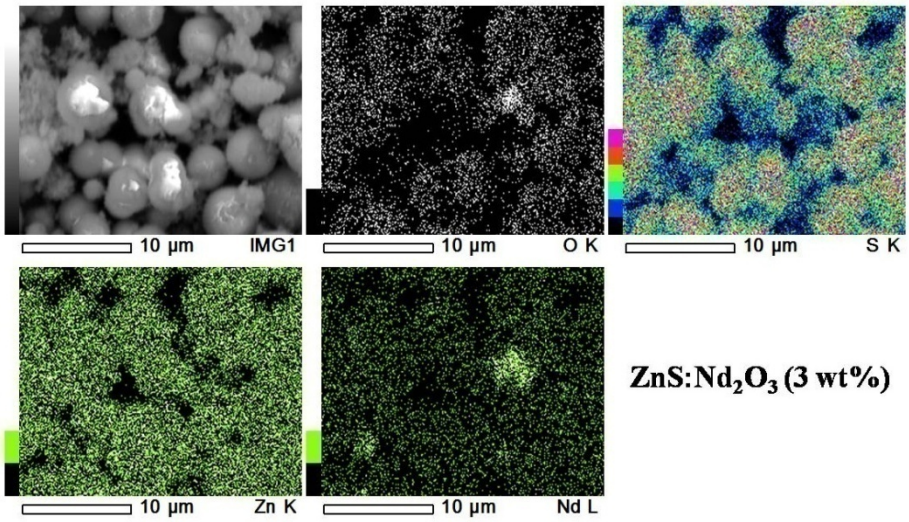

Figure.6.4. *X-ray dot mapping of ethylenediamine assisted solvo-hydrothermally obtained (growth temperature: 180 °C) ZnS:Nd_2O_3 host-guest (ZNHG) system grown with 3 wt% Nd acgetate in the precursor solution.*

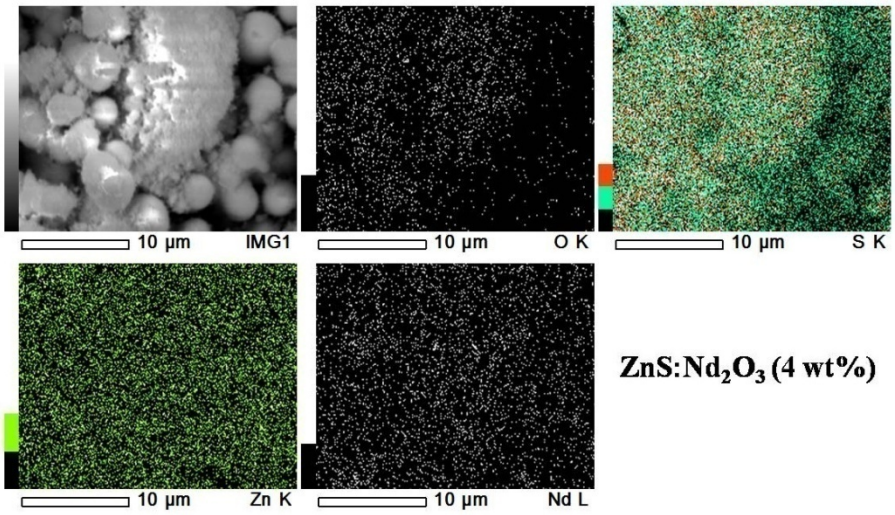

Figure.6.5. *X-ray dot mapping of ethylenediamine assisted solvo-hydrothermally obtained (growth temperature: 180 °C) ZnS:Nd_2O_3 host-guest (ZNHG) system grown with 4 wt% Nd acetate in the precursor solution.*

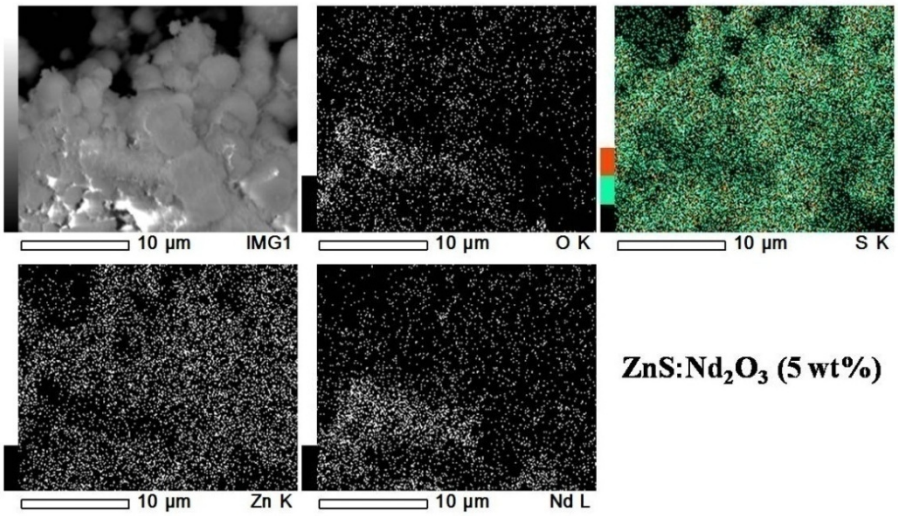

Figure.6.6. *X-ray dot mapping of ethylenediamine assisted solvo-hydrothermally obtained (growth temperature: 180 °C) ZnS:Nd_2O_3 host-guest (ZNHG) system grown with 5 wt% Nd acetate in the precursor solution.*

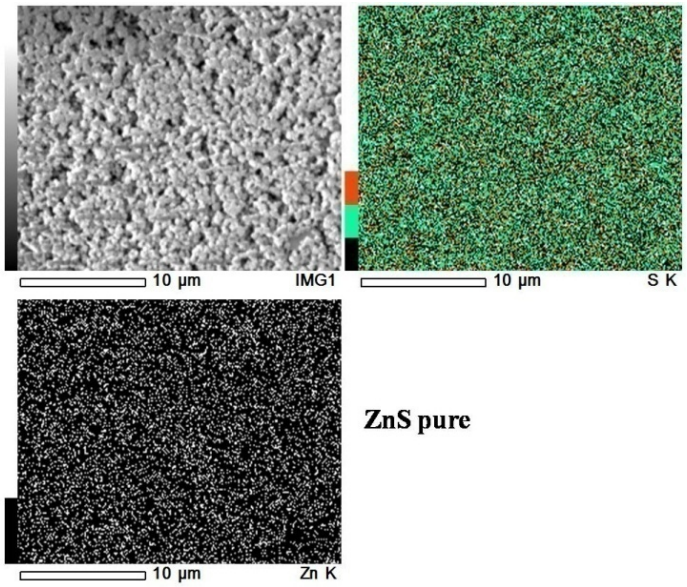

Figure.6.7. *X-ray dot mapping of ethylenediamine assisted solvo-hydrothermally obtained (growth temperature: 180 °C) ZnS.*

The X-ray dot mapping shows the presence of zinc, sulfur, neodymium and oxygen in the case of ZnS:Nd_2O_3 host-guest (ZNHG) system grown with 3wt% (Figure 6.4), 4wt% (Figure.6.5) and 5wt% (Figure. 6.6) Nd acetate in the precursor solution. Whereas the ZnS shows the presence of zinc and sulfur only (Figure.6.7)

Table 6.2. The EDAX data of ethylenediamine assisted solvo-hydrothermally obtained (growth temperature: 180 °*C*) ZnS:Nd_2O_3 host-guest (ZNHG) system grown with 3, 4 and 5 wt% Nd acetate in the precursor solution.

ZnS:Nd 3 wt%		ZnS:Nd 4 wt%		ZnS:Nd 5 wt%	
Element	**Atom %**	**Element**	**Atom %**	**Element**	**Atom %**
O	1.57	O	8.80	O	8.33
S	26.81	S	36.52	S	40.17
Zn	70.27	Nd	3.97	Nd	2.21
Nd	1.35	Zn	50.71	Zn	49.29
Total	100	Total	100	Total	100

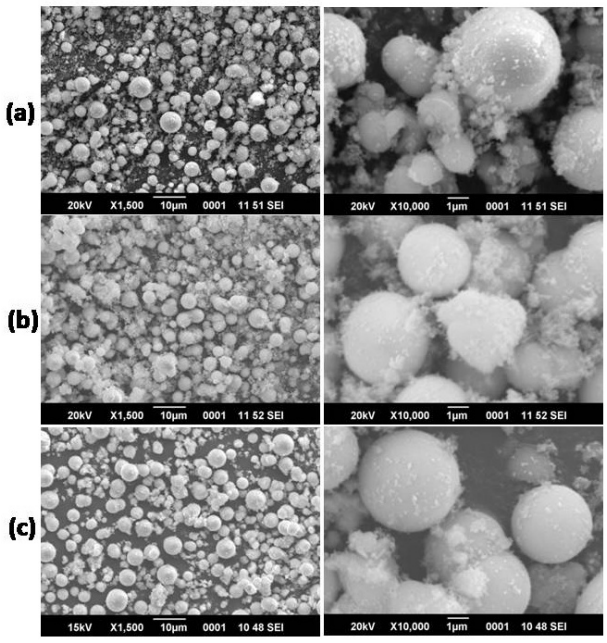

Figure.6.8. *SEM images of of ethylenediamine assisted solvo-hydrothermally obtained (growth temperature: 180 °C) ZnS:Nd_2O_3 host-guest (ZNHG) system grown with (a) 3 wt%, (b) 4 wt% and (c)5 wt% Nd acetate in the precursor solution.*

From the SEM images of the samples we can see that, all the samples are having spherical morphology with a little agglomerated structure (Figure.6.8). The spherical nature of the samples was due to the growth directing surfactant ethylenediamine and solvent acetonitrile used for the synthesis as described in Chapter 5. The addition of Nd salt in the growth medium probably favours the agglomeration of smaller spheres to a certain amount as one can see from the SEM images (Figure. 6.8).

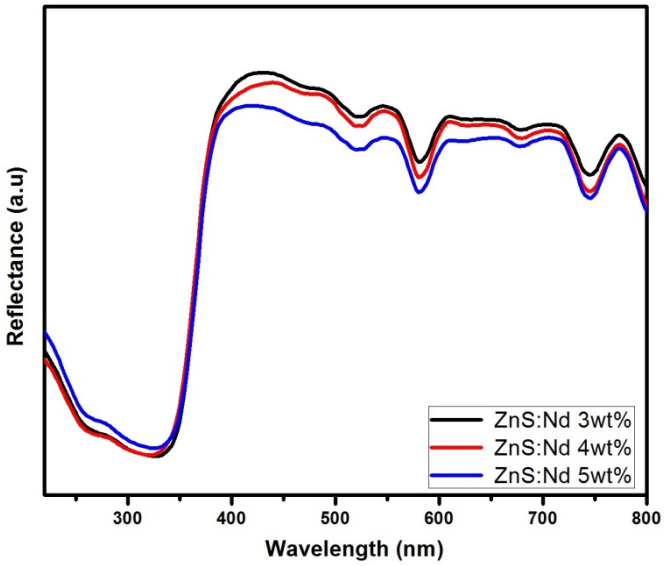

Figure.6.9. *Reflectance spectra of ethylenediamine assisted solvo-hydrothermally obtained (growth temperature: 180 °C) ZnS:Nd_2O_3 host-guest (ZNHG) system grown with 3, 4 and 5 wt% Nd acetate in the precursor solution.*

The room temperature reflectance spectra of ethylenediamine assisted solvo-hydrothermally grown Nd added (3, 4 and 5 wt%) ZnS:neodymium host-guest system at 180 °C are shown in figure 6.9. The absorption spectra of the samples (Figure. 6.10) shows absorption peaks at 521, 581, 678 and 746 nm contributed to Nd ions as reported by Bouras *et al* [Bouras K *et al;* 2014]. A shift in absorption edge towards lower energies

with increase in Nd content is observed in the present samples. Comparing with the electronic energy levels of Nd^{3+}, these observed Nd related absorption peaks corresponds to the direct excitation of electrons from the $^4I_{9/2}$ ground state to the excited states [Bouras K *et al;* 2014].

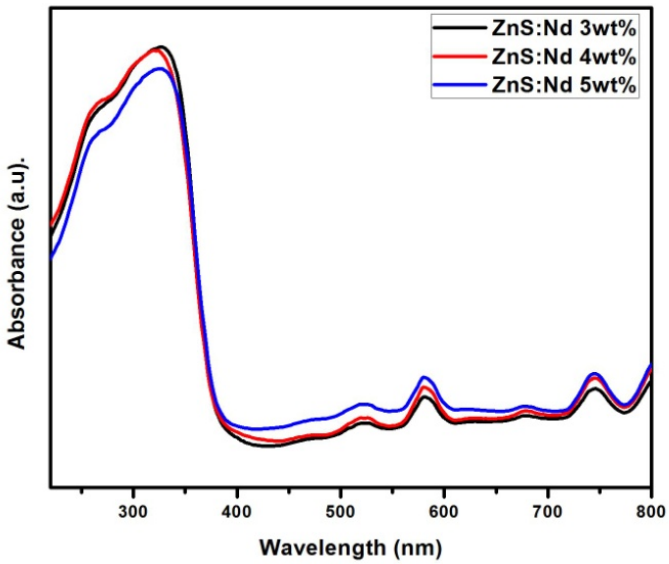

Figure.6.10. *Absorbance spectra of ethylenediamine assisted solvo-hydrothermally obtained (growth temperature: 180 °C) ZnS:Nd_2O_3 host-guest (ZNHG) system grown with 3, 4 and 5 wt% Nd acetate in the precursor solution.*

The band gaps of the present samples were calculated using Kubelka-Munk function. It is observed that there is no appreciable change in the band gap of all the samples. The obtained band gap values are 3.48 eV (Nd 3 wt%), 3.50 eV (Nd 4 wt%) and 3.47 eV (Nd 5 wt%) (Figure 6.11).

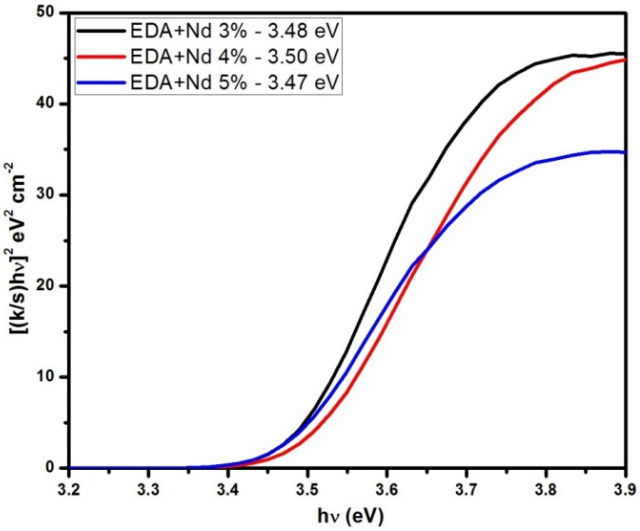

Figure.6.11. *Tauc plot of ethylenediamine assisted solvo-hydrothermally obtained (growth temperature: 180 °C) ZnS:Nd_2O_3 host-guest (ZNHG) system grown with 3, 4 and 5 wt% Nd acetate in the precursor solution.*

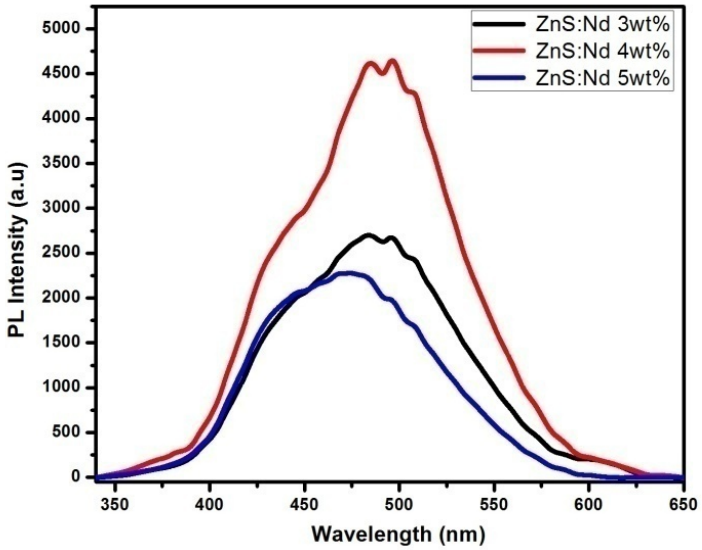

Figure.6.12. *Room temperature photoluminescence (with an excitation of 325 nm) spectra of ethylenediamine assisted solvo-hydrothermally obtained (growth temperature: 180 °C) ZnS:Nd_2O_3 host-guest (ZNHG) system grown with 3, 4 and 5 wt% Nd acetate in the precursor solution.*

Figure 6.12 shows the room temperature photoluminescence spectra of $ZnS:Nd_2O_3$ host-guest system with an excitation wavelength of 325 nm and figure 6.13 is that with excitation of 785 nm. With the 325 nm excitation, Nd 3 wt% added sample shows broad blue emission from 425-530 nm centered at 485 nm, Nd 4 wt% added sample shows emission from 415-540 nm centered at 490 nm and the Nd 5 wt% added sample have emission from 420-525 nm centered at 470 nm. But in the case of cubic ZnS, a broad emission peak is observed which is in the range 380 nm to 580 nm [Chapter 5]. The reduction in PL emission range with respect to that of cubic ZnS may probably due to the absence of impurities. The observed blue emission from ZNHG system is attributed to the surface states [Wang X *et al;* 2011] or it is associated with the Zn^{2+} and S^{2-} vacancy trapped emission [Park S *et al;* 2012] which is in consistent with previous report [Chapter 5].

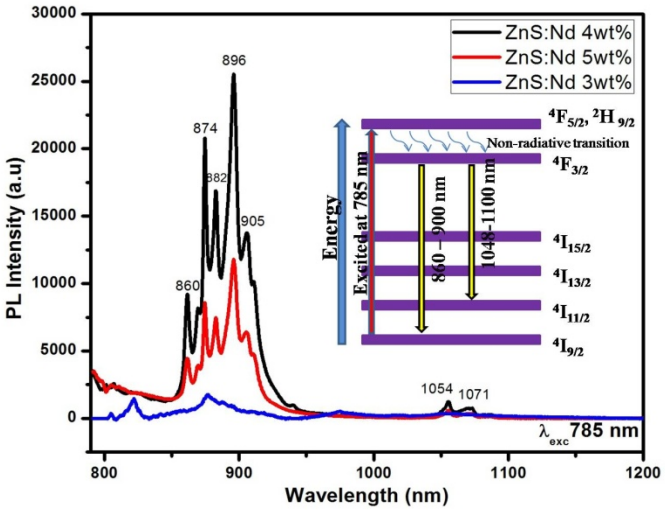

Figure.613. *Room temperature photoluminescence (with an excitation of 785 nm) spectra of ethylenediamine assisted solvo-hydrothermally obtained (growth temperature: 180 °C) $ZnS:Nd_2O_3$ host-guest (ZNHG) system grown with 3, 4 and 5 wt% Nd acetate in the precursor solution.*

The Nd 4 and 5 wt% added ZNHG samples shows intense IR emission bands at 860-905 nm and feeble emission at 1054 and 1071 nm while exciting with IR radiation of wavelength 785 nm. The intensity reduction in the Raman peaks of all the samples attributed to the fluorescence nature of the samples. The optical properties of neodymium is mainly originates from the $4f^4\ 6s^2$ electronic configuration. These observed emission at 860 -905 nm attributed to the radiative transition from $^4F_{3/2}$ to $^4I_{9/2}$ and emission at 1054 and 1071 nm is due to that of $^4F_{3/2}$ to $^4I_{11/2}$ transition of Nd electronic energy levels [Bouras K *et al;* 2014]. Whereas the Nd 3 wt% added sample shows very weak luminescence emission in the IR region, which may be due to relatively less Nd ion incorporation as we observed from the EDAX. The proposed band structure of emissions from Nd energy levels is shown in inset of figure 6.13. Generally the IR emission in the wavelength region around 885 and 1060 nm are considered as biological window which includes with the transparency windows of human tissues [Rocha U *et al;* 2013]. The IR emissions in these two regions are much favourable for sub-tissue imaging and sensing since neodymium emission bands are located at both sides of the characteristic water absorption band centered at 980 nm [Rocha U *et al;* 2013]. Reports suggest that the quasi-three-level $^4F_{3/2}$-$^4I_{9/2}$ transition from Nd ion doped laser around 900 nm have much more attention in recent years [Rusu M *et al;* 2004]. The IR emission property of these materials is useful to the fabrication of new IR laser sources.

6.4. Conclusions

In summary, the structural and optical properties of ethylenediamine assisted solvo-hydrothermally grown ZnS:Nd_2O_3 host-guest (ZNHG) system were carried out. Wurtzite phase of ZnS exists in ZNHG system

instead of cubic phase of ZnS. Narrowing of visible PL emission of ZNHG system with respect to that of cubic ZnS is contributed to the addition of neodymium acetate in the growth system, which favoured the formation of wurtzite phase of ZnS. The Nd 4 and 5 wt% added samples of ZNHG system shows Nd related emission peaks at 860 – 905 nm ($^4F_{3/2}$ to $^4I_{9/2}$ transition) and feeble emission at 1054 and 1071 nm ($^4F_{3/2}$ to $^4I_{11/2}$ transition) as well as the ZnS related blue emission. The observed Nd related emission in the IR region can be used for the fabrication of IR sources and for bio-imaging applications.

Investigations on Biocompatibility and Imaging Studies of Ethylenediamine assisted Solvo-hydrothermally grown ZnS Microspheres and Solvo-hydrothermally grown Mn Doped ZnS Nanoparticles

7 Chapter

7.1. Introduction

Medical bio-optical imaging has become an advanced research area recently, with the development of nanomaterials and inorganic nanocrystals possessing high luminescence properties for bio-sensing and bio-imaging. The spectral tunability of semiconductor materials along with the high efficiency attained importance in recent research which explored its applications for cell tracking, cancer and cell detection [Fan G *et al;* 2014, Yong K T *et al;* 2010 and Lee J Y *et al;* 2014]. Native biological fluorescence, light absorption and scattering by biological tissue constituents are strongly affecting the visible light imaging process [Luo S *et al;* 2011]. Haemoglobin and amino acids strongly absorbs wavelength below 600 nm [Maestro L M *et al;* 2012, Wang G *et al;* 2011 and Zagorovsky K *et al;* 2013]. Cadmium based quantum dots are being used for bioimaging because of its inherent high quantum yield. However, the bio-accumulation of hazardous materials like Cd is harmful to vertebrate system and internal organs [Pradhan N *et al;* 2007, Poulose A C *et al;* 2012 and Luo P G *et al;* 2013] and its bio-stability [Yong K T *et al;* 2010, Lee J Y *et al;* 2014, Luo S

et al; 2011, Ruan S *et al;* 2014 and Polavarapu L *et al;* 2011]. Unfortunately, bio-compatible, heavy metal free and high fluorescent non toxic materials which are suitable for bioimaging are less in number. Semiconductor nanomaterials surrounded by organic monolayers having enhanced optical properties with high stability are another option to escape from toxicity of Cd based chalcogenides for bio-imaging. Hsieh *et al* used highly luminescent CdSe/ZnS quantum dots (QDs) as visible imaging dye [Hsieh J M *et al;* 2006]. Yong *et al* reported the in-vivo imaging studies and tumor targeting of QD bioconjugates [Yong K T *et al;* 2010]. Ruan *et al* reported carbon based nitrogen-doped nanospheres as advanced materials in this area [Ruan S *et al;* 2014]. Nanomaterials like CdS, ZnCdS, ZnSe, ZnS and their doped combinations which give the UV-blue emissions were widely used for biological applications [Durgadas C V *et al;* 2012, Hsieh J M *et al;* 2006, Wang G *et al;* 2011 and Liab J *et al;* 2013.]. Above luminescent materials requires biocompatible surface coating, which is a major drawback [Durgadas C V *et al;* 2012]. Comparatively less toxic ZnS having high luminescent yield with good biocompatibility are suitable candidate for replacing the traditional toxic cadmium based materials. In the present chapter, we are reporting the investigations on biocompatibility and imaging studies of S-H grown ZnS microspheres and Mn doped ZnS nanoparticles.

7.2. Experimental

7.2.1. Synthesis

The synthesis of ethylenediamine assisted solvo-hydrothermally grown ZnS microspheres are described in chapter 5, whereas the solvo-hydrothermal growth of Mn doped ZnS nanoparticles are given in chapter 4.

7.2.2. Characterization

A Biotech, Power wave XS, USA micro plate reader was used to record the optical absorbance (measuring the intensity of the peak at 570 nm) of the present ZnS samples. A Leica DM IRB, Germany, phase contrast microscope was used for analyzing the aggregation study of the present samples. The imaging efficiency of the samples was recorded with a XENOGEN-IVIS optical imaging system. Cytotoxic studies of the samples were done with MCF7 cells (Michigan Cancer Foundation-7- a breast cancer cell) and L929 fibroblast cell lines.

The cytotoxicity of ZnS microspheres and Mn doped ZnS nanoparticles were investigated by analyzing the cell viability of the system on MCF7 cells by the MTT (3-(4,5-dimethylthiazol-2-yl)-2,5-diphenyltetrazolium bromide) assay method. Different concentrations of the ZnS microspheres/Mn doped ZnS nanoparticles, viz. 0.1, 0.01, 0.05, 0.005 and 0.001mg/ml, were added to the cells and incubated for a time of 24 h. On removal of the media, MTT (0.2 mg/ml) was added to each experimental well and is incubated for 3 h. After removal of MTT, dimethyl sulfoxide was added to the experimental media for dissolving formazan and incubated for 30 min. The optical absorbance was quantified by measuring the intensity of the peak at 570 nm using micro plate reader (Biotech, Power wave XS, USA). Haemocompatibility studies of the samples were done by analyzing the aggregation studies of the samples with human blood cells (RBC, WBC and Platelets). The samples were incubated along with RBC/WBC/Platelets at a temperature of 37 °C for 30 min and the change in morphology was analyzed using a phase contrast microscope. For

investigating the emission properties of the samples for cellular imaging, the material was incubated with L929 fibroblast cell lines for 3 hour and images were recorded using a Leica DM IRB, Germany, phase contrast microscope.

7.3. Results and Discussion

7.3.1. Biocompatibility and Imaging Efficiency of Ethylenediamine Assisted Solvo-hydrothermally grown ZnS Microspheres

7.3.1.1. Cytotoxicity and Hemocompatibility

It is interesting to note that even a concentration of 0.001 mg/ml of the ZnS microspheres leaves 72% of the cells viable indicating the cytofriendly nature of the ZnS microspheres [Figure.7.1]. But the higher doses (0.005, 0.01, 0.05, and 0.1 mg) of the ZnS microspheres are causing more cell deaths, which are cytotoxic to a certain extent.

Table 7.1: Cellular viability vs Concentration of ethylenediamine assisted solvo-hydrothermally grown ZnS microspheres.

Sample concentration (mg)	Cellular viability (%)	S D (±)
0.1	19.78	0.086
0.05	26.18	0.029
0.01	26.94	0.029
0.005	30.28	0.026
0.001	72.19	0.064

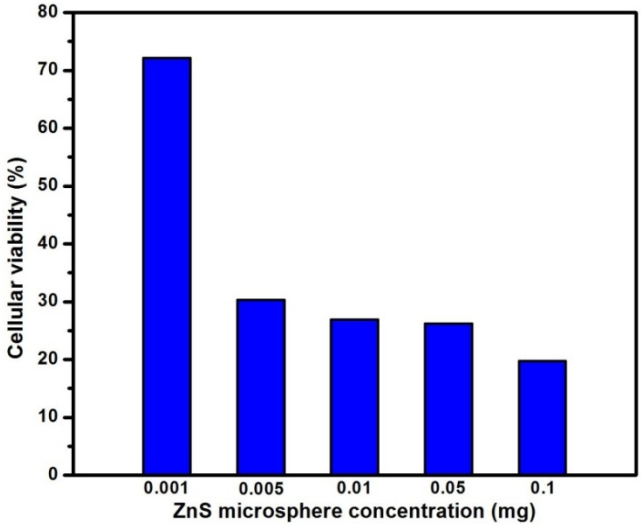

Figure.7.1. *The cytotoxicity study of ethylenediamine assisted solvo-hydrothermally grown ZnS microspheres synthesized at a temperature of 180 °C in MCF-7 cell lines.*

7.3.1.2. Aggregation Studies

The RBC aggregation study of the ZnS microspheres reveals that the morphology of RBC is found to be normal after incubation without showing any aggregation [Figure 7.2]. Similarly after incubation, there is no aggregation of the cells are seen from the phase contrast microscopic images of the WBC treated with ZnS microspheres [Fig 7.2]. The blood platelets aggregation study was also done with the above protocol and the morphology of the platelets are similar without any change after inoculating the cells with the ZnS microspheres used in the present investigation [Figure 7.2].

The present biocompatibility study of the samples shows that the S-H grown ZnS microspheres are both cytocompatible and haemocompatible and can be used for imaging the cells.

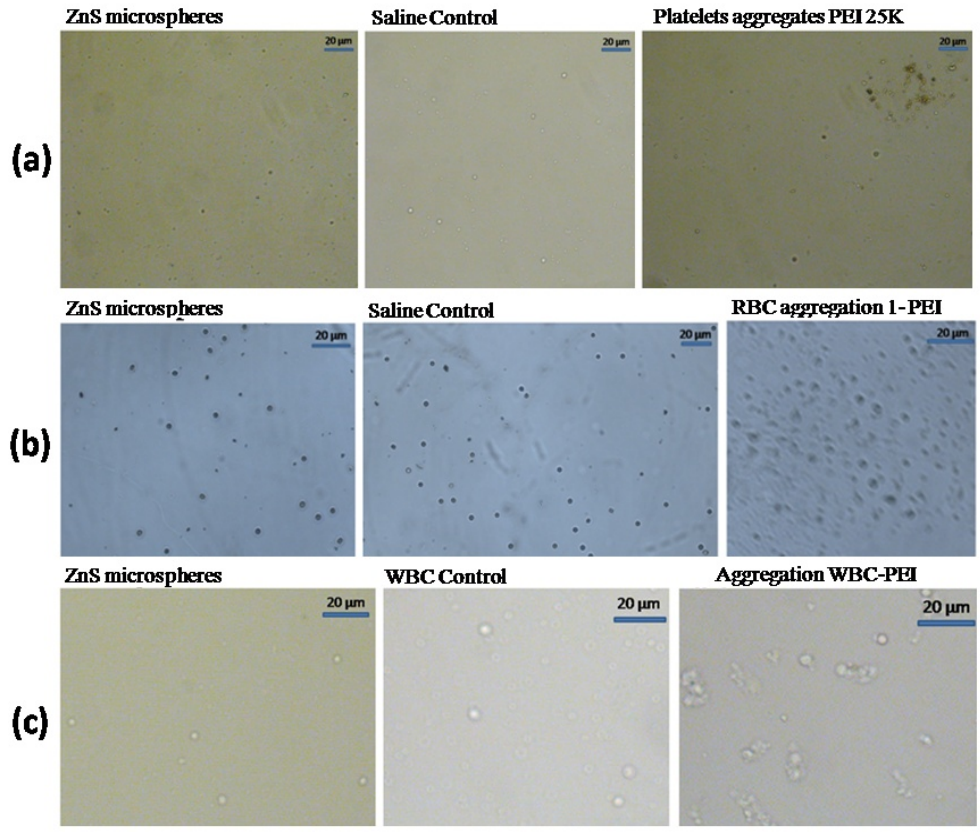

Figure.7.2. *The haemocompatibility (a) Platelet, (b) RBC and (c) WBC aggregation studies of ethylenediamine assisted solvo-hydrothermally grown ZnS microspheres synthesized at a temperature of 180 °C in human blood cells.*

7.3.1.3. Emission Studies

The imaging efficiency of ethylenediamine assisted solvo-hydrothermally grown ZnS microspheres was evaluated using XENOGEN-IVIS spectrum optical imaging system and is given in figure. 7.3. The sample is showing good fluroscence emission as understood from the adjacent color bar in figure.7.3, which is in good agreement with previously described PL results.

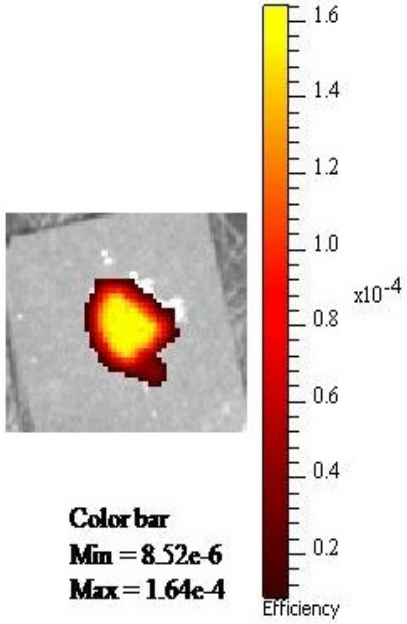

Figure.7.3. *Fluorescence efficiency study (photons/sec/cm^2/sr) of ethylenediamine assisted solvo-hydrothermally grown ZnS microspheres synthesized at a temperature of 180 °C with XENOGEN-IVIS system*

7.3.1.4. Imaging Studies

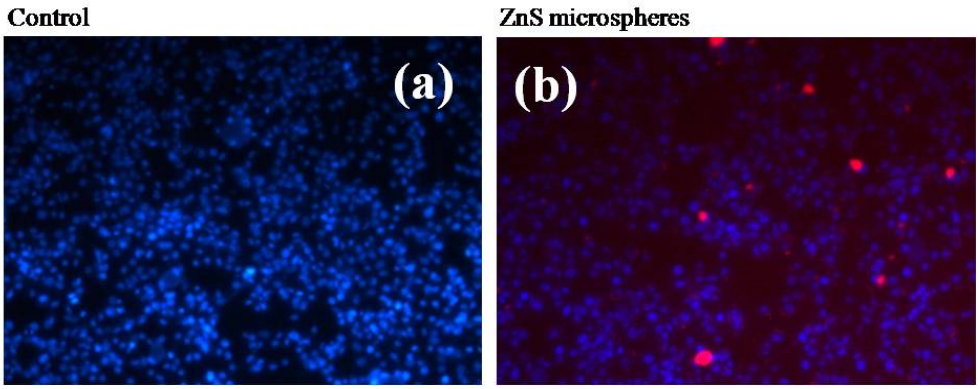

Figure.7.4*. In vitro imaging study of ethylenediamine assisted solvo-hydrothermally grown ZnS microspheres synthesized at a temperature of 180 °C in L929 fibroblast cell lines.*

The fluorescence microscopic images (Figure 7.4 b) shows the emission from the ZnS microspheres which is compared to the cells without the ZnS microspheres (Figure 7.4 a). The partial internalization of the materials would have taken place due to endocytosis or the enhanced permeability and retention (EPR) effect of the cells. The size of the fibroblast cells used in this study has a size range of 5 to 10 μm to facilitate the particle uptake.

7.3.2. Biocompatibility and Imaging Efficiency of Solvo-hydrothermally grown Mn Doped ZnS Nanoparticles

7.3.2.1. Cytotoxicity and Hemocompatibility

About 80% of the cells are viable even with a sample concentration of 0.1 mg (Table 7.2; Figure 7.5). This shows that the samples are non cytotoxic.

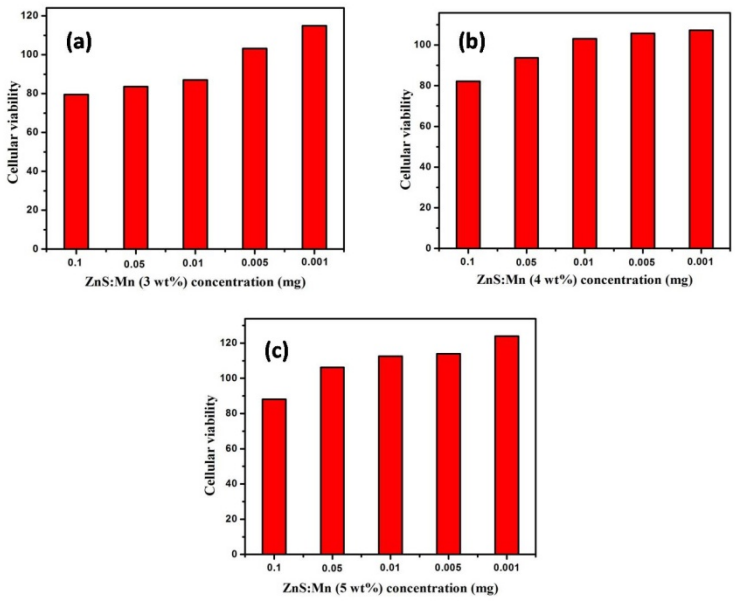

Figure.7.5. *Cytotoxicity study of solvo-hydrothermally grown (a) Mn 3 wt%, (b) Mn 4 wt%, (c) Mn 5 wt% doped ZnS nanostructures synthesized at a growth temperature of 200 °C in MCF-7 cell lines.*

Table 7.2. *Cellular viability vs Concentration of the samples*

	ZnS:Mn 3 wt%		ZnS:Mn 4 wt%		ZnS:Mn 5 wt%	
ZnS:Mn concentration (mg)	**Cellular viability (%)**	**S D (±)**	**Cellular viability (%)**	**S D (±)**	**Cellular viability (%)**	**S D (±)**
0.1	79.47	0.045	82.17	0.012	88.17	0.207
0.05	83.59	0.052	93.71	0.322	106.25	0.281
0.01	87.07	0.872	103.05	0.115	112.61	0.221
0.005	103.19	0.134	105.68	0.200	113.91	0.207
0.001	114.83	0.116	107.19	0.129	123.87	0.069

The haemocompatibility properties of the present samples are revealed by the aggregation studies of Mn doped ZnS with human RBC, WBC and platelets. The WBC, RBC, and the Platelets studies of the present samples indicates the hemocompatibility of the samples under investigations.

7.3.2.2. Aggregation Studies

The platelets aggregation studies of the Mn doped ZnS nanoparticles reveals that the morphology of the platelets remain without any change and cell aggreagation induced by the external agents are not observed (Figure 7.6).

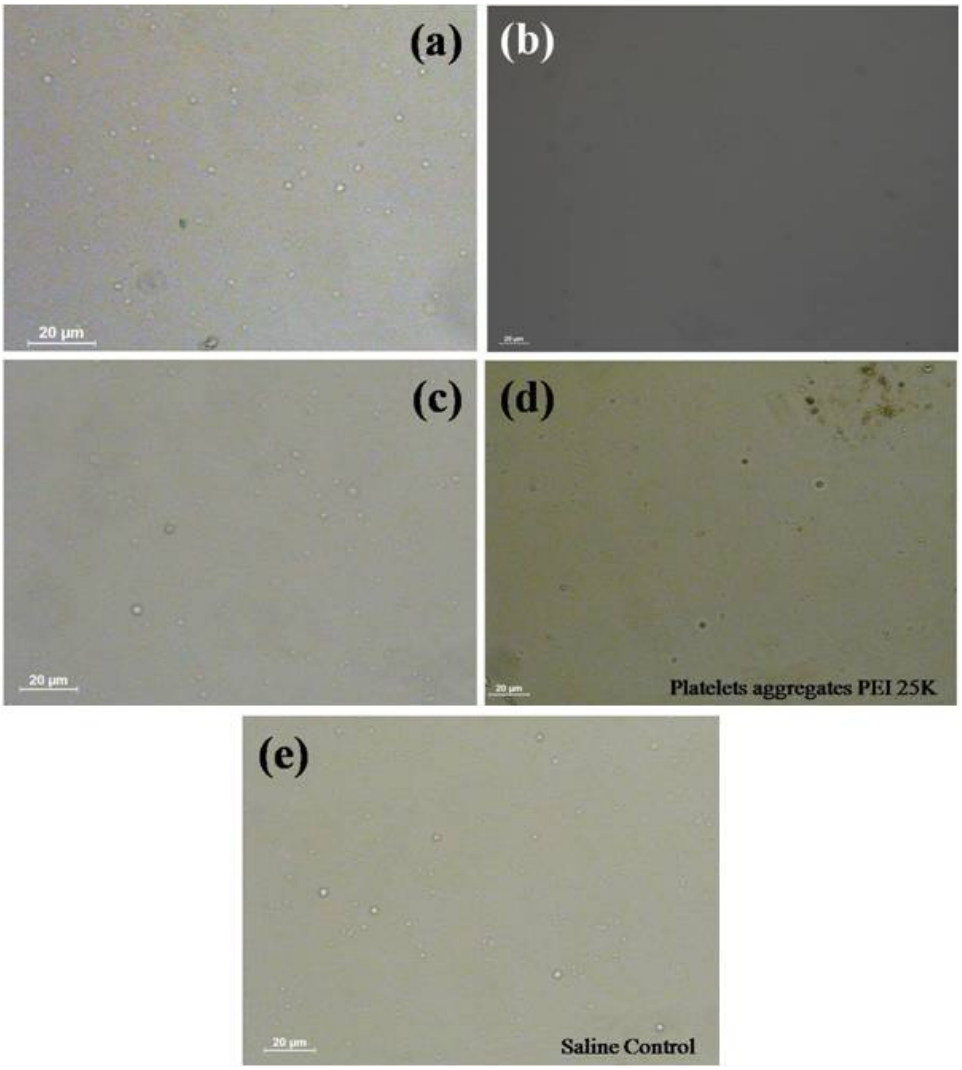

Figure.7.6. *Platelets aggregation study of solvo-hydrothermally grown (a) Mn 3 wt%, (b) Mn 4 wt%, (c) Mn 5 wt% doped ZnS nanostructures synthesized at a growth temperature of 200 °C in human blood cells.*

Similarly the RBC aggregation analysis of the samples shows that the microscopic images are found to be be normal in its morphology (Figure 7.7).

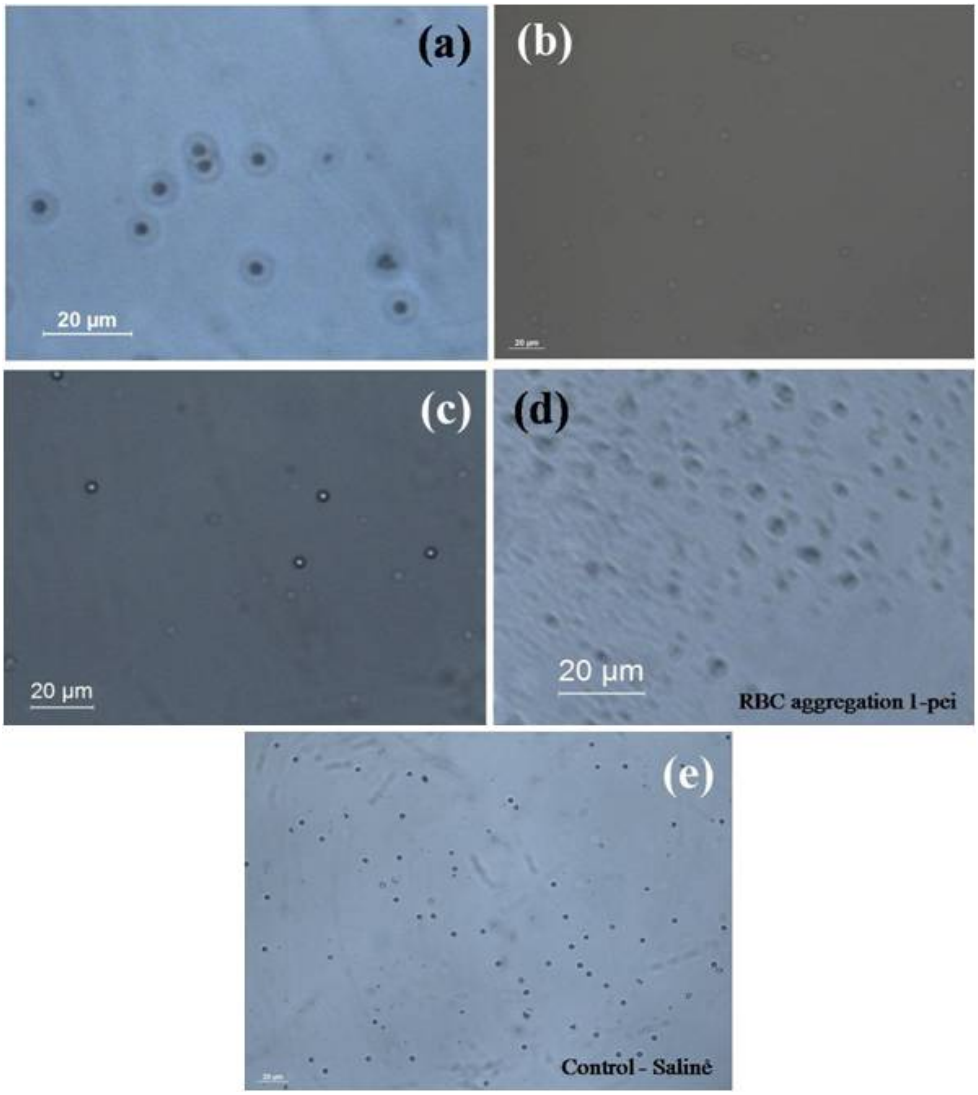

Figure.7.7. *RBC aggregation study of solvo-hydrothermally grown (a) Mn 3 wt%, (b) Mn 4 wt%, (c) Mn 5 wt% doped ZnS nanostructures synthesized at a growth temperature of 200 °C in human blood cells.*

Aggregation of the WBC cells are not seen from the specimen as shown in phase contrast microscopic images in figure 7.8.

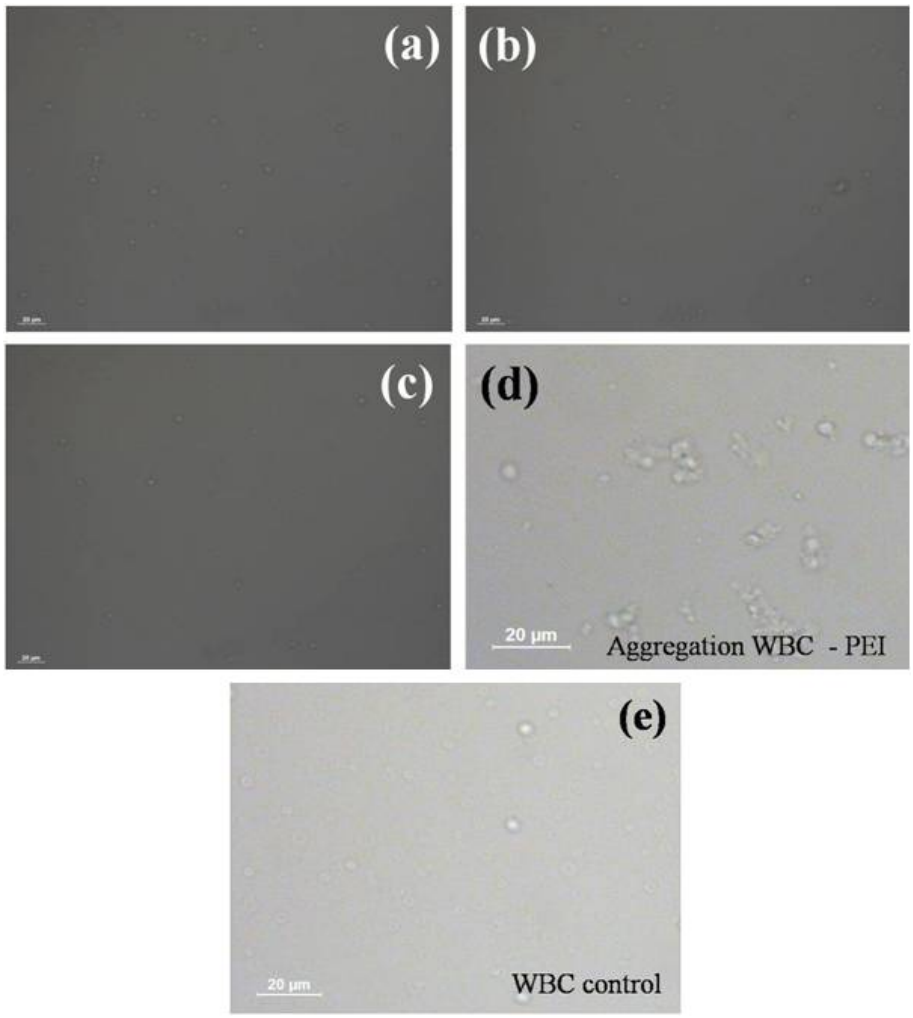

Figure.7.8. *WBC aggregation study of solvo-hydrothermally grown (a) Mn 3 wt%, (b) Mn 4 wt%, (c) Mn 5 wt% doped ZnS nanostructures synthesized at a growth temperature of 200 °C in human blood cells.*

7.3.2.3. Emission Studies

All the samples under investigation shows flourescence. The observed flourescence is in good aggreement with the obtained PL emission as reported previously. All the three samples show good fluorescence emission as evidenced from the color bar shown. It is clear from the figure

7.9, that the Mn 3 wt% doped ZnS sample is having high fluorescence efficiency compared to the other two samples. Whereas Mn 4 wt% doped ZnS sample is having comparatively less emission intensity among the three samples. The reasons for the variation in the emission intensity of the present samples were already reported previously.

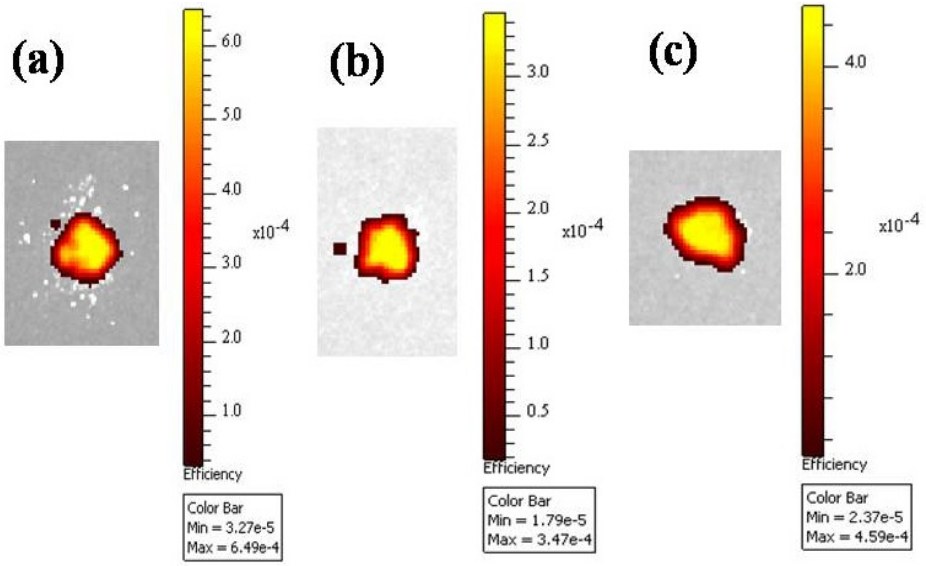

Figure.7.9. *Fluorescence efficiency study (photons/sec/cm^2/sr) of solvo-hydrothermally grown (a) Mn 3 wt%, (b) Mn 4 wt%, (c) Mn 5 wt% doped ZnS nanostructures synthesized at a growth temperature of 200 °C with XENOGEN-IVIS system.*

7.3.2.4. Imaging Studies

The observed emission from the cells with (a,b, and c) and without (d) the samples were shown in figure 7.10. All the samples shows good emission properties as seen from the figure 7.10. Among these, Mn 3 wt% doped ZnS sample (Figure 7.10 (a)) shows high emission which is in agrrement with its PL emission.

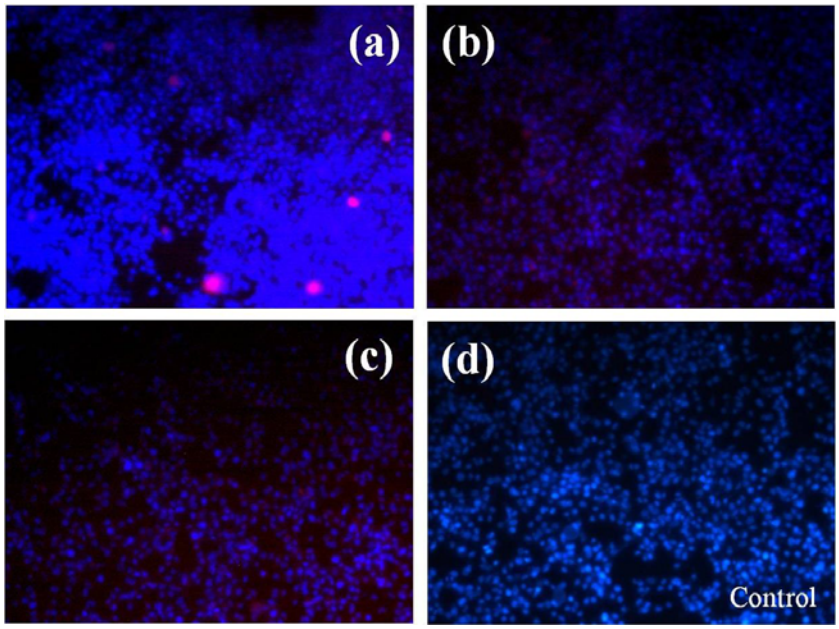

Figure.7.10. *In vitro imaging study of solvo-hydrothermally grown (a) Mn 3 wt%, (b) Mn 4 wt%, (c) Mn 5 wt% doped ZnS nanostructures synthesised at a growth temperature of 200 °C in L929 fibroblast cell lines.*

7.4. Conclusions

Biocompatibility and imaging efficiency of ethylenediamine assisted solvo-hydrothermally grown ZnS microspheres and solvo-hydrothermally grown Mn doped ZnS nanoparticles were investigated. ZnS:Mn 3 wt% sample exhibits more cytocompatibility as compared to ZnS:Mn 4, ZnS:Mn 5 wt% and ZnS microspheres. The presence of Mn dopant contributes to variation in cytocompatibility as well as emission properties. ZnS:Mn 3 wt% is more efficient and suitable for biological applications. Comparatively less toxic and biocompatible ZnS and ZnS:Mn systems with high luminescent yield is a suitable candidate to replace the traditional toxic cadmium based materials for biological applications.

.....ꕥ.....

8 Summary and Future Scope of the Present Work

Chapter

This chapter summarizes the major highlights, general conclusions and the future scope of the present work. The conclusions of the present studies provide new guidelines for growing different morphological structures and to improve the properties of ZnS based phosphors for light emitting as well as bio-imaging applications.

8.1. Summary of the Present Study

Studies on nanoscale materials can give new information with respect to its bulk state. The applications of semiconductor nanocrystals especially quantum dots are emerging rapidly for its wide variety of uses in the field of biotechnology, medicine and optics. II-VI semiconductors are first among the phosphor compounds studied for the applications in cathode ray tube displays. The II-VI semiconductors are usually having wide band gap and high ionicity which are considered as the important material for optoelectronic devices operating under the excitation with UV sources. Among II-VI (i.e, compound of IIb metal with VIa cations) semiconductors, luminescent properties of ZnS can be tuned by intentional dopants as well as by changing its size, shape and morphology.

The thesis deals with the synthesis and photoluminescence studies of micro and nanostructured ZnS by hydrothermal and solvo-hydrothermal method for the bioimaging applications. In summary, the thesis focuses on growth of ZnS with different morphological structures and to investigate its luminous properties.

Relatively oxygen free mesoporous ZnS microstructures are synthesized by solvo-hydrothermal method. XRD and Raman studies of the samples reveals that hydrothermally and solvo-hydrothermally grown ZnS is having cubic sphalerite phase of ZnS. Boosted UV emission at 349 nm is observed from the ZnS prepared by the solvo-hydrothermal route whereas PL emission at 540 nm is observed from hydrothermally grown ZnS. The increased intensity of the UV emission from S-H grown ZnS is probably attributed to activation of whispering gallery modes (WGMs) of almost elliptical microstructures made of porous nanostructures. This material with the complete elimination of defect related emissions can be used for the fabrication of LEDs, UV lasers and in medical field.

Luminescence properties of hydrothermally and solvo-hydrothermally (water-acetonitrile) grown Mn doped ZnS at a reaction temperature of 200 °C is studied. The PL emission of the ZnS doped with 3 and 5 wt% of Mn, synthesized by S-H method are having intense dual wavelength emission at UV and yellow-orange region. ZnS with Mn 3 wt% exhibit higher luminescence yield at 367 nm and at yellow-orange region. The increase in luminescence yield of S-H grown sample with Mn 3 wt% doping is attributed to the increase in population of sulphur vacancies formed due to the higher solubility of the sulphur in acetonitrile and the increase in specific area of grain boundary as grown crystals. Water-acetonitrile combination is a suitable solvent for the production of better luminescent Mn doped ZnS. The chromaticity coordinates (CIE) of the observed yellow-orange emission from the samples are calculated, which fall in the yellow-orange region. The high luminescence yield at 367 nm and in the yellow-orange region from the sample is useful to fabricate white light sources based on this material and also for bio-imaging.

Morphology of ZnS grown by S-H method can be varied by using surfactants like ethylenediamine, polymethyl methacrylate, cetyl trimethylammonium bromide and polyethylene glycol during growth process. ZnS nanoflakes with length of 100-150 nm and width of 20-30 nm are obtained with the use of CTAB whereas particles having size in the range 100-200 nm are formed while using PEG as surfactant. ZnS nanoparticles of size below 100 nm are obtained with the use of PMMA as surfactant and are agglomerated. ZnS microspheres having average diameter of 3.85 μm made of hyperfine particles with 10 nm size are obtained with solvo-hydrothermally (S-H) method using ethylenediamine surfactant, which exhibits broad visible PL emission from 380-580 nm. The broad visible PL emission from the microspheres is attributed to the increase in carrier concentration as understood from the presence of intense Raman band at 257 cm^{-1}. ZnS microspheres with broad visible emission have potential applications in the fields of bioimaging, diagnostic analysis and for the fabrication of white light sources.

The structural and optical properties of ethylenediamine assisted solvo-hydrothermally grown ZnS:Nd_2O_3 host-guest (ZNHG) system were carried out. Wurtzite phase of ZnS exists in ZNHG system instead of cubic phase of ZnS. Narrowing of visible PL emission of ZNHG system with respect to that of cubic ZnS is contributed to the addition of neodymium acetate in the growth system, which favoured the formation of wurtzite phase of ZnS. The Nd 4 and 5 wt% added samples of ZNHG system shows Nd related emission peaks at 860 – 905 nm ($^4F_{3/2}$ to $^4I_{9/2}$ transition) and feeble emission at 1054 and 1071 nm ($^4F_{3/2}$ to $^4I_{11/2}$ transition) as well as the ZnS related blue emission. The observed Nd related emission in the IR

region can be used for the fabrication of IR sources and for bio-imaging applications.

The whole works summarizes that water-acetonitrile solution combination is a suitable solvent for the growth of better luminescent ZnS. Ethylenediamine assisted solvo-hydrothermally grown ZnS microspheres and solvo-hydrothermally grown Mn doped ZnS nanoparticles are cyto- and haemo-compatible, can be used for bio-imaging applications.

8.2. Future Scope of the Present Work

ZnS micro and nanostructures are synthesized in the present study by low temperature hydrothermal and solvo-hydrothermal method. ZnS micro and nanostructures with enhanced luminescence properties can be developed by modifying the reaction conditions of solvo-hydrothermal method. The synthesis of transition metal doped ZnS micro and nanostructures with high luminescence are possible with solvo-hydrothermal method especially for light emitting device applications. In the present work, water-acetonitrile solution combination (in 1:1 ratio) is used as solvent for the synthesis of ZnS micro and nanostructures. So attempts can be made to check the possibility of using other solvents in solvo-hydrothermal method for the growth of ZnS with unique physical and optical properties. Similarly, the growth condition of ZnS can be varied by the addition of surfactants as well as different capping agents. Transition metal (Fe,Ni,Co,Mn) doped ZnS likely to exhibit magnetic properties which may have extensive applications in drug delivery systems as well as in the area of spintronics. Rare earth metal doping in ZnS is much difficult with normal reaction procedures as understood from previous as well as present study. The optimisation of experimental conditions for the incorporation of rare-earth ions on ZnS is

another interesting area of interest in the future. Since RE^{3+} ions will give luminescence emissions especially in the region from red end of the electromagnetic spectrum to IR region. Hence these materials are technologically important for the fabrication of next generation IR sources. Apart from that these materials are used for bio-imaging applications because of its emission in the IR region. Some of the RE^{3+} doped or host-guest systems exhibit magnetic properties. These magnetic materials are having future prospects as drug delivery purpose and data storage applications based on its magnetic properties. ZnS obtained from hydothermal/solvo-hydrothermal method with different morphology depending on its growth, crystallises in sphalerite cubic system. These materials are expected to show phase transition when it is subjected to high pressure and temperature. The phase transition studies of these materials can be carried out with Raman, PL and XRD techniques. This information is very useful for the fabrication of devices based on ZnS, for different technological applications. The growth of ZnS using oxygenated salts sometimes generates oxygen related impurities in as grown ZnS materials. These oxygen impurities may contribute variation in physical and optical properties of these materials. So growth of ZnS in oxygen free solvents in inert atmosphere is an interesting research problem, for future research. Further, information on toxicity of nanomaterial is required for its biological applications as well as environmental safety are concerned. Investigation on nanotoxicity of ZnS nanomaterials are another interesting research problem for the future.

Abbreviations

AlGaAs	Aluminium gallium arsenide
ATR	Attenuated Total Reflection
CBD	Chemical Bath Deposition
CCD	Charge Coupled Device
CdS	Cadmium sulphide
CdSe	Cadmium selenide
CdTe	Cadmium telluride
CeAs	Cerium arsenide
CIE	Commission Internationale de lEclairage
CRT	Cathode ray tube
CTAB	Cetyl trimethyl ammonium bromide
CVD	Chemical Vapour Deposition
DDAB	Didodecyldimethylammonium bromide
DNCs	Doped nanocrystals
DOS	Density of states
DRS	Diffuse Reflectance Spectroscopy
EDA	Ethylenediamine
EDTA	Ethylenediaminetetraacetic acid
EDAX	Energy Dispersive X-ray spectroscopy
EtBr	Ethidium bromide
fcc	Face centered cubic
FESEM	Field Emission Scanning Electron Microscope
FTIR	Fourier Transform Infrared spectroscopy
FT-Raman	Fourier Transform Raman spectroscopy

FWHM	Full Width at Half Maximum
GaAs	Gallium arsenide
GaN	Gallium nitride
Ge	Germanium
H_C	Coercivity field
hcp	Hexagonal close packed
HVS	Human visual system
InGaAs	Indium gallium arsenide
InP	Indium phosphide
LED	Light emitting diode
LO	Longitudinal optical
LOPC	LO phonon-plasmon coupled mode
MBE	Molecular Beam Epitaxy
MCF7 cell	Michigan Cancer Foundation-7 cell
MOCVD	Metal Organic Chemical Vapour Deposition
MRI	Magnetic resonance imaging
MTT	MTT (3-(4, 5-dimethylthiazol-2-yl)-2, 5-diphenyltetrazolium bromide)
NBE	Near-band edge
Nd:YAG	Neodymium Yttrium Aluminium Garnet
nm	Nanometer
NP	Nanoparticle
NRs	Nanorods
PbS	Lead sulphide
PEG	Polyethylene glycol
PET	Positron emission tomography
PID	Proportional Integral Derivative

PL	Photoluminescence
PLD	Pulsed Laser Deposition
PLE	Photoluminescence excitation
PMMA	Polymethyl methacrylate
PMT	Photomultiplier tube
PrN	Praseodymium nitride
PTA	Photothermal ablation
PVD	Physical Vapour Deposition
PVP	Polyvinylpyrrolidone
Q dots	Quantum dots
QW	Quantum Well
RBC	Red blood cells
RE	Rare Earth
RGO	Reduced grapheme oxide
RTP	Room temperature phosphorescence
SAED	Selected Area Electron Diffraction
SBDs	Schottky barrier diodes
SCF	Supercritical fluids
SCW	Supercritical water
SEM	Scanning Electron Microscopy
SERS	Surface enhanced Raman Spectroscopy
s_{GB}	Specific area of grain boundary
S-H	Solvo-hydrothermal
SiC	Silicon carbide
SPD	Spectral power density
SPR	Surface plasmon resonance
T_C	Curie temperature

TEM	Transmission Electron Microscope
TG	Thioglycerol
T_N	Néel temperature
TO	Transverse optical
TOP	Triocytlphosphine
TOPO	Triocytlphosphine oxide
UV	Ultra violet
WBC	White blood cells
WGMs	Whispering gallery modes
WLEDs	White LEDs
XRD	X-Ray Diffraction
ZNHG	ZnS:Nd_2O_3 host-guest system
ZnO	Zinc oxide
ZnS	Zinc sulphide
ZnSe	Zinc selenide

References

[1] Aby C P, Veeranarayanan S, Nagaoka Y, Yoshida Y, Maekawa T and Kumar D S, Materials Express, **2**, 94 (2012a).

[2] Aby C P, Veeranarayanan S, Nagaoka Y, Yoshida Y, Maekawa T and Kumar D S, J. Fluorescence, **22**, 931 (2012b).

[3] Acharya S A, Maheshwari N, Tatikondewar L, Kshirsagar A and Kulkarni S K, Cryst. Growth. Des., **13**, 1369 (2013).

[4] Arndt D, Zielasek V, Dreher W and Bäumer M, J. Colloid. Interf. Sci., **417**, 188 (2014).

[5] Baiju K V, Periyat P, Wunderlich W, Pillai P K, Mukundan P and Warrier K G K, J. Sol-Gel. Sci. Technol., **43**, 283 (2007).

[6] Banwell C N and McCash E M, Fundamentals of molecular spec- troscopy. Tata McGraw Hill, 4th edition (1994).

[7] Barber J, Brutin D and Tadrist L, Nanoscale Res. Lett., **6**(1), 1 (2011).

[8] Bean C P and Livingston J D, J. Appl. Phys., **30**, 120S (1959).

[9] Bedanta S and Kleemann W, J. Phys. D, **42**, 013001 (2009).

[10] Beeby A, Burton-Pye B P, Faulkner S, Motson G R, Jeffery J C, McCleverty J A and Ward M D, J. Chem. Soc., Dalton Trans., 1923 (2002).

[11] Bera D, Qian L, Tseng T K and Holloway P H, Materials, **3**, 2260 (2010).

[12] Bhargava R N, Gallagher D, Hong X and Nurmikko A, Phys. Rev. Lett., **72,** 416 (1994).

[13] Bhirud A, Chaudhari N, Nikam L, Sonawane R, Patil K, Baeg J O and Kale B, Int J. Hydrogen Energ., **36**, 11628 (2011).

[14] BiIlmeyer F W and Saltzman M, Principles of color technology. New York: John Wiley and Sons, second ed., (l981).

[15] Biju V, Itoh T, Anas A, Sujith A and Ishikawa M., Anal. Bioanal. Chem., **391**(7), 2469 (2008).

[16] Bodo B, Singha R and Das S C, Int.J.App.Phy.and Math., **2**(4), 287(2012).

[17] Bol A A, Beek R V and Meijerink A, Chem. Mater., **14**, 1121 (2002).

[18] Bouras K, Rehspringer J L, Schmerber G, Rinnert H, Colis S, Ferblantier G, Balestrieri M, Ihiawakrim D, Dinia A and Slaoui A, J. Mater. Chem. C, **2**, 8235 (2014).

[19] Brown E, Hanley C B, Hommerich U, Bluiett A G and Trivedi S B, J. Lumin., **133**, 244 (2013).

[20] Bruchez M, Moronne M, Gin P, Weiss S and Alivisatos A P, Science, **281**, 2013 (1998).

[21] Bruno A, Borriello C, Luccio T D, Nenna G, Sessa L, Concilio S, Haque S A and Minarini C, J. Nanopart Res., **15**, 2085 (2013).

[22] Brus L E, J. Phys. Chem., **90**, 2555 (1986).

[23] Buerger M J, X-ray Crystallography. John Wiley and Sons, New York, 3rd edition, (1962).

[24] Bushiri M J, Gopakumar V and Vaidyan V K, Surf. Rev. Lett., **15**, 551(2008).

[25] Buzea C, Blandino I I P and Robbie K, Biointerphases, **2**(4), MR17 (2007).

[26] Byrappa K and Adschiri T, Progress in Crystal Growth and Characterization of Materials, **53**, 117 (2007).

[27] Byrappa K, Yoshimura I and Yoshimura M, Hand book of Hydrothermal Technology, William Andrew Publishing, New York (2001).

[28] Cao G. Nanostructures & Nanomaterials: Synthesis, Properties & Applications. Imperial College Press, London (2004).

[29] Cash K J and Clark H A, Trends in Mol. Med., **16** (12), 584 (2010).

[30] Chae W S, Yoon J H, Yu H, Jang D J, and Kim Y R, J. Phys. Chem. B, **108**, 31 (2004).

[31] Chakraborty M, Hsiao F W, Naskar B, Chang C H and Panda A K, Langmuir, **28**, 7282 (2012).

[32] Chander H, Mater. Sci. and Eng. R., 49**,** 113 (2005).

[33] Chatterjee A, Priyam A, Bhattacharya S C and Saha A, Colloids Surf. A, Physicochem. Eng. Asp., **297**, 258 (2007).

[34] Chen D, Chen Y, Lu H, and Ji Z, Inorg. Chem., **53**, 8638 (2014).

[35] Chen Z W, Lai J K L and Shek C H, Phys. Rev. B. **70**, 165314 (2004).

[36] Cheng C, Xu G, Zhang H, Cao J, Jiao P and Wang X, Mat. Lett., **60**, 3561(2006).

[37] Cheng Y C, Jin C Q, Gao F, Wu X L, Zhong W, Li S H, and Chu P K., J. Appl. Phys., **106**, 123505,(2009).

[38] Cheng Y, Samia A C, Meyers J D, Panagopoulos I, Fei B and Burda C. J. Am. Chem. Soc., **130**(32),10643 (2008).

[39] Cholan S, Shanmugam N, Kannadasan N, Sathishkumar K and Deivam K, J. Mater. Res. Technol., **3**(3), 222 (2014).

[40] Choube S R, Gedam S C and Dhoble S J, Rec Res in Sci and Tech., **4**(8), 75(2012).

[41] Colombo M, Carregal-Romero S, Casula M F, Gutierrez L, Morales M P, Bohm I B, Heverhagen J T, Prosperi D and Parak W J, Chem. Soc. Rev., **41**, 4306 (2012).

[42] Cullity B D and Stock S R, Elements of X ray diffraction. Prentice Hall, New Jersey, 3rd edition, (2001).

[43] Darbandi M, Thomann R and Nann T, Chem. Mater., **17**(23), 5720 (2005).

[44] Dillip G R, Dhoble S J and B Deva Prasad Raju, Opt. Mat., **35**, 2261(2013).

[45] Dillip G R, Mallikarjuna K, Dhoble S J and B Deva Prasad Raju, J. Phys. and Chem. Solids, **75,** 8 (2014).

[46] Dong L, Chu Y, Zhang Y, Liu Y and Yang F, J. Coll. and Inter. Sci., **308,** 258 (2007).

[47] Donne A L, Jana S K, Banerjee S, Basu S and Binetti S, J. Appl. Phys., **113,** 014903 (2013).

[48] Dubertret B, Skourides P, Norris D J, Noireaux V, Brivanlou A H and Libchaber A, Science., **298** (5599), 1759 (2002).

[49] Durgadas C V, Sreenivasan K and Sharma C P, Biomaterials, **33**, 6420 (2012).

[50] Dutta D P, Manoj N and Tyagi A K, J. Lumin., **131,** 1807 (2011).

[51] Dykman L A and Khlebtsov N G, Acta Naturae, **3**(2), 34 (2011).

[52] Edelstein R L, Tamanaha C R, Sheehan P E, Miller M M, Baselt D R, Whitman L J and Colton R J, Biosensors Bioelectron., **14**, 805 (2000).

[53] Efros A L and Efros A L. Sov. Phys. Semicond., **16**, 772 (1982).

[54] Efros A L and Rosen M. Annu. Rev. Mater Sci., **30**, 475 (2000).

[55] Fan G, Wang C and Fang J, Nano Today, **9**, 69 (2014).

[56] Fan H, Leve E W, Scullin C, Gabaldon J, Tallant D, Bunge S, Boyle T, Wilson M C and Brinker C J, Nano Lett., **5** (4),645 (2005).

[57] Fan J and Wang L, J. Heat Transf., **133**(4), 040801 (2011).

[58] Fan Z and Lu J G. Appl. Phys. Lett., **86**, 123510 (2005).

[59] Fang X and Zhang L, J. Mater. Sci. Technol., **22** (6) (2006).

[60] Flewitt P E J and Wild R K, Physical methods for materials characterisation., IOP Publishing Ltd (2003).

[61] Fojtik A, Weller H, Koch U, Henglein A and Bunsenges B. Phys. Chem., **88,** 969 (1984).

[62] Fujiwara H, Hosokawa H, Murakoshi K, Wada Y and Yanagida S, Langmuir, **14**,5154(1998).

[63] Gao X, Cui Y, Levenson R M, Chung L W K and Nie S, Nat. Biotech, **22**(8):969 (2004).

[64] Garnett E C, Liang W and Yang P. Adv. Mater., **19**, 2946 (2007).

[65] Gatoo M A, Naseem S, Arfat M Y, Dar A M, Qasim K and Zubair S, Hindawi Publishing Corporation Bio. Med. Res. Int., Article ID 498420 (2014).

[66] Gazit E. Imperial College press (2007).

[67] Geszke-Moritz M, Piotrowska H, Murias M, Balan L, Moritz M, Lulekb J and Schneider R, J. Mater. Chem. B, **1**, 698 (2013).

[68] Ghosh D, Hussain S, Ghosh B, Bhar R and Pal A K, ISRN Mat. Sci. Article ID 521701, http://dx.doi.org/10.1155/2014/521701. (2014).

[69] Greeff A P and Swart H C, Surf. and Interface Anal., **29(12),** 807 (2000).

[70] Greeff A P and Swart H C, Surf. and Interface Anal., **31,** 448 (2001).

[71] Guo N, Lu W, Jia Y, Lv W, Zhao Q, and You H, Chem. Phys. Chem., **14,** 192, (2013).

[72] Guo W, Sun X, Jacobson Yan X, Min K, Srivatsan A, Niu G, Kiesewetter D O, Chang J and Chen X, ACS Nano, **9** (1), 488 (2015).

[73] Hafeez M, Rehman S, Manzoor U, Khan M A and Bhatti A S, Phys. Chem. Chem. Phys., **15**, 9726 (2013).

[74] Haglund E, Goldsmith M M S and Leary J F, Ann. Biomed. Eng., **37**(10), 2048 (2009).

[75] Han M, Gao X, Su J Z and Nie S, Nature Biotechnology , **19**, 631(2001).

[76] Hartmann H, Mach R and Selle B, "Wide Gap II-VI Compounds as Electronic Materials, in current Topics in Materials Science", edit by E. Kaldis, (North-Holloand Pablishing Company) (1982).

[77] Haruta M, Tsubota S, Kobayashi T, Kageyama H, Genet M J and Delmon B. J. Catal., **144**, 175 (1993).

[78] Hayashi H and Hakuta Y, Materials, **3**, 3794 (2010).

[79] He L, Ji S P, Tang N, Zhao Y and Tao G H, Dalton Trans., **44**, 2325 (2015).

[80] He Y, Wang H F and Yan X P, Anal. Chem., **80** (10), 3832 (2008).

[81] Herring C and Galt J K. Phys. Rev., **85**,1060 (1952).

[82] Hoa T T Q, The N D, McVitie S, Nam N H, Vu L V, Canh T D and Long N N, Opt. Mat., **33,** 308 (2011).

[83] Hsieh J M, Ho M L, Wu P W, Chou P T, Tsaib T T and Chi Y, Chem. Commun., **615** (2006).

[84] http1- http://www.fei.com/products/tem/tecnai/)

[85] http2- https://en.wikipedia.org/wiki/CIE_1931_color_space

[86] http3-http://hyperphysics.phyastr.gsu.edu/hbase/vision/imgvis/cie4. gif

[87] Hu H and Zhang W, Opt. Mater., **28,** 536 (2006).

[88] Huang Y, Cai Y and Liu H, Particuology, **9,** 533 (2011).

[89] Huh Y D, Park J Y, Kweon S S, Kim J H, Kim J G and Do Y R, Bull. Korean Chem. Soc., **25,** 1585 (2004).

[90] Ibupoto Z H, Khun K, Liu X and Willander M, Nanomaterials, **3**, 564 (2013).

[91] Indira T K and Lakshmi P K, Int. J. Pharm. Sci. and Nanoteh., **3**(3), 1035 (2010).

[92] Ingle J D and Crouch S R, Spectrochemical Analysis, Prentice-Hall Int. New Jersey (1988).

[93] Issa B, Obaidat I M, Albiss B A and Haik Y, Int. J. Mol. Sci., **14**, 21266 (2013).

[94] Javey A, Woo S, Friedman R S, Yan H and Lieber C M, Nano. Lett., **7**, 773 (2007).

[95] Jayasimhadri M , Ratnam B V , Jang K , Lee H S , Yi S S and Jeong J H, Thin Solid Films, **518**, 6210 (2010).

[96] Jian D, Gao Q, Li N and Ruan M, Mater. Lett., **61**, 4471 (2007).

[97] Jiang Y, Meng X M, Liu J, Xie Z Y, Lee C S and Lee S T, Adv. Mater., **15**, 323 (2003).

[98] Kagan C R, C.B. Murray C B and Bawendi M G, Phys. Rev. B-Cond. Mat., **54**, 8633 (1996) a.

[99] Kagan C R, Murray C B, Nirmal M and Bawendi M G, Phys. Rev. Lett., **76**, 1517 (1996) b.

[100] Kajiwara K, Hida T and Tanaka K, J. Vac. Sci. Technol. B, **21,** 515 (2003).

[101] Kandlikar S G, J. Heat Trans-T ASME, **134**, 034001 (2012).

[102] Kao C C and Liu Y C, Mater. Chem and Phys., **115,** 463(2009).

[103] Kapon E, Walthef M, Christen J, Grundmann M, Caneau C, Hwang D M, Colas E, Bhar R, Song G H and Bimberg D, Superlattices and Microstructures, **12** (4), 491 (1992).

[104] Kar S and Chaudhuri S, Chem. Phys. Lett., **414**, 40 (2005).

[105] Katano H, Uematsu K and Tsukatani T, Analy. Sci., **27,** 1249 (2011).

[106] Khosravi A A, Kundu M, Kuruvilla B A, Shekhawat G S, Gupta R P, Sharma A K, Vyas P D and Kulkarrni S K, Appl.Phys. Lett., **67** (17), 2506 (1995).

[107] Kingsley J D and Prener J S, J. Appl. Phys., **43 (7**), 3073 (1972).

[108] Kittel C, Introduction to solid state Physics. Wiely Eastern Limtd (1996).

[109] Kole A K and Kumbhakar P, Results in Physics, **2**, 150 (2012).

[110] Kole A K, Tiwary C S and Kumbhakar P, J. Appl. Phys., **113,** 114308 (2013a).

[111] Kole A K, Tiwary C S and Kumbhakar P, Cryst. Eng. Comm., **15**, 5515 (2013b).

[112] Kubelka P and Munk F, Zh. Tekh. Fiz, 12:593 (1931).

[113] Kubelka P, J. Opt. Soc. Am., **38**, 448 (1948).

[114] Kumar S S, Khadar M A, Dhara S K, Ravindran T R and Nair K G M, Nucl. Instr. and Meth. in Phys. Res. B, **251**, 435 (2006).

[115] Kumar S, Gradzielski M and Mehta S K, RSC Adv., **3**, 2662 (2013).

[116] Kumbhakar P, Ray S S and Stepanov A L, J. Nanomaterials, Article ID 181365, (2014).

[117] Kurita A, Kanematsu Y, Watanabe M, Hirata K and Kushida T, J. Lumin., **87–89,** 986 (2000).

[118] Kushida T, Kurita A, Watanabe M, Kanematsu Y, Hirata K, Okubo N and Kanemitsu Y, J. Lumin., **87–89**, 466 (2000).

[119] Labiadh H, Chaabane T B, Piatkowski D, Mackowski S, Lalevée J, Ghanbaja J, Aldeek F and Schneider R, Mater. Chem. and Phys., **140,** 674 (2013).

[120] Lee J Y, Nam D H, Oh M H, Kim Y, Choi H S, Jeon D Y, Park C B and Nam Y S, Nanotechnology, **25**, 175702 (2014).

[121] Lee S, Song D, Kim D, Lee J, Kim S, Park I Y and Choi Y D, Mater. Lett., **58,** 342 (2003).

[122] Li G, J. Zhai, Li D, Fang X, Jiang H, Dong Q and Wang E, J. Mater. Chem., **20**, 9215(2010).

[123] Li H, Wang G, Zhang F, Cai Y, Wang Y and Djerdj I, RSC Advances, **2**, 12413 (2012).

[124] Li J, Zhao D, Meng X, Zhang Z, Zhang J, Shen D, Lu Y, and Fan X, J. Phys. Chem. B, **110**, 14685(2006).

[125] Li Q and Wang C, Appl. Phys. Lett., **83**, 359 (2003).

[126] Li Y, Lu A, Wang C and Wu X, Sol. Energy. Mater. Sol. Cells., **92,** 953 (2008).

[127] Li Y, Zhang S, Gao L, Chen W, Gao L, Zhang W, Cui J and Yan S, Synth. React. Inorg. Met.-Org. Nano-Metal Chem., **44**, 942 (2014).

[128] Liab J and Zhu J J, Analyst, **138**, 2506 (2013).

[129] Liu L W, Hu S Y, Pan Y , Zhang J Q, Feng Y S and Zhang X H, Beilstein J. Nanotechnol., **5**, 919 (2014).

[130] Liu X Y, Tian B Z, Yu C Z and Zhao D Y, Chem. Lett., **33**, 522 (2004).

[131] Liu X, Mater. Chem. Phys., **91**, 212 (2005).

[132] Lorbeer C and Mudring A V, J. Phys. Chem. C, **117**, 12229 (2013).

[133] Lu S H, Chen T F, Wang A J, Wu Z L, Wang Y S, Appl. Surf. Sci., 299, 116 (2014).

[134] Lu W, Xiong C, Zhang G, Huang Q, Zhang R, Zhang J Z and Li C, Clin Cancer Res., **15**(3), 876 (2009).

[135] Lu X, Yang J, Fu Y, Liu Q, Qi B, Lu C and Su Z, Nanotech., **21,** 115702 (2010).

[136] Lu Y, Su Y, Zhou Y, Wang J, Peng F, Zhong Y, Huang Q, Fan C and He Y. Biomaterials, **34**(17), 4302 (2013).

[137] Lue J T, Encyclopedia of Nanoscience and Nanotechnology, Edited by H. S. Nalwa, **1**–46 (2007).

[138] Luo P G, Sahu S, Yang S T, Sonkar S K, Wang J, Wang H, LeCroy G E, Cao L and Sun Y P, J. Mater. Chem. B, **1**, 2116 (2013).

[139] Luo S, Zhang E, Su Y, Cheng T and Shi C, Biomaterials, **32,** 7127 (2011).

[140] Luo Y, Duan G, Ye M, Zhang Y and Li G, J. Phys. Chem. C, **112**, 2349 (2008).

[141] Ma C, Moore M, Li J and Wang Z L, Adv. Mater., **15**, 228 (2003).

[142] Ma J, Wong H, Kong L B and Peng K W, Nanotechnology, **14**, 619 (2003).

[143] Ma X, Song J and Yu Z, Thin Solid Films, **519,** 5043 (2011).

[144] Maestro L M, Hernandez J E R, Bogdan N, Capobianco J A, Vetrone F, Sole J G and Jaque D, Nanoscale, **4**, 298 (2012).

[145] Mah C, Fraites T J, Zolotukhin J I, Song S, Flotte T R, Dobson J, Batich C and Byrne B J, Mol. Therapy., **6** (1), 106 (2002).

[146] Mah C, Zolotukhin I, Fraites T J, Dobson J, Batich C and Byrne B J, Mol. Therapy, **1**, S239 (2000).

[147] Mahian O, Kianifar A and Kalogirou S A, Int. J. Heat Mass Tran., **57**(2), 582 (2013).

[148] Mahtab R, Rogers J P and Murphy C J, J. Am. Chem. Soc., **117**, 9099 (1995).

[149] Maio J R D, Kokuoz B and Ballato J, Opt Express, **14**, 11412 (2006).

[150] Malik M A, O'Brien P and Revaprasadu N, J. Mater. Chem., **11**, 2382 (2001).

[151] Mandal A and Tamai N, Chem. Phys. Lett., **507,** 248 (2011).

[152] Manna L, Scher E C, Li L S and Paul Alivisatos A, J. Am. Chem. Soc., **124**, 7136(2002).

[153] Mansoori G A and Fauzi Soelaiman T A, Journal of ASTM International, **2** (6), 1-22 (2005).

[154] Mansur H S, Mansur A A P, Soriano-Araújoa A and Lobato Z I P, Green Chem., **17**, 1820 (2015).

[155] Manzoor K, Vadera S R, Kumar N and Kutty T R N, Mater. Chem. Phys., **82,** 718 (2003).

[156] Manzoor K, Vadera S R, Kumar N and Kutty T R N, Solid State Commun., **129,** 469 (2004).

[157] Medintz IL, Berti L, Pons T, Grimes A F , English D S, Alessandrini A, Facci P and Mattoussi H, Nano Lett., **7**(6), 1741(2007).

[158] Mehta S K and Kumar S, J. Lumin., **130**, 2377 (2010a).

[159] Mehta S K, Kumar S, Chaudhary S and Bhasin K K, Nanoscale, **2**, 145 (2010b).

[160] Melancon M P, Lu W, Yang Z, Zhang R, Cheng Z, Elliot A M, Stafford J, Olsen T, Zhang J Z and Li C, Mole. Cancer Therapeutics **7**, 1730 (2008).

[161] Meng X M, Liu J , Jiang Y , Chen W W, Lee C S, Bello I and Lee S T, Chem. Phy. Lett., **382**, 434(2003).

[162] Michalet X, Pinaud F F, Bentolila L A, Tsay J M, Doose S, Li J J, Sundaresan G, Wu A M, Gambhir S S and Weiss S, Science, **307**(5709), 538 (2005).

[163] Mondal C, Ganguly M, Jaya Pal, Roy A, Jana J, and Pal T, Langmuir, **30**, 4157 (2014).

[164] Moritz M G, Piotrowska H, Murias M, Balan L, Moritz M, Lulek J and Schneider R, J. Mater. Chem. B., **1,** 698 (2013).

[165] Muhr V, Wilhelm V S, Hirsch T and Wolfbeis O S, Acc. Chem. Res., **47**, 3481 (2014).

[166] Mulvaney P, Liz-Marzan LM, Giersig M and Ung T., J. Mater. Chem., **10**(6), 1259 (2000).

[167] Murray G M, Pesterfield L L, Stump N A and Schweitzer G K, Inorg. Chem., **28**, 1994 (1989).

[168] Murugadoss G and Rajesh Kumar M, Appl Nanosci., **4**, 67 (2014).

[169] Murugadoss G and Ramasamy V, Luminescence, **28**, 69 (2013).

[170] Muruganandham M, Amutha R and Sillanpaa M, ACS Appl. Mater. Inter., **2**, 1817 (2010).

[171] Muruganandham M, Amutha R, Repo E, Sillanpaa M, Kosumoto Y, and Al-Mamun M A, Photochem and Photobio A: Chemistry, **216**, 133 (2010).

[172] Nagaraju G and Chandrappa G T, J. Mater. Sci. Technol., **28** (6), 495(2012).

[173] Nakamura S, Mukai T and Senoh M, Appl. Phys. Lett., **64**, 1687(1994).

[174] Nann T and Mulvaney P, Angew. Chem. Int. Ed., **43**, 5393 (2004).

[175] Nguyen T T, Trinh X A, Nguyen L H and Pham T H, Adv. Nat. Sci.: Nanosci. Nanotechnol., **2**, 035008 (2011).

[176] Nosaka Y, Yamaguchi K, Miyama H and Hayashi M, Chem. Lett., **17,** 605 (1988).

[177] Nozik A J, Williams F, Nenadovic M T, Rajh T and Micie O I, J. Phys. Chem., **89**, 397 (1985).

[178] Okazaki K, Shimogaki T, Fusazaki K, Higashihata M, Nakamura D, Koshizaki N and Okada T, Appl. Phys. Lett., **101**, 211105 (2012).

[179] Ozin G A and Cademartiri L, Small, **5** (11), 1240 (2009).

[180] Pan A, Liu R, Yang Q, Zhu Y, Yang G, Zou B and Chen K, J. Phys. Chem. B, **109**, 24268 (2005).

[181] Park S, Jin C, Kim H, Hong C and Lee C, J. Lum,**132**, 231(2012).

[182] Pathak C S, Pathak P K, Kumar P and Mandal M K, J. Ovonic Research, **8**(1) 15 (2012).

[183] Peng L and Wang Y, Nanoscale. Res.Lett., **5**, 839 (2010).

[184] Peng Q, Jie J, Xie C, Wang L, Zhang X, Wu D, Yu Y, Wu C, Wang Z and Jiang P, Appl. Phys. Lett., **98**, 123117 (2011).

[185] Pereiro M, Baldomir D, Botana J, Arias J E, Warda K and Wojtczak L. J. Appl. Phys., **103,** 07A315 (2008).

[186] Peter TC So and Chen Y Dong, Fluorescence Spectrophotometry, DOI: 10.1038/npg.els.000297, (2011).

[187] Phuruangrat A, Thongtem T and Thongtem S, Mater. Lett., **63**, 1562 (2009).

[188] Piao X Q, Horikawa T, Hanzawa H and Machida K, Chem. Lett., **35 (3)**, 334 (2006).

[189] Pierobon P and Cappello G, Adv.Drug Deliv. Rev., **64,** 167, (2012 b).

[190] Pierobon P and Cappello G, Biol. Interact. Nanopart., **64**(2), 167 (2012 a).

[191] Polavarapu L, Manna M and Xu Q H, Nanoscale, **3**, 429 (2011).

[192] Porter A L and Youtie J, J. Nanopart. Res., **11**, 1023 (2009).

[193] Poulose A C, Veeranarayanan S, Aravind A, Nagaoka Y, Yoshida Y, Maekawa T, and Kumar D S, Mater. Express, **2** (2), 94 (2012).

[194] Pradeep T; Nano: The essentials- Understanding Nanoscience and Nanotechnology, Tata McGraw-Hills Publishing Company Ltd, ISBN 0-07-061788-0 (2007).

[195] Pradhan N, Battaglia D M, Liu Y and Peng X, Nano Lett., **7**(2), 312 (2007).

[196] Qu S C, Zhou W H, Liu F Q, Chen N F, Wang Z G, Pan H Y, Yu D P, Appl. Phys. Lett., **80** (19), 3605 (2002).

[197] Rajalakshmi M, Sakunthala T and Arora A K, J. Phys.: Condens. Matter, **9**, 9745 (1997).

[198] Raman C V and Krishna K S, Nature, **121**, 501 (1928).

[199] Ramsden J J, Webber S E and Gratzel M, J. Phy. Chem., **89,** 2740 (1985).

[200] Reddy D A, Murali G, Poornaprakash B, Vijayalakshmi R P and Reddy B K, Sol. State Comm., **152** (7), 596 (2012).

[201] Richter H, Wang Z P and Ley L. Solid State Commun., **39**, 625 (1981).

[202] Rocha U, da Silva C J, Silva W F, Guedes I, Benayas A, Maestro L M, Elias M A, Bovero E, van Veggel F C J M, Sole J A G and Jaque D, *ACS Nano*,7 (**2**), 1188 (2013).

[203] Rosetti R, Ellison J L, Gibson J M and Brus L E, J. Chem. Phys., **80**, 552 (1984).

[204] Rosetti R, Hull R, Gibson J M and Brus L E, J. Chem. Phys., **83,** 1406 (1986).

[205] Rosetti R, Nakahara S and Brus L E, J. Chem. Phys., **79,** 1086 (1983).

[206] Ruan S, Wan J, Fu Y, Han K, Li X, Chen J, Zhang Q, Shen S, He Q and Gao H, Bioconjugate Chem., **25**, 1061 (2014).

[207] Rusu M, Karirinne S, Guina M, Grudinin A B and Okhotnikov O G, Solid State Lasers and Amplifiers, edited by Alphan Sennaroglu, James G. Fujimoto, Clifford Pollock R, Proceedings of SPIE Vol. 5460 (SPIE, Bellingham, WA, 0277, (2004).

[208] Sagadevan S and Janarthanan B, Int. J. Mat. Sci. Appl, **3**(6), 370 (2014).

[209] Sajan P, Bushiri J M and Vinod R, Appl. Phys. A-Mater., **113**, 321 (2013).

[210] Sajan P, Jayasree R S, Agouram S and Junaid Bushiri M, Luminescence, **31**, 544 (2016)

[211] Sajan P, Vinod R and Bushiri M J, J. Lumin., **158**, 110 (2015).

[212] Sajimol A M, Anas A, Das A V, Sreekanth S, Jayalekshmi S, Spectrochim. Acta A., **136**, 327 (2015).

[213] Saleem S S and Aruldhas G, Spectrochimica Acta, **40A**(2), 149 (1984).

[214] Sanderson P, Delgado-Saborit J M and Harrison R M, Atm. Environment, **94**, 353 (2014).

[215] Schroder D K, Semiconductor material and device characterization. Wiley Interscience, New York (1998).

[216] Schwartz R W, Molec. Phys., **30**, 81 (1975).

[217] Scocioreanu M, Baibarac M, Baltog I, Pasuk I and Velula T, J. Solid State Chem., **186**, 217 (2012).

[218] Sebastian J S, PhD thesis, University of Florida, Florida, USA, (1998).

[219] Senna M, Igarashi T, Konishi M and Isobe T, Fourth International Display Workshop, Nogoya, Japan, 613 (1997).

[220] Shadia J and Ikhmayies, Advances in the II-VI Compounds Suitable for Solar Cell Applications, ISBN: 978-81-308-0533-7 (2014).

[221] Sharma M, Singh S and Pandey O P, J. Appl. Phys., **107**, 104319 (2010).

[222] Shenai K, Dudley M and Davis R F, ECS J. Sol. State Sci. and Tech., **2** (8) N3055 (2013).

[223] Shinde K N, Dhoble S J, Swart H C and Park K, Springer Series in Materials Science, **174**, 41 (2012).

[224] Singh V, Sharma P K and Chauhan P, Mater. Chem. and Phy. **121**, 202 (2010).

[225] Sirbuly D J, Tao A, Law M, Fan R and Yang P D, Adv. Mater., **19**, 61 (2007).

[226] Smith A M and Nie S, Acc. Chem. Res., **43**(2) 190 (2010).

[227] Smith A M, Duan H, Mohs A M and Nie S, Adv. Drug Deliv. Rev., **60**(11), 1226 (2008).

[228] Soloviev V N, Eichhofer A, Fenske D and Banin U, J. Am. Chem. Soc., **122** (11), 2673(2000).

[229] Song H Q, Qing D D, Ping X J, Song Z X, Min Z H, and Lan L, Chinese Phys Lett., **27** (5) 057306 (2010).

[230] Song K C, Lee H S, Choung Il Y, Cho K I, Ahn Y and Choi E J. Col. and Sur. A: Physicochem. Eng. Asp., **276,** 162 (2006).

[231] Sookhakian M, Amin Y M and Basirun W J, Appl. Surf. Sci., **283**, 668 (2013).

[232] Stanislaus S W, Adam T W, Teri W O, Jin L H, Philip K, Dimitri V V and Charles M L, Appl. Phys. Lett., **73**, 3465 (1998).

[233] Stapor A, Godlewski M, Przybylinska H and Hommel D, J. Lumin., **40-41**, 625 (1988).

[234] Straumal B B, Mazilkin A A, Protasova S G, Straumal P B, Myatiev A A, Schutz G, Goering E J, Tietze T and Baretzky B, Phil.Mag., **93,** 1371 (2013).

[235] Streetman B G, Solid state electronic devices, Prentice Hall of India Pvt Ltd, New York, (1995).

[236] Subramanian A and Marlcs L D, Ultramicroscopy, **98**, 151 (2004).

[237] Sun L, Liu C, Liao C and Yan C, J. Mater. Chem., **9**, 1655 (1999).

[238] Sun L, Liu T, Qiu Y, Liu J, Shi L and Wolfbeis O S, Microchim. Acta., **181**, 775 (2014).

[239] Sun T M, Wang Y C, Wang F, Du J Z, Mao C Q, Sun C Y, Tang R Z, Liu Y, Zhu J, Zhu Y H, Yang X Z and Wang J, Biomaterials, **35**(2), 836 (2014).

[240] Suresh S; Nanoscience and Nanotechnology, **3**(3), 62 (2013).

[241] Sureshkumar R, Mohideen S T and Nethaji N, Renew. Sust. Energ. Rev., **20**, 397-410 (2013).

[242] Swart H C, Oosthuizen L, Holloway P H and Berning G L P, Surf. Interface. Anal., **26**, 337 (1998 b).

[243] Swart H C, Sebastian J S, Trottier T A, Jones S L and Holloway P H, J. Vac. Sci.Technol., **A 14,** 1697 (1996).

[244] Swart H C, Trottier T A, Sebastian J S, Jones S L and Holloway P H, J. Appl. Phys., **83(9),** 1 (1998 a).

[245] Taghvaei V, Yangjeh A H and Behboudnia M, Physica.E, **42**, 1973(2010).

[246] Tanaka A, Onari S and Arai T, Phys. Rev. B, **45**, 6587 (1992).

[247] Tanaka A, Onari S and Arai T, Phys. Rev. B, **47**, 1237 (1993).

[248] Taylor R, Coulombe S and Otanicar T, Proc. of the 3rd Int. Conf. on Micro/Nanoscale Heat & Mass Transfer, Atlanta, GA, March, Anonymous, 3-6 (2012).

[249] Tian L, Xu Z, Zhao S, Cui Y, Liang Z, Zhang J and Xu X, Materials, **7**, 7289 (2014).

[250] Tran T K , Park W, Tong W, Kyi M M, Wagner B K, and Summers C J, J. Appl. Phys., **81**, 2803(1997).

[251] Tsakalakos T, Balch J, Fronheiser J, Korevaar B A, Sulima O and Rand J. Appl. Phys. Lett., **91**, 233117 (2007).

[252] Ummartyotin S and Infahsaeng Y, Renew.and Sus. Ener. Rev., **55**, 17–24 (2016).

[253] Uzar N and Arikan M C, Bull. Mater. Sci., **34**(2), 287 (2011).

[254] Veprek S and Argon A S. Surface and Coatings Technology, **146**, 175 (2001).

[255] Vij D R, Luminescence of solids Plenum Press NewYork (1998).

[256] Wang C, Hu B, Li W and Yi H, Optik. 125, 554 (2014).

[257] Wang G and Su X, Analyst, **136**, 1783 (2011).

[258] Wang J, Polleux J, Lim J and Dunn B. J. Phys. Chem. C, **111**, 14925 (2007).

[259] Wang L, Huang S and Sun Y, Appl. Surf. Sci., **270**, 178 (2013).

[260] Wang S P, Mamedova N, Kotov N A, Chen W and Studer J, Nano Lett., **2**, 817 (2002).

[261] Wang S, Jarrett B R, Kauzlarich S M and Louie A Y. J. Am. Chem. Soc., **129**(13), 3848 (2007).

[262] Wang X, Shi J, Feng Z, Lia M and Li C, Phys. Chem. Chem. Phys., **13**, 4715 (2011).

[263] Wang Y, Yang X, He T C, Gao Y, Demir H V, Sun X W and Sun H D, Appl. Phys. Lett., **102**, 021917 (2013).

[264] Wang Z W, Daemen L L, Zhao Y S, Zha C S, Downs R T, Wang X D, Wang Z L and Hemley R J, Nat. Mater., **4**, 922 (2005).

[265] Watt M, The principle and practise of electron microscopy, Cam-bridge Uni. Press, Cambridge (1997).

[266] Wei Z, Sun L, Liu J, Zhang J Z, Yang H, Yang Y and Shi L, Biomaterials, **35**, 387 (2014).

[267] Weissleder R, Elizondo G, Wittenburg J, Rabito C A, Bengele H H and Josephson L, Radiology, **175**, 489 (1990).

[268] Weller H, Angew. Chem. Int. Ed. Engl., **32,** 41 (1993).

[269] Weller H, Koch U, Gutierrez M, Henglein A and Bunsenges B. Phys. Chem., **88,** 649 (1984).

[270] Willard D M, Carillo L L, Jung J and Van Orden A, Nano Lett., **1**, 469 (2001).

[271] Willard H H, Instrumental Methods of Analysis, 7th ed. Belmont (1987).

[272] Williams D and Goldstein J, X-ray spectrometry in electron beam instruments, Plenum Press, New York (1995).

[273] Wu Q, Cao H, Zhang S, Zhang X and Rabinovich D, Inorg Chem., **45**, 7316 (2006).

[274] Wyszecki G and Stiles W S, Color Science: concepts and methods, quantitative data andformulae, Second edition, p.131, John Wiley & Sons Inc., New York (1982).

[275] Xia B, Zhang W, Bao W, Dong C, Zhang J and Shi J, Phys. Status Solidi A, **209,** 2247 (2012).

[276] Xing R, Xue Y, Liu X, Liu B, Miao B, Kanga W and Liu S, Cryst. Eng. Comm., **14**, 8044 (2012).

[277] Xu D, Liu Z, Liang J and Qian Y, J. Phys. Chem. B, **109**, 14344 (2005).

[278] Xu J and Ji W, J. Mater. Sci. Lett., **18**,115(1999).

[279] Xu S J, Chua S J, Liu B, Gan L M, Chew C H and Xu G Q, Appl. Phys. Lett., **73** (4), 478 (1998).

[280] Xu Y, Wu J, Sun W, Tao D, Yang L, Song Z, Weng S, Xu Z, Soloway R D, Xu D and Xu G, Chem. Eur. J., **8** (23) (2002).

[281] Xue K, Chen D and Jiao X, Inorg. Chem., **49**, 1191(2010).

[282] Yang C C, Lin C M, Chen Y J, Wu Y T, Chuang S R, Liu R S and Hu S F, Appl. Phys. Lett., **90**, 123503 (2007).

[283] Yang H, Santra S and Holloway P H, J. Nanosci. Nanotech., **5** (9) 1364 (2005),

[284] Yang H, Wang Z, Song L, Zhao M, Chen Y, Dou K, Yu J and Wang L, Mater. Chem. Phys., **47,** 249 (1997).

[285] Yang P, Lu M, Xu D and Zhou G, J. Lumin., **93,** 101 (2001).

[286] Yao W T, Yu S H, Pan L, Li J, Wu Q S, Zhang L and Jiang H, Small, **1**, 320 (2005).

[287] Ye C, Meng G, Wang Y, Jiang Z and Zhang L, J. Phys. Chem. B, **106**, 10338 (2002).

[288] Yen W M, Shionoya S and Yamamoto H, Phosphor Handbook; Yen, W. M., S., Eds.; CRC Press: Boca Raton (1999).

[289] Yim W M and Stofko E J, J. Electrochem. Soc., **119** (3), 381 (1972).

[290] Yoffe A D, Adv. in Phys., **42**(2), 173 (1993).

[291] Yong K T, Roy I, Hu R, Ding H, Cai H, Zhu J, Zhang X, Bergey E J and Prasad P N, Integr. Biol., **2**, 121(2010).

[292] Yonzon C R, Haynes C L, Zhang X Y, Walsh J T and Van Duyne R P, Anal. Chem., **76**, 78 (2004).

[293] Yoshida J and Kobayashi T, J. Magn. Magn. Mater., **194**, 176 (1999).

[294] Yu I, Isobe T and Senna M, J. Phys. Chem. Solids, **57** (4), 373 (1996).

[295] Yu X, Wan J, Shan Y, Chen K and Han X, Chem. Mater., **21**, 4892 (2009).

[296] Yuan G D, Zhang W J, Zhang W F, Fan X, Bello I, Lee C S and Lee S T, Appl. Phys. Lett., **93**, 213102 (2008).

[297] Yuan H J, Xie S S, Liu D F, Yan X Q, Zhou Z P, Ci L J, Wang J X, Gao Y, Song L, Liu L F, Zhou W Y and Wang G, J.Cry.Grow, **258**, 225 (2003).

[298] Yue G H, Yan P X, Yan D, Fan X Y, Wang M X, Qu D M and Liu J Z, Appl. Phys. A, **84**, 409 (2006).

[299] Zagorovsky K and Chan W C, Nat. Mater., **12**(4), 285 (2013).

[300] Zande A M, Huang P Y, Chenet D A, Berkelbach T C, You Y M, Lee G H, Heinz T F, Reichman D R, Muller D A and Hone J C, Nature Mat., **12**, 554 (2013).

[301] Zapien J A, Jiang Y, Meng X M, Chen W, Au F C K, Lifshitz Y and Lee S T, Appl.Phys.Lett., **84**,1189 (2004).

[302] Zhang C, Ma P, Li C, Li G, Huang S, Yang D, Shang M, Kang X and Lin J, J. Mater. Chem., **21**, 717 (2011).

[303] Zhang H and Shen Y, J. Lumin., **40-41**, 401 (1988).

[304] Zhang J Z, World Scientific Publishing Co. Pvt. Ltd., http://www.worldscibooks.com/nanosci/7093.html, (2009).

[305] Zhang Q, Chi W, Zhang W, Lv C and Li J, New. J. Chem., **36**,119 (2012).

[306] Zhang X, Young M A, Lyandres O and Van Duyne R P, J. Am. Chem. Soc. **127**, 4484 (2005).

[307] Zhang X, Zhang Y, Song Y, Wang Z and Yu D, Physica. E, **28**, 1 (2005).

[308] Zhang Y, Gu C, Schwartzberg A M and Zhang J Z, Appl. Phys. Lett. **87**, 123105 (2005).

[309] Zhang Y, Pan C, Zhang Y and He W, Cryst. Res. Technol., **46**, 718 (2011).

[310] Zhao J G and Zhang H H, Superlattice Microst., **51**, 663 (2012).

[311] Zhao Q, Hou L and Huang R, Inorg. Chem. Comm., **6**, 971 (2003).

[312] Zhao Z, Song J, Zheng J and Lian J, Trans. Nonferrous Met. Soc. China, **24**, 1434 (2014).

[313] Zhong S L, Xu R, Zhang L F, Qu W G, Gao G Q, Wu X L and Xu A W, J. Mater. Chem., **21**, 16574 (2011).

[314] Zhu S, Zhang J, Qiao C, Tang S, Li Y, Yuan W, Li B, Tian L, Liu F, Hu R, Gao H, Wei H, Zhang H, Sun H and Yang B, Chem. Commun., **47**, 6858 (2011).

[315] Zhu Y C, Bando Y and Xue D F, Appl. Phys. Lett., **82**, 1769 (2003).

[316] Zhuang Z, Lu X, Peng Q and Li Y, J. Am. Chem. Soc., **132**, 1819 (2010).

[317] Zimmler M A, Bao J, Capasso F, Muller S and Ronning C. Appl. Phys. Lett., **93**, 051101, (2008).

Appl Phys A (2013) 113:321–325
DOI 10.1007/s00339-013-7969-8

Applied Physics A
Materials Science & Processing

RAPID COMMUNICATIONS

Boosted UV emission at 349 nm from mesoporous ZnS

P. Sajan · Junaid M. Bushiri · R. Vinod

Received: 14 June 2013 / Accepted: 4 September 2013 / Published online: 13 September 2013
© Springer-Verlag Berlin Heidelberg 2013

Abstract Relatively oxygen-free mesoporous cubic ZnS particles were synthesised via a facile solvo-hydrothermal route using a water–acetonitrile combination. Boosted UV emission at 349 nm is observed from the ZnS prepared by the solvo-hydrothermal route. The increased intensity of this UV emission is attributed to activation of whispering gallery modes of almost elliptical microstructures made of porous nanostructures.

1 Introduction

Modern technology demands new UV sources especially for scintillation [1], for read heads to reduce data storage space, and for bio-imaging applications [2]. ZnS is a semiconductor material with large exciton binding energy of about 40 meV at room temperature [3]. Among the ZnS grown at different conditions, the cubic sphalerite phase has a band gap of the order of 3.68 eV, which is suitable to fabricate UV sources operating at ambient conditions [4–9]. ZnS is also best suited for biological systems and applications, since it is less toxic as compared to lead and cadmium compounds [10]. Even though there is a great interest in the photoluminescence (PL) properties of one-dimensional (1D) ZnS nanostructures, few studies are available in the literature on possible UV emission at room temperature. The reported UV emissions from ZnS are at 365 [11], 322 [12], 333 [13], 375 [14], 374 [15], and 380 nm [16], and these are have fewer applications in device fabrication because of the feeble emission nature. Enhanced optical properties of ZnS nanocrystals are also obtained by using capping agents and surfactants like trioctylphosphine oxide (TOPO) [17], chitosan [18], trioctylphosphine oxide [19], ethylenediamine, dodecylthiol [20], 1-ethyl-3-methylimidazolium ethyl sulphate [21], and didecyldimethylammonium bromide (DDAB) [22] during the synthesis process. Even though the band-to-band edge emission of ZnS falls in the UV region, the majority of the chemically synthesised ZnS samples exhibit emission in the region 400–450 nm or, with doping, in the region 500–600 nm [23]. This is mainly due to high sensitivity of the 1D ZnS nanostructures' optical properties to the synthetic conditions.

More interestingly, mesoporous materials attained much attention because they possess more active sites with abundant inner spaces and surface area. These materials are likely to have better technological performance and are useful for applications in the fields of nanodevices, catalysts, sensors, medicines, drug delivery, etc. [24, 25]. The synthesis of mesoporous ZnS structures is achieved mostly by using surfactants as well as templates [24]. Xing et al. [25] used polyvinylpyrrolidone (PVP) and Zhang et al. [26] employed ethylene glycol as surfactants for the synthesis of mesoporous ZnS structures. A template-free solvothermal and hydrothermal method is also getting more attractive, because it is a low-cost method for the synthesis of large-scale materials [27]. In the hydrothermal synthesis process, water is used as solvent for reactants. But the presence of OH radicals in the water generally contributes to higher amounts of oxygen- and sulphur-related defects, which results in intense emission in the green and orange regions of the spectrum. So, this in turn will reduce the intensity of band-to-band UV emission.

P. Sajan · J.M. Bushiri (✉) · R. Vinod
Nanofunctional Materials Lab, Department of Physics, Cochin University of Science and Technology, Kochi 682022, Kerala, India
e-mail: junaidbushiri@gmail.com

2 Experimental

2.1 Synthesis

All the chemicals used for the present synthesis were AR grade. In the present work we used a water–acetonitrile solution combination as a solvent for solvo-hydrothermal reaction. ZnS crystals were synthesised by the reaction of zinc acetate, $Zn(CH_3COO)_2{\cdot}2H_2O$ (0.2 M), and Na_2S (1 M). Zinc acetate and Na_2S were taken in separate beakers and dissolved in 40 ml of water–acetonitrile solution (1:1 ratio), each separately. These solutions were allowed to dissolve by constant stirring using a magnetic stirrer for 5 min. Then the two solutions were mixed suddenly, stirred for 1 h, transferred to a Teflon-lined sealed stainless steel autoclave, and heated at 200 °C for a growth time of 12 h. After the heating process, the autoclave was allowed to cool naturally to room temperature. The precipitates were filtered out, washed with distilled water and ethanol, and dried in air atmosphere.

2.2 Characterization

The as-synthesised sample was characterized by a Rigaku D/Max-C X-ray diffractometer using Cu Kα radiation (λ = 1.5418 Å) with a scanning speed of 5°/min in the 2θ range 10–80°. The Raman spectrum of the sample was recorded with a Horiba Jobin Yvon LabRAM HR system with a He–Ne laser (632.8 nm) as the excitation source with a resolution better than 3 cm^{-1}. The morphological characterization and elemental analysis (Scanning Electron Microscopy-Energy Dispersive X-ray Spectroscopy (SEM-EDAX)) of the sample were carried out by a JEOL model JSM-6390LV and a JEOL model JED-2300. The transmission electron microscopy (TEM) images of the sample were recorded with a FEI Tecnai G^2 20 S-TWIN 200 keV transmission electron microscope. The UV-visible spectrum of the sample was recorded with a Jasco V-570 spectrometer in the wavelength range 220–800 nm and the room-temperature photoluminescence (PL) of the sample was recorded by a Horiba Jobin Yvon LabRAM HR system with a He–Cd laser (excitation wavelength 325 nm).

3 Results and discussion

Figure 1 shows the X-ray diffraction pattern recorded from the solvo-hydrothermally prepared ZnS sample. The X-ray diffraction pattern of the sample shows the formation of cubic sphalerite (zinc blende) ZnS phase (JCPDS 05-0566) with lattice constant $a = 5.4060$ Å [28].

Zinc blende structure of ZnS belongs to the T_d (43m) point group [29]. The first-order Raman spectra of zinc blende ZnS have transverse optical (TO) and longitudinal optical (LO) modes, which lie below 1000 cm^{-1} [29]. In the present study we obtained Raman bands (Fig. 2) at 286 and 349 cm^{-1} corresponding to TO and LO zone-center phonons of cubic ZnS [30]. The weak nature of the Raman peak at 286 cm^{-1} confirms the cubic structure of the sample [30]. It is reported that both TO and LO modes of zinc blende structure are allowed for scattering from the (111) face only, TO mode from the (110) face only, and LO mode from the (100) face only [30]. In the X-ray diffraction pattern an intense peak at 27.9° indicates that the sample is highly crystalline and oriented in the (111) plane. In the present case both LO and TO modes contributing to the scattering from the (111) plane are seen, which is in agreement with our X-ray result.

The EDAX spectrum (Fig. 3) of the sample which shows the presence of only sulphur and zinc further supports our X-ray Diffraction (XRD) observation.

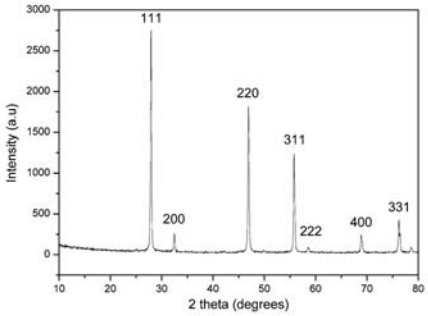

Fig. 1 XRD pattern of solvo-hydrothermally grown mesoporous ZnS at 200 °C

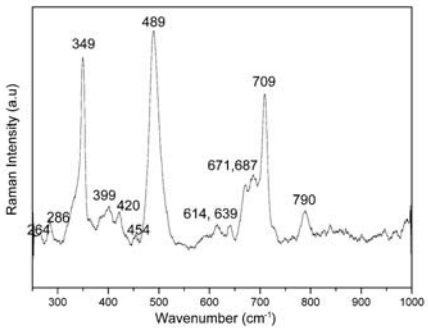

Fig. 2 Raman spectrum of solvo-hydrothermally grown mesoporous ZnS at 200 °C

Figure 4a shows the SEM image of the ZnS sample prepared by using water as solvent and Fig. 4b shows the SEM image of the ZnS sample prepared by using water–acetonitrile (1:1 ratio) as solvent. From the SEM images, one can see that the morphology of the sample is getting spherical in nature and with less agglomeration when the water–acetonitrile combination is used. The particle size distribution histogram (shown in the inset of Fig. 4b) shows that the average particle size is around 265 nm.

Figures 5a, b, and c show the High Resolution Transmission electron microscopy (HRTEM) images of the prepared mesoporous ZnS sample and Fig. 5d depicts its Selected area electron diffraction (SAED) pattern. One can see the porous nature of the as-prepared material from the TEM images with pore size of about 2.4 nm.

Figure 6 shows the UV-visible absorption spectrum recorded from the prepared ZnS sample. The steep absorption edge in the vicinity of 332–370 nm represents the transition between valence and conduction bands usually seen in direct band gap semiconductors like ZnS. Further, the observed absorption shoulder represents the presence of discontinuous energy levels in the band gap [28]. From the absorption spectrum of the sample, a sharp absorption edge is observed at 340 nm, which is the same as reported in bulk ZnS [31]. The band gap of the sample is calculated by using the Kubelka–Munk relation and is found to be 3.64 eV.

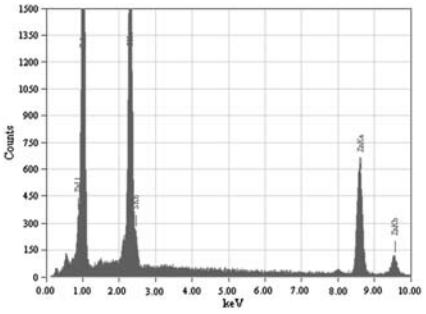

Fig. 3 EDAX spectrum of solvo-hydrothermally grown mesoporous ZnS at 200 °C

Figure 7 depicts the photoluminescence (PL) spectrum recorded from the as-prepared ZnS sample with an excitation wavelength of 325 nm. As reported in the literature, the PL emission in ZnS is contributed by different mechanisms, viz. near-band-edge (NBE) emission in the region 320–370 nm, which is known to originate from band-to-band transitions, or excitonic transitions or the quantum size effect. The violet (390 to 400 nm) emission is attributed to deep levels such as Zn^{2+} vacancies, S^{2-} interstitials, and dislocations. The blue (430–470 nm) emission is associated with the trapped luminescence arising from the Zn^{2+} and S^{2-} vacancies [32]. But the green (510–550 nm) emission is due to the presence of defect levels contributed by dopants or impurity atoms. The PL spectrum shows a highly intense emission peak in the UV region at 349 nm with a feeble shoulder peak at 336 nm and weak and broad profiles at 416 and 523 nm. The weak green emission at 523 nm from the sample under investigation can be associated with the electronic transfer from sulphur vacancies to its interstitial states [33]. The excitonic UV emission at 349 nm in the present sample is not reported so far in any of the ZnS structures. So, the present material has potential application in order to fabricate devices to emit 349 nm UV radiation [10].

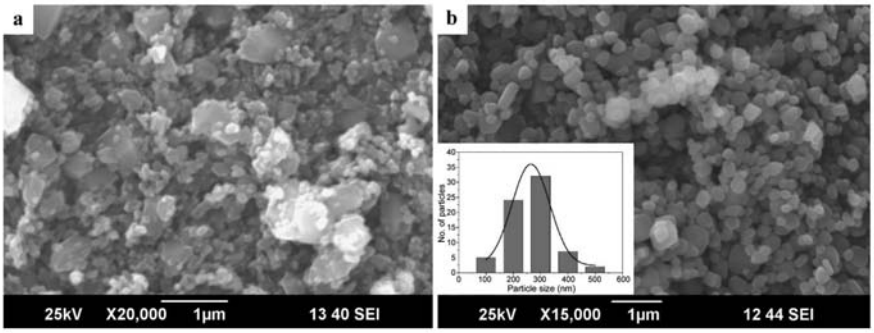

Fig. 4 SEM images of (**a**) hydrothermally grown ZnS, (**b**) solvo-hydrothermally grown mesoporous ZnS at 200 °C (*inset* shows the particle size distribution histogram)

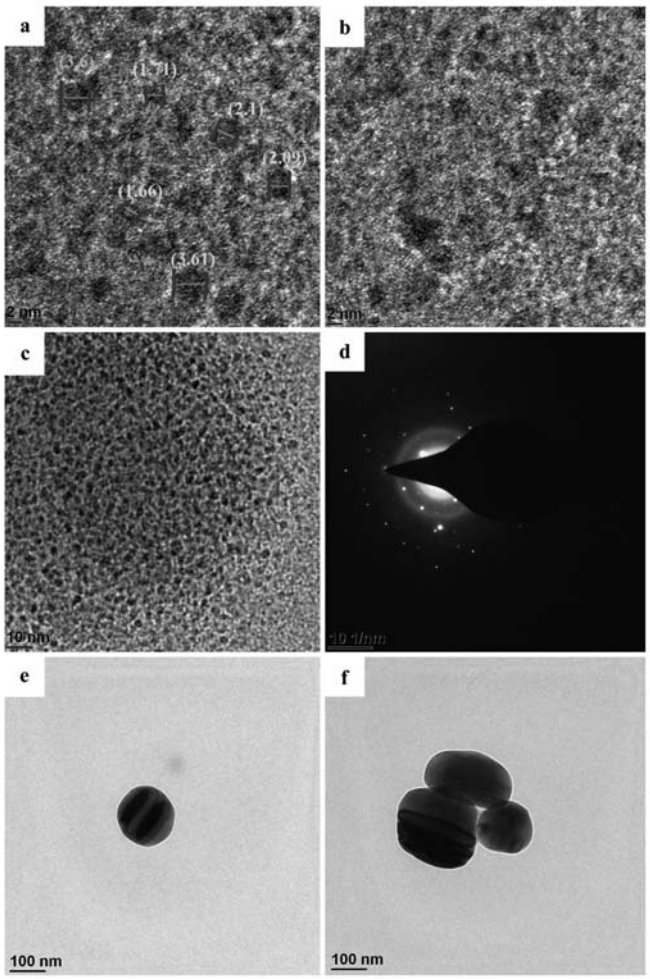

Fig. 5 HRTEM images (**a**), (**b**), and (**c**) corresponds to magnified portion of micro-sized particles (**e**, and **f**), and (**d**) SAED pattern of solvohydrothermally synthesized mesoporous ZnS at 200 °C

4 Conclusions

In summary, we have synthesised almost oxygen-free mesoporous ZnS microspheres with an average pore size of around 2.4 nm. The average particle size is found to be about 265 nm from the histogram plotted based on the size distribution of particles in the SEM image. Our TEM observations with lower-resolution images show that the particles are elliptical in nature having an average diameter of the order of 0.1 to 0.15 μm by considering the dimensions of semi-major and semi-minor axes. These microstructures are made of mesoporous nanoregime structures which can generate UV radiation corresponding to their band gap when this system is suitably pumped by radiation having higher

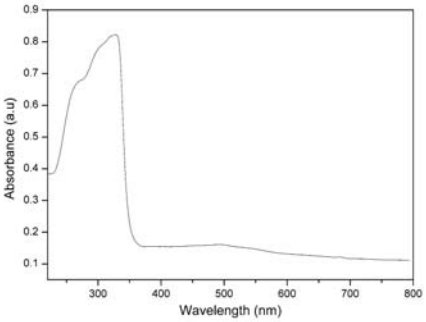

Fig. 6 Room temperature UV-visible absorption spectrum of solvo-hydrothermally synthesised mesoporous ZnS at 200 °C

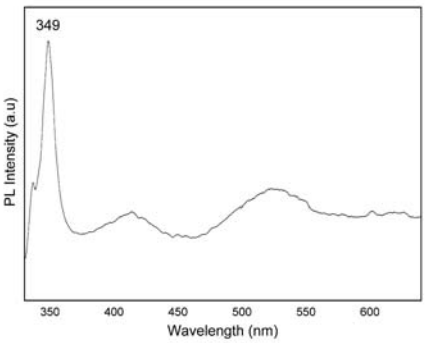

Fig. 7 Room temperature photoluminescence spectrum of mesoporous ZnS grown at 200 °C

frequency. Thus, the generated UV radiation will be amplified by the whispering gallery modes (WGMs) of the elliptical microstructures [34]. So, the unusual enhancement in the UV radiation at 349 nm is partially contributed by WGM activation of the ZnS microstructures. The present material can be used for bio-imaging, in the medical field, as well as in fabricating UV lasers and LEDs. Furthermore, this material is helpful to excite important bio-molecules like nicotinamide adenine dinucleotide (NADH-4, which is an important cell metabolism indicator).

Acknowledgements P. Sajan thanks the University Grants Commission, Government of India, for providing a RGN research fellowship. The authors acknowledge Prof. M.K. Jayaraj, Nanophotonic and Optoelectronic Devices Laboratory, Department of Physics, CUSAT, for providing Raman measurements under the Department of Science and Technology nanomission initiative programme.

References

1. S.R. Choube, S.C. Gedam, S.J. Dhoble, Recent Res. Sci. Technol. **4**(8), 75 (2012)
2. S.K. Mehta, S. Kumar, J. Lumin. **130**, 2377 (2010)
3. T.K. Tran, W. Park, W. Tong, M.M. Kyi, B.K. Wagner, C.J. Summers, J. Appl. Phys. **81**, 2803 (1997)
4. H. Fujiwara, H. Hosokawa, K. Murakoshi, Y. Wada, S. Yanagida, Langmuir **14**, 5154 (1998)
5. H. Li, R. Brescia, R. Krahne, G. Bertoni, M.J.P. Alcocer, C. D'Andrea, F. Scotognella, F. Tassone, M. Zanella, M. De Giorgi, L. Manna, ACS Nano **6**(2), 1637 (2012)
6. J. Xu, W. Ji, J. Mater. Sci. Lett. **18**, 115 (1999)
7. L. Sun, C. Liu, C. Liao, C. Yan, J. Mater. Chem. **9**, 1655 (1999)
8. G.H. Yue, P.X. Yan, D. Yan, X.Y. Fan, M.X. Wang, D.M. Qu, J.Z. Liu, Appl. Phys. A **84**, 409 (2006)
9. J.A. Zapien, Y. Jiang, X.M. Meng, W. Chen, F.C.K. Au, Y. Lifshitz, S.T. Lee, Appl. Phys. Lett. **84**, 1189 (2004)
10. A. Chatterjee, A. Priyam, S.C. Bhattacharya, A. Saha, Colloids Surf. A, Physicochem. Eng. Asp. **297**, 258 (2007)
11. B. Bodo, R. Singha, S.C. Das, Int. J. Appl. Phys. Math. **2**(4), 287 (2012)
12. C. Cheng, G. Xu, H. Zhang, J. Cao, P. Jiao, X. Wang, Mater. Lett. **60**, 3561 (2006)
13. X.M. Meng, J. Liu, Y. Jiang, W.W. Chen, C.S. Lee, I. Bello, S.T. Lee, Chem. Phys. Lett. **382**, 434 (2003)
14. W.S. Chae, J.H. Yoon, H. Yu, D.J. Jang, Y.R. Kim, J. Phys. Chem. B **108**, 31 (2004)
15. H.J. Yuan, S.S. Xie, D.F. Liu, X.Q. Yan, Z.P. Zhou, L.J. Ci, J.X. Wang, Y. Gao, L. Song, L.F. Liu, W.Y. Zhou, G. Wang, J. Cryst. Growth **258**, 225 (2003)
16. J. Li, D. Zhao, X. Meng, Z. Zhang, J. Zhang, D. Shen, Y. Lu, X. Fan, J. Phys. Chem. B **110**, 14685 (2006)
17. M.A. Malik, P. O'Brien, N. Revaprasadu, J. Mater. Chem. **11**, 2382 (2001)
18. M. Sharma, S. Singh, O.P. Pandey, J. Appl. Phys. **107**, 104319 (2010)
19. L. Manna, E.C. Scher, L.S. Li, A.P. Alivisatos, J. Am. Chem. Soc. **124**, 7136 (2002)
20. Q. Zhao, L. Hou, R. Huang, Inorg. Chem. Commun. **6**, 971 (2003)
21. V. Taghvaei, A.H. Yangjeh, M. Behboudnia, Physica E **42**, 1973 (2010)
22. G. Li, J. Zhai, D. Li, X. Fang, H. Jiang, Q. Dong, E. Wang, J. Mater. Chem. **20**, 9215 (2010)
23. X. Zhang, Y. Zhang, Y. Song, Z. Wang, D. Yu, Physica E **28**, 1 (2005)
24. K. Xue, D. Chen, X. Jiao, Inorg. Chem. **49**, 1191 (2010)
25. R. Xing, Y. Xue, X. Liu, B. Liu, B. Miao, W. Kanga, S. Liu, CrystEngComm **14**, 8044 (2012)
26. Q. Zhang, W. Chi, W. Zhang, C. Lv, J. Li, New J. Chem. **36**, 119 (2012)
27. M. Muruganandham, R. Amutha, E. Repo, M. Sillanpaa, Y. Kosumoto, M.A. Al-Mamun, J. Photochem. Photobiol. A, Chem. **216**, 133 (2010)
28. Y. Li, A. Lu, C. Wang, X. Wu, Sol. Energy Mater. Sol. Cells **92**, 953 (2008)
29. Y.C. Cheng, C.Q. Jin, F. Gao, X.L. Wu, W. Zhong, S.H. Li, P.K. Chu, J. Appl. Phys. **106**, 123505 (2009)
30. S.S. Kumar, M.A. Khadar, S.K. Dhara, T.R. Ravindran, K.G.M. Nair, Nucl. Instrum. Methods Phys. Res. B **251**, 435 (2006)
31. L. Peng, Y. Wang, Nanoscale Res. Lett. **5**, 839 (2010)
32. S. Park, C. Jin, H. Kim, C. Hong, C. Lee, J. Lumin. **132**, 231 (2012)
33. X. Wang, J. Shi, Z. Feng, M. Li, C. Li, Phys. Chem. Chem. Phys. **13**, 4715 (2011)
34. K. Okazaki, T. Shimogaki, K. Fusazaki, M. Higashihata, D. Nakamura, N. Koshizaki, T. Okada, Appl. Phys. Lett. **101**, 211105 (2012)

Journal of Luminescence 158 (2015) 110–115

Contents lists available at ScienceDirect

Journal of Luminescence

journal homepage: www.elsevier.com/locate/jlumin

High luminescent yield from Mn doped ZnS at yellow–orange region and 367 nm

P. Sajan, R. Vinod, M. Junaid Bushiri *

Nano Functional Materials Lab Department of Physics, Cochin University of Science and Technology, Kochi, Kerala 682022, India

ARTICLE INFO

Article history:
Received 20 March 2014
Received in revised form
17 September 2014
Accepted 19 September 2014
Available online 30 September 2014

Keywords:
ZnS
Specific area grain boundary
Luminescence
Hydrothermal
Yellow–Orange
Solvo-Hydrothermal

ABSTRACT

Luminescence properties of hydrothermally and solvo-hydrothermally (water–acetonitrile) grown Mn doped ZnS at a reaction temperature of 200 °C is studied. The photoluminescence (PL) emission intensity of solvo-hydrothermally grown Mn doped ZnS shows high luminescence intensity as compared to that of grown by hydrothermal method. ZnS with Mn 3 wt% doping, grown by S-H method exhibit high luminescence yield at yellow–orange region and 367 nm, is contributed to increase of frozen sulphur vacancy population and specific area of grain boundary. The chromaticity coordinates (CIE) of the observed yellow–orange emission from the samples are calculated, which fall in the yellow–orange region.

© 2014 Elsevier B.V. All rights reserved.

1. Introduction

Semiconductor based white light sources attained much attention because of its high luminous efficiency, brightness, low power consumption [1] and environmental safety [2]. Warm white light emitting sources are a new generation product, fabricated by using ultraviolet light emitting diode (UV–LED) chip in the region 350–420 nm coated with blue–green and orange–yellow phosphors. The rare earth based phosphors used for the fabrication of white LEDs (WLEDs) has week red spectral emission. This week emission in turn contribute to high correlated colour temperature ($T_c > 4500$ K) and low colour rendering indexes ($R_a < 80$) which are undesirable [3,4]. On the other hand most of the warm white light emitting phosphors are nitride or oxynitride compounds. It requires inert atmosphere for its production and are costly. Presently WLEDs are commercially fabricated using InGaN blue chips and yellow–orange emitting phosphor combination. Alternatively, ZnS based phosphors like ZnCdS:Ag, Cl (red) [5], ZnS:Cu, Al (green) [6], and ZnS:Ag (blue) [7], etc. with different colours are also used for making warm white light sources and WLEDs. High luminescence efficiency of the material is a pre-requisite in order to get better performing white light sources. ZnS:Mn shows emission in the yellow–orange region [8–11] and its energy bands, luminescence centres can be tuned by changing the doping concentration [12]. Hydrothermally synthesised Mn doped (0.5, 1, 3, 10 and 20 wt%) ZnS shows a 495 nm (blue) and orange emission at 587 nm attributed to the $^4T_1 - {}^6A_1$ transition of Mn [10]. There is a shift in the absorption band edge to longer wavelength and a broad emission at 580 nm is also reported in ZnS doped with Mn [11].

Highly luminescent, non-toxic yellow–orange emitting sources are also important especially for biological labelling, which can replace the presently using labelling materials like ethidium bromide (EtBr). Synthesis condition of the materials is important in relation to its luminescence properties. Recently our group have reported intensity enhancement in the UV emission from ZnS microstructures attributed to the activation of whispering gallery modes (WGMs) when water–acetonitrile combination is used as solvent for the synthesis of ZnS [13]. In the present work, we are reporting the high luminescence yield from the solvo-hydrothermally (water–acetonitrile combination) grown Mn doped ZnS at yellow–orange region and at 367 nm. Further an attempt is made to understand the role of week hydrophobic polar solvent like acetonitrile on luminescence properties of solvo-hydrothermally (S-H) grown Mn doped ZnS nanocrystals.

2. Experimental

2.1. Materials preparation

Manganese (Mn) doped ZnS were synthesised by the reaction of analytical reagent grade (AR grade) zinc acetate (0.4 M), manganese acetate and sodium sulphide (1 M). 3.4065 and 0.1054 g zinc acetate and manganese acetate respectively were

* Corresponding author. Tel.: +91 9495348631.
E-mail address: junaidbushiri@gmail.com (M.J. Bushiri).

http://dx.doi.org/10.1016/j.jlumin.2014.09.041
0022-2313/© 2014 Elsevier B.V. All rights reserved.

used for the synthesis of Mn 3 weight percentage (wt%) doped ZnS. But 3.3713 g zinc acetate and 0.1405 g of manganese acetate were used for the synthesis of Mn 4 wt% doped ZnS. The Mn 5 wt% doped ZnS were made by using 3.3360 g zinc acetate and 0.1756 g of manganese acetate. Whereas the amount of sodium sulphide used for the synthesis of all the compounds described in this communication was 3.1216 g (1 M). For the synthesis, zinc acetate and manganese acetate were taken together in a beaker and made to 40 ml solution using water in hydrothermal or water–acetonitrile combination in S-H synthesis. Sodium sulphide is made to 40 ml solution separately in the same way. These two solutions were stirred separately for 5 min and mixed together, stirred again for 1 h. The resulting solution was kept inside a teflon lined sealed stainless steel autoclave and heated at 200 °C for 12 h [13]. The precipitates obtained from the reaction process were filtered out and washed with distilled water and ethanol. The precipitates were allowed to dry in air atmosphere at room temperature (30 °C) and again warmed by using hot air oven at 60 °C for 1 h. Water–acetonitrile combination (1:1) is used as the solvent for the synthesis of Mn doped ZnS by S-H method.

2.2. Materials characterisation

The X-ray diffraction (XRD) patterns of the prepared Mn doped ZnS (ZnS:Mn) samples were recorded by using a Rigaku Geigerflex D Max diffractometer with CuKα radiation (λ = 1.5414 Å). Morphology of the samples was examined with a JEOL Model JSM-6390LV scanning electron microscope (SEM). The high resolution transmission electron microscopy (HRTEM) images of the samples were recorded by using a JEOL JEM-2100 model transmission electron microscope. The diffused reflectance spectra (DRS) of the samples were taken with JASCO V-570 spectrometer. A Horiba Jobin Yvon Lab Ram HR system was used for the measurement of room temperature photoluminescence (PL) spectra of the samples with a He–Cd laser (excitation wavelength 325 nm).

3. Results and discussion

3.1. XRD analysis of hydrothermally and S-H synthesised Mn doped ZnS

The X-ray diffraction patterns (Fig. 1) of hydrothermally and S-H grown Mn 3, 4 and 5 wt% doped ZnS can be indexed to that of cubic sphalerite ZnS phase with JCPDS 05-0566. The XRD of S-H

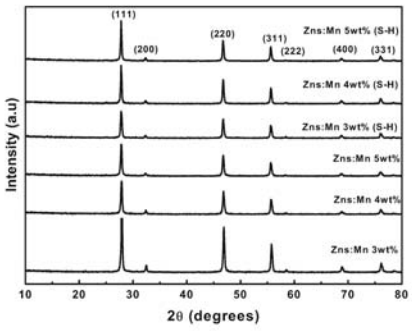

Fig. 1. Room temperature XRD patterns of hydrothermally and S-H synthesised Mn doped (3, 4 and 5 wt%) ZnS at a reaction temperature of 200 °C.

Table 1
Grain size and lattice parameter of the hydrothermally and S-H synthesised ZnS:Mn at a reaction temperature of 200 °C.

Sample (wt%)	Average grain size (nm)	Standard deviations (±) nm	Lattice parameter Å Unit
ZnS:Mn (3)	33	1.27	5.5348
ZnS:Mn (4)	37	1.67	5.5441
ZnS:Mn (5)	41	2.49	5.5530
ZnS:Mn (3 S-H)	26	2.48	5.5535
ZnS:Mn (4 S-H)	31	0.30	5.5558
ZnS:Mn (5 S-H)	34	1.27	5.5575

grown ZnS:Mn is almost identical to that of S-H grown ZnS reported previously [13]. The calculated lattice constants are found to be matching with that of the standard value 5.4060[14]. The lattice parameters (Table 1) of all the samples increases slightly with increase in the Mn doping concentration (wt%).

3.2. SEM analysis of hydrothermally and S-H synthesised Mn doped ZnS

From the SEM images one can see that the morphology of S-H grown Mn doped ZnS are tending to become spherical in nature with less agglomeration unlike its hydrothermally grown counterparts (Fig. 2). The average grain size of the samples are determined from the XRD data using Scherrer equation corresponds to the (1 1 1), (2 2 0) and (3 1 1) planes [12,14]. The particle size and optical properties are expected to change while using different organic solvents for growth process [15]. Similarly, crystal structure of the materials may change due to the influence of interfacial forces while using organic solvents for the synthesis [15]. It is reported that the grain size may increase while increasing the water content in solvo hydrothermal growth with acetonitrile–water combination which is in agreement with our observation [15]. In the present study the grain size of both the hydrothermally and S-H synthesised Mn doped ZnS samples gets increased as Mn doping wt% increases. Interestingly, the grain size of the S-H grown Mn doped ZnS is relatively less than that of hydrothermally grown Mn doped ZnS with the identical doping concentrations (Table 1). In order to know the actual size of the samples, the HRTEM images (Fig. 3) of the representative samples are taken and are in agreement with the values given in Table 1.

3.3. DRS study of hydrothermally and S-H synthesised Mn doped ZnS

Fig. 4 depicts the room temperature absorption spectra of hydrothermally and S-H synthesised Mn doped (3, 4 and 5 wt%) ZnS grown at a reaction temperature of 200 °C and the observed absorption edge is given in Table 2. There is no appreciable change in the absorption edge and optical band gap of all the samples under investigation and S-H grown ZnS reported by our group [13].

Fig. 5 shows the $[(k/s)h\nu]^2$ versus $h\nu$ plot by using Kubelka–Munk function of the hydrothermally and S-H synthesised Mn doped (3, 4 and 5 wt%) ZnS [10]. It is found that the band gap of hydrothermally and S-H grown ZnS:Mn (3, 4 and 5 wt%) are blue shifted from the bulk ZnS (3.65 eV) [16] and its values are slightly decreased with increase in doping concentration (Table 2).

3.4. Photoluminescence analysis of hydrothermally and S-H synthesised Mn doped ZnS

Room temperature PL spectrum of S-H and hydrothermally synthesised Mn doped (3, 4 and 5 wt%) ZnS samples are shown in Fig. 6. The PL emission spectra of the solvo-hydrothermally grown ZnS:Mn shows higher luminescence intensity as compared to that

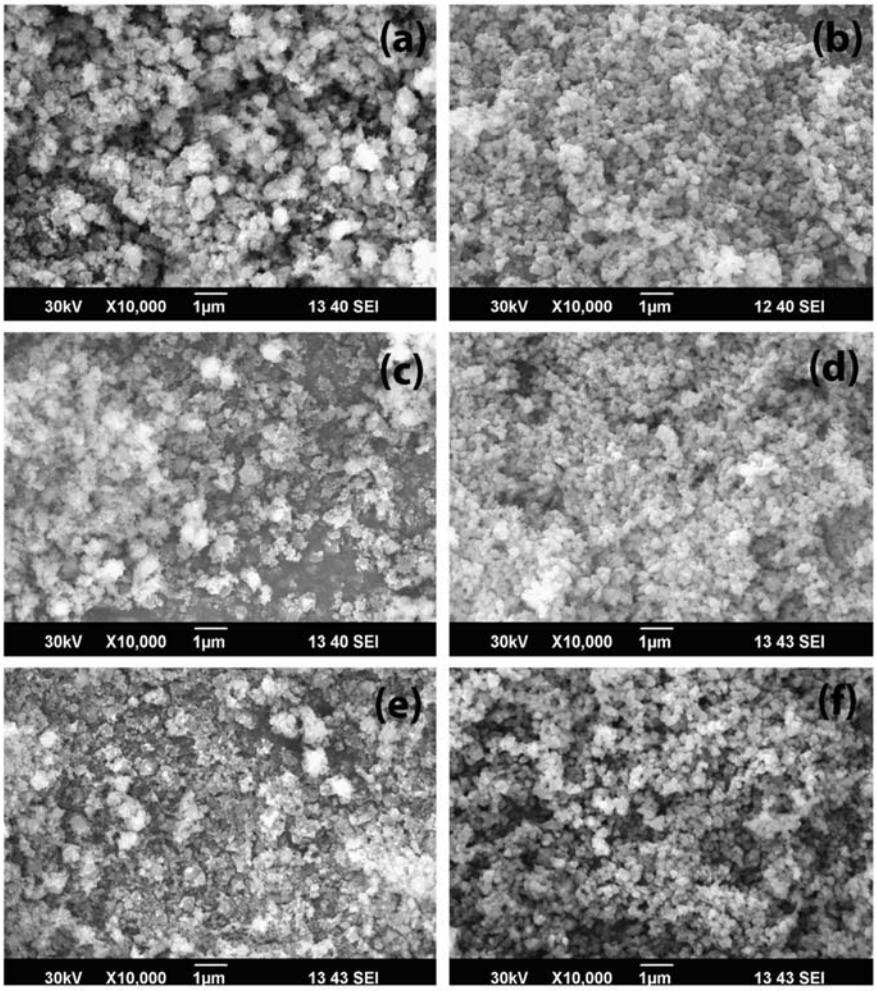

Fig. 2. SEM images of hydrothermally (a) 3 wt%, (c) 4 wt%, (e) 5 wt% and S-H synthesised (b) 3 wt%, (d) 4 wt%, (f) 5 wt% Mn doped ZnS at a reaction temperature of 200 °C.

of grown by hydrothermal method. The hydrothermally grown Mn:ZnS samples shows an emission band at 600 nm similar to previously reported one [17]. The S-H grown ZnS samples with Mn 3 and 4 wt% doping shows emission at 602 nm while 5 wt% ZnS: Mn shows band at 600 nm. Apart from this the 3 wt% S-H grown Mn doped ZnS shows a strong UV band at 367 nm. Similarly 5 wt% S-H grown Mn doped ZnS have a UV emission at 376 nm. But the UV emission is absent in the case of 4 wt% S-H grown Mn doped ZnS. The near-band edge (NBE) emission in the UV region can be attributed to the band-to band, or excitonic transition or quantum size effect [18]. The emission at 600 nm may be arising from the $_4T_1 - _6A_1$ transition of Mn^{2+} ions [19]. The defect related emission (trap state blue emission) usually seen in ZnS is absent in the samples under investigation. The solubility of sulphur, manganese, and zinc in organic solvents like acetonitrile is a major factor which determines the luminescence property of the materials like ZnS [15]. In the present case, the solubility of sulphur in acetonitrile is more as compared to that of zinc, which contributed to the formation of frozen sulphur vacancies (Vs), and increase in population of frozen sulphur vacancy state Vs. On exciting the sample with energy of 3.83 eV (325 nm), the electrons are pumped to the conduction band and these electrons may be trapped in

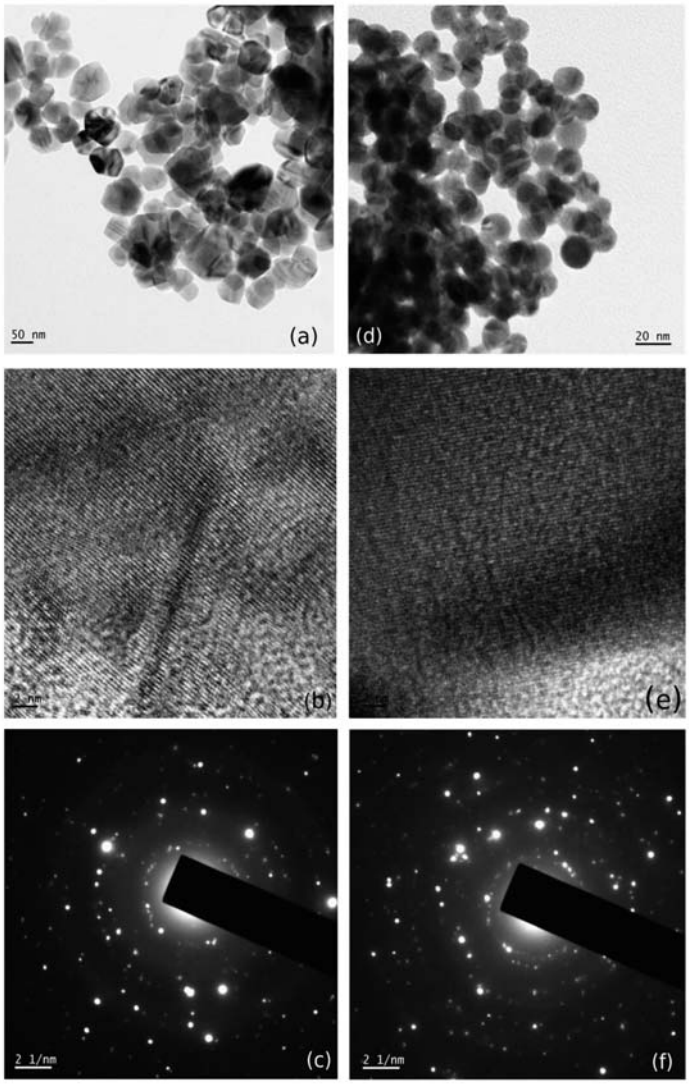

Fig. 3. HRTEM images of hydrothermally (a, b) and S-H synthesised at 200 °C (d, e) 3 wt% Mn doped ZnS. The SAED patterns of hydrothermally (c) and S-H synthesised (f) 3 wt% Mn doped ZnS at a reaction temperature of 200 °C.

shallow traps formed by Vs. From this level, the electrons reaches to the upper energy level of Mn^{2+} ($_4T_1$) by a non-radiative transition [17]. As a result of this transition the population at $_4T_1$ level of Mn^{2+} increases. These carriers cannot stay for a long time at that level and radiate to lower level Mn^{2+} ($_6A_1$) with yellow–orange emission as reported previously [17]. The enhanced intensity in Mn 3 wt% doped S-H grown ZnS is due to the increase in population of frozen sulphur vacancies contributed to high solubility of sulphur in acetonitrile [15]. The rate of non-radiative transition from the shallow traps (formed by sulphur vacancy) to

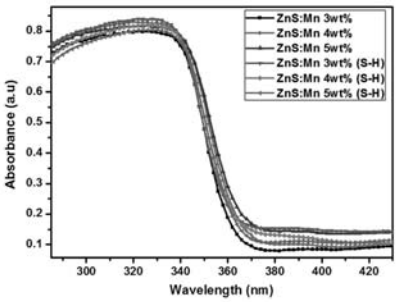

Fig. 4. The room temperature UV–vis absorption spectra of hydrothermally and S-H synthesised Mn doped (3, 4 and 5 wt%) ZnS at a reaction temperature of 200 °C.

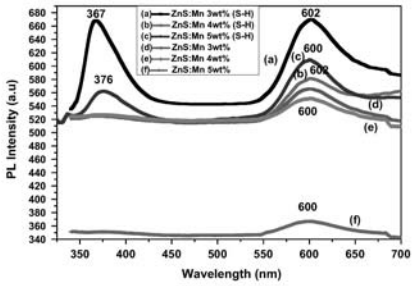

Fig. 6. Room temperature PL spectra of hydrothermally (d, e and f) and S-H synthesised (a, b and c) Mn doped (3, 4 and 5 wt%) ZnS at a reaction temperature of 200 °C.

Table 2
Absorption edge and the band gap of the hydrothermally and S-H synthesised Mn doped ZnS with different doping concentrations (3, 4 and 5 wt%).

Sample (wt%)	Absorption edge wavelength region (nm)	Band gap (eV)
ZnS:Mn (3)	(330–370)	3.53
ZnS:Mn (4)	(330–370)	3.52
ZnS:Mn (5)	(325–375)	3.50
ZnS:Mn (3 S-H)	(330–365)	3.54
ZnS:Mn (4 S-H)	(330–370)	3.53
ZnS:Mn (5 S-H)	(330–370)	3.525

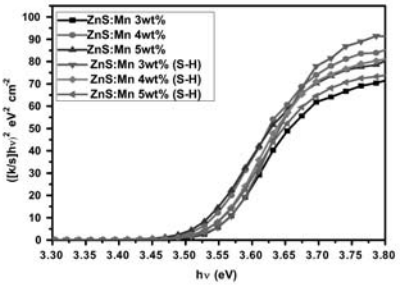

Fig. 5. $[(k/s)h\nu]^2$ versus $h\nu$ plot of hydrothermally and S-H synthesised Mn doped (3,4 and 5 wt%) ZnS at a reaction temperature of 200 °C.

the ${}_4T_1$ level of Mn^{2+} and recombination of electrons from shallow traps with the holes in the ground states are almost equal leading to the dual wavelength emission at UV and orange–yellow region with the same intensity [17]. The observed PL intensity reduction for the higher Mn doping concentrations attributed to the quenching effect by the Mn ions pairing or coagulation [10]. Moreover the presences of organic solvents cause surface passivation and which may also leads to photoluminescence intensity enhancement [20]. The CIE chromaticity coordinates, of the observed yellow–orange emission from the samples are calculated and is in the yellow–orange region (Table 3).

The specific area of grain boundary (s_{GB}) of a material has significant role in its physical and optical properties [21]. The s_{GB} of S-H ZnS:Mn samples were calculated from the SEM images using

Table 3
CIE colour coordinates of the hydrothermally and S-H synthesised Mn doped ZnS with different doping concentrations (3, 4 and 5 wt%).

Sample (wt%)	CIE Coordinate
ZnS:Mn (3)	(0.466, 0.511)
ZnS:Mn (4)	(0.464, 0.513)
ZnS:Mn (5)	(0.464, 0.513)
ZnS:Mn (3 S-H)	(0.475, 0.504)
ZnS:Mn (4 S-H)	(0.469, 0.509)
ZnS:Mn (5 S-H)	(0.470, 0.508)

the formula for the flattened grains.

$$s_{GB} = 1.65\,\mathbf{a}/\mathbf{D},$$

where '**a**' is the ratio of grain width to grain height and '**D**' is the mean grain width [21]. It shows values of 9.598×10^6 m^2/m^3 (3 wt%), 7.578×10^6 m^2/m^3 (4 wt%), and 7.99×10^6 m^2/m^3 (5 wt%) for S-H synthesised ZnS:Mn samples. The s_{GB} values of hydrothermally grown ZnS:Mn samples are not calculated because of the agglomerated nature of the grains. The increase in s_{GB} value indicates the presence of more grain boundary specific area and the grain boundary angle [22]. There will be the possibility to have large amount of defect states in the grain boundary region, which become charged after trapping free carriers from neighbouring grains [23]. So the increase in specific area of grain boundary of a material will leads to the increase in population of carriers [23], and these carriers will participate in transition between different energy levels and will boost the intensity enhancement in the PL spectrum. The enhanced luminescence efficiency observed in the Mn 3 wt% ZnS:Mn is contributed to the increase in specific area of grain boundary (9.598×10^6 m^2/m^3) as compared to 4 wt% (7.578×10^6 m^2/m^3), and 5 wt% (7.99×10^6 m^2/m^3) of ZnS:Mn. In case of 4 wt% ZnS:Mn, UV emission is decreased because of the reduction in population of Vs contributed to decrease in s_{GB}. Further there is a possibility to have more Mn ions in S-H grown systems which contribute to increase in s_{GB} and in turn increase the luminescence intensity [23]. The organic solvents used for the synthesis of nanocrystal materials contribute to the formation of ion-pair which in turn enhance the PL intensity of the as synthesised samples [24,25].

4. Conclusions

The PL emissions of the ZnS doped with 3 and 5 wt% of Mn, synthesised by S-H method are having intense dual wavelength

emission at UV and yellow–orange region. ZnS with Mn 3 wt% exhibit higher luminescence yield at 367 nm and yellow–orange region. The increase in luminescence yield of S-H grown sample with Mn 3 wt% doping is attributed to the increase in population of frozen sulphur vacancies formed due to the higher solubility of the sulphur in acetonitrile and the increase in specific area of grain boundary. Water–acetonitrile combination is a suitable solvent for the production of better luminescent Mn doped ZnS. The high luminescence yield at 367 nm and in the yellow–orange region from the sample is useful to fabricate white light sources and also for bio-imaging.

Acknowledgements

P. Sajan thanks University Grants Commission, Government of India, for providing Rajiv Gandhi National fellowship. The author acknowledges Professor M. K. Jayaraj, Nanophotonic and Optoelectronic Devices Laboratory, Department of Physics, CUSAT, for providing photoluminescence measurement facility under Department of Science and Technology nano mission initiative programme.

References

[1] X. Lu, J. Yang, Y. Fu, Q. Liu, B. Qi, C. Lu, Z. Su, Nanotechnology 21 (2010) 115702.
[2] G.R. Dillip, S.J. Dhoble, B. Deva Prasad Raju, Opt. Mater. 35 (2013) 2261.
[3] N. Guo, W. Lu, Y. Jia, W. Lv, Q. Zhao, H. You, ChemPhysChem 14 (2013) 192.
[4] G.R. Dillip, K Mallikarjuna, S.J Dhoble, B. Deva Prasad Raju, J. Phys. Chem. Solids 75 (2014) 8.
[5] Y.D. Huh, J.Y. Park, S.S Kweon, J.H. Kim, J.G. Kim, Y.R. Do, B Korean Chem. Soc. 25 (2004) 1585.
[6] C.C. Kao, Y.C. Liu, Mater. Chem. Phys. 115 (2009) 463.
[7] K. Kajiwara, T. Hida, K. Tanaka, J. Vac. Sci. Technol. B 21 (2003) 515.
[8] M.G. Moritz, H. Piotrowska, M. Murias, L. Balan, M. Moritz, J. Lulek, R. Schneider, J. Mater. Chem. B 1 (2013) 698.
[9] H. Labiadh, T.B. Chaabane, D. Piatkowski, S. Mackowski, J. Lalevée, J. Ghanbaja, F. Aldeek, R. Schneider, Mater. Chem. Phys. 140 (2013) 674.
[10] T.T.Q. Hoa, N.D. The, S. McVitie, N.H. Nam, L.V. Vu, T.D. Canh, N.N. Long, Opt. Mater. 33 (2011) 308.
[11] Y. Huang, Y. Cai, H. Liu, Particuology 9 (2011) 533.
[12] X. Ma, J. Song, Z. Yu, Thin Solid Films 519 (2011) 5043.
[13] P. Sajan, Junaid M. Bushiri, R. Vinod, Appl. Phys. A-Mater. 113 (2013) 321.
[14] Y. Li, A. Lu, C. Wang, X. Wu, Sol. Energ. Mat. Sol. C 92 (2008) 953.
[15] J.J. Ramsden, S.E. Webber, M. Gratzel, J. Phys. Chem. 89 (1985) 2740.
[16] A.L. Donne, S.K. Jana, S. Banerjee, S. Basu, S. Binetti, J. Appl. Phys. 113 (2013) 014903.
[17] A.K. Kole, C.S. Tiwary, P. Kumbhakar, J. Appl. Phys. 113 (2013) 114308.
[18] S. Park, C. Jin, H Kim, C. Hong, C. Lee, J. Lumin. 132 (2012) 231.
[19] G. Murugadoss, V. Ramasami, Luminescence 28 (2013) 69.
[20] K.C. Song, H.S. Lee, I.Y. Choung, K.I. Cho, Y. Ahn, E.J. Choi, Colloid Surface A: Physicochem. Eng. Aspects 276 (2006) 162.
[21] B.B. Straumal, A.A. Mazilkin, S.G. Protasova, P.B. Straumal, A.A. Myatiev, G. Schutz, E.J. Goering, T. Tietze, B. Baretzky, Philos. Mag. 93 (2013) 1371.
[22] A.M. Zande, P.Y. Huang, D.A. Chenet, T.C. Berkelbach, Y.M. You, G.H. Lee, T. F. Heinz, D.R. Reichman, D.A. Muller, J.C. Hone, Nat. Mater. 12 (2013) 554.
[23] D. Ghosh, S. Hussain, B. Ghosh, R. Bhar and A.K. Pal, ISRN Mat.Sci. (2014), Article ID 521701, http://dx.doi.org/10.1155/2014/521701.
[24] H. Katano, K. Uematsu, T. Tsukatani, Anal. Sci. 27 (2011) 1249.
[25] B. Xia, W. Zhang, W. Bao, C. Dong, J. Zhang, J. Shi, Phys. Status Solidi A 209 (2012) 2247.

Research article

LUMINESCENCE
The Journal of Biological and Chemical Luminescence

Received: 10 March 2015, Revised: 2 July 2015, Accepted: 6 July 2015 Published online in Wiley Online Library: 17 August 2015

(wileyonlinelibrary.com) DOI 10.1002/bio.2993

Synthesis of cubic ZnS microspheres exhibiting broad visible emission for bioimaging applications

P. Sajan,[a] R. S. Jayasree,[b] S. Agouram[c] and M. Junaid Bushiri[a]*

ABSTRACT: Biocompatible ZnS microspheres with an average diameter of 3.85 μm were grown by solvo-hydrothermal (S-H) method using water–acetonitrile–ethylenediamine (EDA) solution combination. ZnS microspheres were characterized by X-ray diffraction (XRD), scanning electron microscopy (SEM), high-resolution transmission electron microscopy (HRTEM), Fourier transform (FT)-Raman spectroscopy and Fourier transform infrared spectroscopy (FTIR) techniques. The broad photoluminescence (PL) emissions from 380–580 nm that were seen from the ZnS microspheres attributed to the increase in carrier concentration, as understood from the observed intense Raman band at 257 cm^{-1}. Cytotoxicity and haemocompatibility investigations of these ZnS microspheres revealed its biocompatibility. ZnS microspheres, along with biological cell lines, were giving visible light emission and could be used for bioimaging applications. Copyright © 2015 John Wiley & Sons, Ltd.

Keywords: ZnS microspheres; broad visible emission; bioimaging; cytotoxicity; haemocompatibility; luminescence

Introduction

ZnS is an important semiconductor material with a band gap of 3.7 eV at room temperature (1). ZnS nanostructures with morphologies such as needles, rods, sheets, micro- and nanospheres, belts etc. were synthesised with a chemical method using surfactants or templates (2). Recently, semiconductor microspheres have obtained much more attention because of their potential applications in the fields of drug targeting, bio-separation, diagnostic analysis and for light-emitting devices (3). The synthesis of ZnS hollow microspheres (4–6), monodispersed wurtzite-type ZnS microspheres (7), mesoporous ZnS with tunable pore size and surface area (8), hierarchical mesoporous ZnS–RGO composite (2), and wurtzite ZnS hierarchical microspheres by the hydrothermal method (9) etc. have been reported in the literature. Phosphors with less toxicity and possessing high luminescent quantum yield are technologically important for use in electroluminescent devices, light-emitting devices (10), and displays etc. (11). White light-emitting phosphor-based light-emitting diodes (LEDs) have advantages such as a long life time, and energy conservation etc. (12–15). Moreover, improving the efficiency of white light sources is a challenging research problem (15). At this time, white light emission is achieved by mixing primary coloured monochromatic sources or using phosphors that convert light into a combination of red, green and blue (RGB; upconversion method) or by yellow and blue phosphors (15–17). The aforesaid white light sources are unstable and exhibit weak emission. In this context, the choice of a single phosphor emitting a white light is an important one in order to get better luminescent quantum yields. Organic material such as the oxadiazole–carbazole copolymer (POC) and semiconductor quantum dot InP/ZnS also exhibit white emission (18). In addition, rare earth-based materials such as Dy^{3+} ion-doped Gd_2O_3 nanophosphors (11), ceria nanophosphors (15), and $BaYF_5$:Ln^{3+} (Ln = Yb, Er, Tm) nanocrystals (19) etc. also exhibit white emission. White light emission from a bio-friendly and relatively cost-effective material such as ZnS is promising for future technology requirements and is the least reported option in the literature. Lu *et al.* reported white emission from Mn^{2+}-doped ZnS by surface chelating of 8-hydroxyquinoline-5-sulfonic acid with the CIE colour coordinates (0.35, 0.34) (20), terbium-based infinite coordination polymer hollow microspheres are also good bio-friendly white emitting sources (4). Wang *et al.* obtained white emission by combining green and blue emission from biocompatible ZnS with the red emission from porous silicon (21). Semiconductor (22), as well as rare earth-based, materials are reported to exhibit upconversion (23–27) of infra-red (IR) wavelengths to visible or UV emission and are suitable for biological imaging. Semiconductors such as CuSe, CdSe, and carbon-based nanophosphors, etc. can also be used for bioimaging applications (28–31). Heavy metal-free, biocompatible, highly luminescent and non-toxic semiconductors that have

* Correspondence to: M. Junaid Bushiri, Nano Functional Materials Laboratory Department of Physics, Cochin University of Science and Technology, Kochi, Kerala-682022, India. E-mail: junaidbushiri@gmail.com

[a] Nano Functional Materials Laboratory, Department of Physics, Cochin University of Science and Technology, Kochi, Kerala, 682022, India

[b] Biophotonics and Imaging Laboratory, Biomedical Technology Wing, Sree Chitra Tirunal Institute for Medical Sciences & Technology, Poojappura, Thiruvananthapuram 695012, Kerala, India

[c] Departamento de Fisica Aplicada y Electromagnetismo, Universitat de, Valencia, C/Dr Moliner 50 Burjassot, Valencia 46100, Spain

Abbreviations: DRS, diffused reflectance spectrum; EPR, enhanced permeability and retention; FTIR, Fourier transform infrared spectroscopy; HRTEM, high-resolution transmission electron microscopy; PL, photoluminescence; RBC, red blood cell; SAED, selected area electron diffraction; SEM, scanning electron microscope; TEM, transmission electron microscope; WBC, white blood cell; XRD, X-ray diffraction.

Copyright © 2015 John Wiley & Sons, Ltd.

LUMINESCENCE
The Journal of Biological and Chemical Luminescence

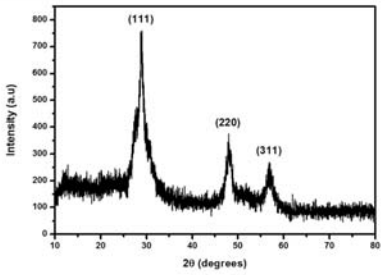

Figure 1. XRD pattern of ethylenediamine assisted solvo-hydrothermally grown ZnS microspheres synthesised at a growth temperature of 180°C.

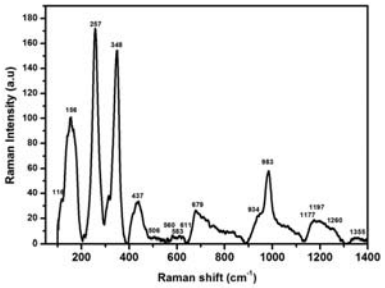

Figure 2. Raman spectrum of ethylenediamine assisted solvo-hydrothermally grown ZnS microspheres synthesised at 180°C.

emission in the region 600–950 nm, however, are much effective for *in vivo* and *in vitro* imaging purposes (22).

To the best of our knowledge, broad emission (380–580 nm) from the cubic phase of biocompatible ZnS microspheres has not reported previously. In the present paper, we are report the synthesis of zinc sulphide (ZnS) microspheres by the facile solvo-hydrothermal (S-H) method and their emission properties. Further, their cytocompatibility, haemocompatibility and *in vitro* bioimaging properties were also investigated.

Experimental

Material preparation

ZnS microspheres were synthesised using AR grade zinc acetate and thiourea along with a water–acetonitrile–ethylenediamine (EDA) solution combination as solvent (S-H method). Next, 0.4 M zinc acetate and 0.8 M thiourea were dissolved in 40 mL solvent (18 mL water + 18 mL acetonitrile + 4 mL EDA) each separately and stirred for 5 min using a magnetic stirrer. Then the two solutions were mixed together rapidly and stirred again for 5 min. These solutions were transferred to a teflon beaker, kept in an autoclave made of stainless steel and sealed. The above chemical reaction system was heated at 180°C for a reaction time of 12 h. After the heating process, the reaction system was allowed to cool naturally. The precipitates were filtered out and washed with water and ethanol. The resulting powder was warmed at 60°C for 1 h in an air atmosphere.

Material characterization

The as-synthesised sample was characterized using a Rigaku D/Max-C X-ray diffractometer and CuKα radiation (λ =1.5418 Å) in the 2θ range 10–80°. A Horiba Jobin Yvon LabRAM HR system (resolution in the order of 3 cm^{-1}) equipped a He–Ne laser (632.8 nm) was used to record the Raman spectrum of the sample. The Fourier transform infrared spectrum (FTIR) of the sample was recorded on a SHIMADZU IR Affinity-1 FTIR spectrophotometer using the KBr pellet technique with a resolution of 4 cm^{-1}. A JEOL model JSM-6390LV scanning electron microscope (SEM) was used for the morphological analysis. The transmission electron microscopy (TEM) images of the sample were taken with a FEI TECNAI G2 F20 transmission electron microscope attached to a selected area electron diffraction (SAED) system. The diffused reflectance spectrum (DRS) and absorbance of the sample were recorded using a JASCO V-570 UV–Vis–NIR spectrometer in the wavelength range 220–800 nm. The room temperature photoluminescence measurement of the sample was done with a Horiba Jobin Yvon LabRAM HR system using a He–Cd laser with an excitation wavelength of 325 nm. The bio-fluorescence images were recorded using a XENOGEN-IVIS spectrum. L929 fibroblast cell lines were used for *in vitro* imaging analysis of the samples.

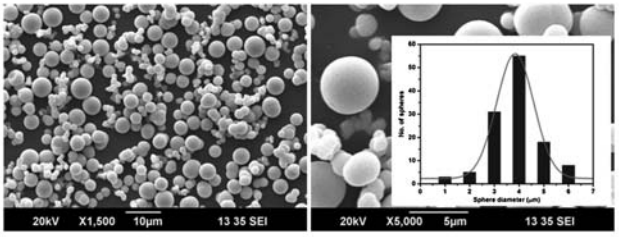

Figure 3. SEM images of ethylenediamine assisted solvo-hydrothermally grown ZnS microspheres synthesised at 180°C. Left panel: scale 10 μm. Right panel: scale 5 μm. Inset: Histogram based on SEM images.

 Copyright © 2015 John Wiley & Sons, Ltd.

LUMINESCENCE
The Journal of Biological and Chemical Luminescence

Results and discussion

Figure 1 depicts the XRD patterns of the solvo-hydrothermally grown ZnS microspheres synthesised at 180°C. The XRD pattern matched that of cubic sphalerite ZnS (JCPDS no. 05–0566). The lattice constant calculated using XRD data is '*a*' = 5.3602 Å, which is comparable with that of the reported value.

Scocioreanu *et al.* reported Raman bands of cubic ZnS at 266, 349, 430 and 653 cm^{-1} (32). The present sample also gives Raman bands at 257, 348, 437 and 679 cm^{-1}, which indicates the formation of the cubic phase of ZnS in agreement with our XRD results (Fig. 2). The Raman peak observed at 156 cm^{-1} can be assigned to the disorder activated mode (32). The Raman bands at 257 and 348 cm^{-1} correspond to the transverse (TO) and longitudinal (LO) zone centre phonons of (111) plane scattered cubic ZnS (33) and also the band at 257 cm^{-1} LO phonon–plasmon coupled modes as reported by Kumar *et al.* (33). The cubic nature of the as-prepared sample was confirmed from the XRD pattern as well as from the absence of a Raman peak at 286 cm^{-1} (33). The presence of a highly intense LO phonon–plasmon coupled mode (LOPC-L^-) Raman band at 257 cm^{-1} is attributed to the increase in carrier concentration (33) in S-H grown ZnS as compared with previous reports (34,35).

Figure 3 shows the SEM images of the solvo-hydrothermally grown ZnS microsphere synthesised at 180°C. The microsphere diameter distribution histogram based on SEM images (inset of Fig. 3) shows that the size distribution was not uniform, and varied from 1–6 μm. These microspheres had an average diameter of 3.85 μm. These XRD data gave broad diffraction peaks and its corresponding grain size, calculated using the Scherrer formulae, gave a value of about 10 nm. This result indicates that these microspheres are made of nanoregime particles and are similar to that of solvo-hydrothermally grown ZnS reported previously (35).

The HRTEM image (Fig. 4a) of the present sample shows its average size to be about 10 nm. The appearance of concentric rings in the SAED pattern (Fig. 4 b) suggested that the material is made of nanoregime particles, which confirms with the size of the particle (about 10 nm) calculated using XRD data. These observations clearly reveal that the smooth microspheres with an average diameter of 3.85 μm are made of hyperfine nanoparticles that have dimensions of about 10 nm.

The S-H grown ZnS in the presence of surfactant ethylenediamine exhibits a regular smooth surface morphology as compared with that grown without ethylenediamine. The chemical reaction of the present experiment is complex because of the involvement of organic solvents such as acetonitrile and the growth-directing surfactant ethylenediamine. The solvent acetonitrile used in the growth system reacts with water at higher temperatures to produce ammonia. Apart from this reaction, the decomposition of thiourea at higher temperatures will also generate ammonia as per the reaction:

$$(NH_2)_2CS \rightarrow H_2S + NH_2CN \quad (1)$$

and at higher temperatures NH_2CN reacts with water to form ammonia and CO_2 (36).

$$NH_2CN + 2H_2O \rightarrow 2NH_3 + CO_2 \quad (2)$$

So the NH_3 concentration inside the growth system is likely to increase and, as a consequence, the pH of the system may increase. As growth is carried out inside a closed system, the production of volatile gases such as ammonia will generate a comparatively higher pressure, consequently the experimental system may have higher energy. Initially, nanoparticles of ZnS are formed and these nanoparticles act as nucleation centres for the larger sized crystallites. The adjacent particles segregate to form spherical structures in order to maintain a low interfacial energy. The spherical nature of the particles is due to the surface tension at higher temperatures (36). The shape and morphology of grains also depend on the interfacial energy of the system (37). A spherical shape has the minimum interfacial energy and has the tendency to form spherical grains (38). Ethylenediamine favours the formation of spherical particles, as reported by Darius *et al.* (39). The new grains try to accumulate and form clusters in order to minimize the interfacial energy. Furthermore, the closely lying nanograins segregate together and attain a spherical morphology. This process accelerates the growth of microcrystals. From the SEM micrograph, smaller spherical structures with diameters in the range 1–6 μm can be seen. This observation suggests that the microspheres are formed due to clustering of smaller grains and are attributed to surface tension.

The absence of organic components in the prepared ZnS microspheres is confirmed from the FTIR spectrum (Fig. 5) and bands seen at 451, 640, and 1220 cm^{-1} that correspond to Zn–S vibration (40).

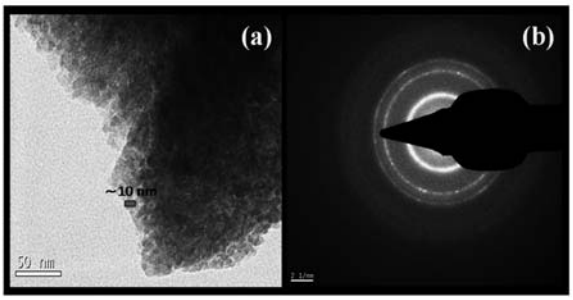

Figure 4. HRTEM image (a) and the SAED pattern (b) of ethylenediamine assisted solvo-hydrothermally grown ZnS microspheres synthesised at 180°C.

 Copyright © 2015 John Wiley & Sons, Ltd.

LUMINESCENCE
The Journal of Biological and Chemical Luminescence

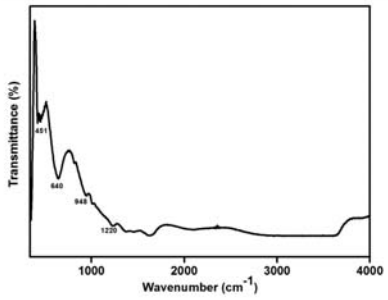

Figure 5. FTIR spectrum of ethylenediamine assisted solvo-hydrothermally grown ZnS microspheres synthesised at 180°C.

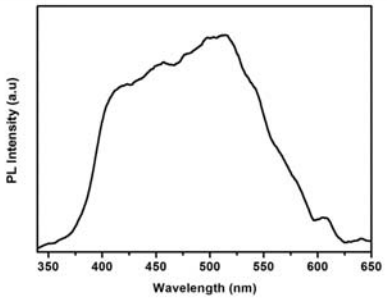

Figure 7. Room temperature photoluminescence (PL) spectrum of ethylenediamine assisted solvo-hydrothermally grown ZnS microspheres synthesised at 180°C.

ZnS is a wide band gap (3.7 eV) semiconductor, which is expected to absorb only UV radiation (41). The UV–visible absorbance spectrum (Fig. 6) recorded from the ZnS microspheres shows that the absorption edge was slightly shifted to 330–428 nm as compared with that reported previously in the range 330–380 nm (42). Maximum absorption was observed at 342 nm with a shift of the order of 7 nm with respect to bulk (335 nm corresponding to the band gap of 3.7 eV), which is attributed to the nanoparticle nature of the sample (43).

The band gap of the prepared ZnS microspheres was calculated using the Kubelka–Munk relationship and was found to be 3.45 eV, which is blue shifted compared with that of the bulk (3.7 eV at room temperature) (44). The blue shift in the band gap also confirmed that the microspheres were made of nanoparticles, in agreement with the TEM and XRD results.

It has been reported previously that hollow ZnS microspheres with rough surface features have PL emission peaks at 3.02 (412 nm) and 2.34 eV (532 nm) (45). But in the present sample, the room temperature photoluminescence spectrum showed a broad emission peak in the wavelength region 380–580 nm (Fig. 7). Hafeez *et al.* (41) reported that visible light emission in ZnS nanostructures is due to intrinsic defects such as Zn and S vacancies. Usually ZnS shows a blue emission under UV light excitation, which is attributed to the surface V_{S^-}, or internal V_S-related emission arising from the recombination between V_S donor levels and the valence band. The V_S–V_{Zn} transition in ZnS gives a greenish-yellow band in the PL spectrum (46). The broad emission from the sample may be related to increase in carrier concentration, which is evident from the appearance of the intense Raman band at 257 cm^{-1}. The near band edge (NBE) emission from the deep levels of Zn^{2+} vacancies, S^{2-} interstitials and dislocations (390–400 nm) are almost absent in the room temperature PL spectrum of the ZnS microsphere, but broad emission arises as a result of the blue (associated with the Zn^{2+} and S^{2-} vacancy trapped emission), green (due to the dopants or impurity atom contributed defect level emission) and orange emissions, attributed to deep levels (47). The presence of Zn and S vacancies, however, depends strongly on the growth process (41). The use of the acetonitrile as a solvent for the growth contributed to the increase in population of sulphur vacancies and consequently more carriers (35). The appearance of a broad visible emission from the sample is probably due to overlapping of blue and greenish-yellow emissions.

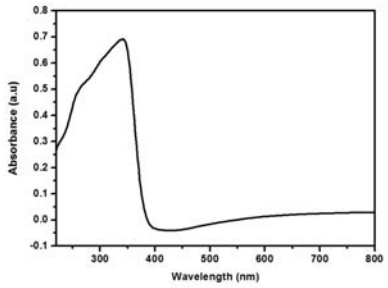

Figure 6. UV–vis absorbance spectrum of ethylenediamine assisted solvo-hydrothermally grown ZnS microspheres synthesised at 180°C.

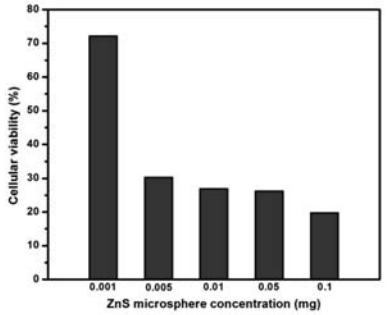

Figure 8. Cytotoxicity study of ethylenediamine assisted solvo-hydrothermally grown ZnS microspheres synthesised at 180°C in L929 fibroblast cell lines.

Copyright © 2015 John Wiley & Sons, Ltd.

LUMINESCENCE
The Journal of Biological and Chemical Luminescence

Cytotoxicity and hemocompatibility

The cytotoxicity of ZnS microspheres was investigated by analysing cell viability of the system on MCF7 cells by the MTT assay method. Different concentrations of ZnS microspheres, such as 0.1, 0.01, 0.05, 0.005 or 0.001 mg/mL, were added to the cells and cells were incubated for 24 h. On removal of the medium, MTT (0.2 mg/mL) was added to each experiment well and the well incubated for 3 h. After removal of MTT, dimethyl sulfoxide was added to the experimental medium to dissolve formazan and the wells were incubated for 30 min. The optical absorbance was quantified by measuring the intensity of the peak at 570 nm using a microplate reader (Biotech, Power wave XS, USA). It is interesting to note that at a concentration of 0.001 mg/mL ZnS microspheres the cells were 72% viable, indicating the non-cytotoxic nature of the ZnS microspheres (Fig. 8). But the addition of higher doses (0.005, 0.01, 0.05 or 0.1 mg) of the ZnS microspheres resulted in comparatively more cell death, therefore the microspheres are cytotoxic to a certain extent.

Similarly, to measure haemocompatibility, aggregation studies with ZnS microspheres and human blood cells were performed (Fig. 9). For this experiment red blood cell (RBC) aggregation analysis was carried out with the RBC isolated from human blood. The experimental ZnS samples were incubated along with RBC at 37°C. Interestingly, morphology was found to be normal after inoculation, showing no aggregation. Similarly biocompatibility of white blood cells (WBCs) was investigated by WBC aggregation analysis. The samples were inoculated with WBC isolated from human blood for 30 min at 37°C (Fig. 9). After incubation, there was no aggregation of the cells, as seen from phase-contrast microscopic images of ZnS microsphere-treated WBC cells. A blood platelets aggregation study was also done with the above protocol and the morphologies of the platelets were similar, without any change after inoculation of the cells with the ZnS microspheres used in the present investigation. The present biocompatibility study of the samples shows that the S-H grown ZnS microspheres are both cytocompatible and haemocompatible and can be used for imaging these cells.

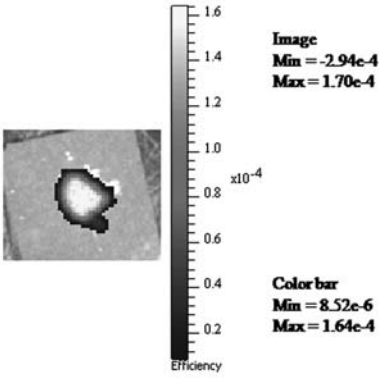

Figure 10. *In vitro* imaging study of ethylenediamine assisted solvo-hydrothermally grown ZnS microspheres synthesised at 180°C with the XENOGEN-IVIS system. Colour bar indicates imaging efficiency value.

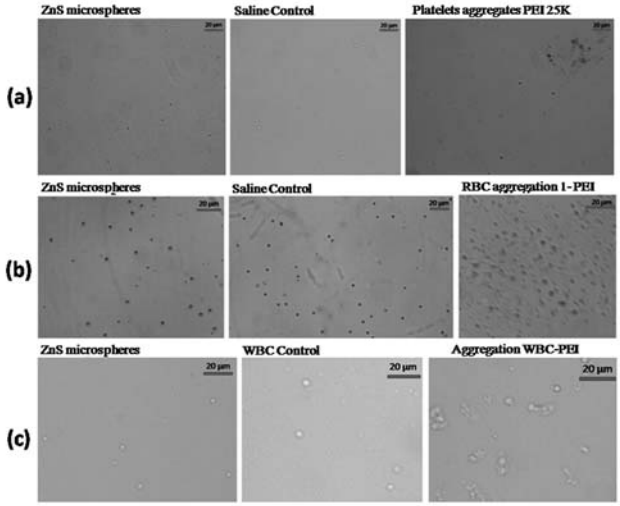

Figure 9. Haemocompatibility aggregation study of ethylenediamine assisted solvo-hydrothermally grown ZnS microspheres synthesised at 180°C in L929 fibroblast cell lines. (a) Platelets; (b) red blood cells; (c) white blood cells.

 Copyright © 2015 John Wiley & Sons, Ltd.

LUMINESCENCE
The Journal of Biological and Chemical Luminescence

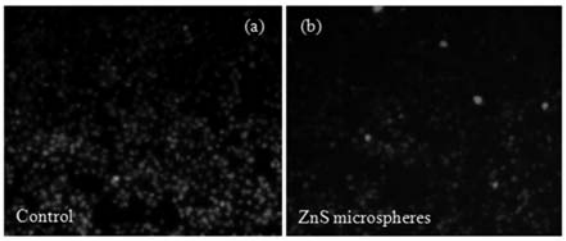

Figure 11. *In vivo* imaging study of ethylenediamine assisted solvo-hydrothermally grown ZnS microspheres synthesized at 180°C in L929 fibroblast cell lines. (a) Control; (b) ZnS microspheres.

Emission and imaging studies

The imaging efficiency of ethylenediamine assisted solvo-hydrothermally grown ZnS microspheres was evaluated using the XENOGEN-IVIS spectrum optical imaging system and is shown in Fig. 10. The sample showed good fluorescence emission as understood from the adjacent colour bar in Fig. 10, which is in good agreement with previously described PL results.

For investigating the emission properties of the ZnS microspheres for cellular imaging, the material was incubated with L929 fibroblast cell lines for 3 h. The fluorescence microscopic images (Fig. 11b) show the emission from the ZnS microspheres. The partial internalization of the materials would have taken place due to endocytosis or the enhanced permeability and retention (EPR) effect of the cells. The size of the fibroblast cells used in this study was in the range 5–10 μm to facilitate particle uptake.

Conclusion

ZnS microspheres with an average diameter 3.85 μm grown by the solvo-hydrothermal (S-H) method and using ethylenediamine surfactant exhibited a broad visible PL emission from 380–580 nm. This broad visible PL emission was attributed to the increase in carrier concentration as understood from the presence of an intense Raman band at 257 cm^{-1}. The present cytocompatible and haemocompatible ZnS microspheres can be used for bioimaging applications. These bio-friendly ZnS microspheres with a broad visible emission have potential applications in the fields of drug targeting, bio-separation, diagnostic analysis and for the production of white light sources.

Acknowledgements

P. Sajan thanks the University Grants Commission, Government of India for providing his Rajiv Gandhi National fellowship. The authors acknowledge Professor M K Jayaraj, Nanophotonic and Optoelectronic Devices Laboratory, Department of Physics, CUSAT, for providing photoluminescence and Raman measurements under the Department of Science and Technology Nano Mission Initiative Programme.

References

1. Lu SH, Chen TF, Wang AJ, Wu ZL, Wang YS. Lattice and optical property evolution of ultra-small ZnS quantum dots grown from a single-source precursor. Appl Surf Sci 2014;299:116–22.
2. Sookhakian M, Amin YM, Basirun WJ. Hierarchically ordered macro-mesoporous ZnS microsphere with reduced graphene oxide supporter for a highly efficient photodegradation of methylene blue. Appl Surf Sci 2013;283:668–77.
3. Yu X, Wan J, Shan Y, Chen K, Han X. A facile approach to fabrication of bifunctional magnetic-optical Fe_3O_4@ZnS microspheres. Chem Mater 2009;21:4892–8.
4. Zhong SL, Xu R, Zhang LF, Qu WG, Gao GQ, Wu XL, et al. Terbium-based infinite coordination polymer hollow microspheres: preparation and white-light emission. J Mater Chem 2011;21:16574–80.
5. Zhang Y, Pan C, Zhang Y, He W. Self-template hydrothermal synthesis ZnS microspheres. Cryst Res Technol 2011;46:718–22.
6. Muruganandham M, Amutha R, Sillanpää M. Reagents for ZnS hierarchical and non-hierarchical porous self-assembly. ACS Appl Mater Inter 2010;2:1817–23.
7. Wu Q, Cao H, Zhang S, Zhang X, Rabinovich D. Generation and optical properties of monodisperse wurtzite-type ZnS microspheres. Inorg Chem 2006;45:7316–22.
8. Muruganandham M, Amutha R, Repo E, Sillanpää M, Kusumoto Y, Al-Mamun MA. Controlled mesoporous self-assembly of ZnS microsphere for photocatalytic degradation of methyl orange dye. J Photochem Photobiol A 2010;216:133–41.
9. Zhao JG, Zhang HH. Hydrothermal synthesis and characterization of ZnS hierarchical microspheres. Superlattice Microst 2012;51:663–7.
10. Jian D, Gao Q, Li N, Ruan M. Preparation of cadmium selenide nanocrystals through an ultrasonic activation double-phase approach at room temperature. Mater Lett 2007;61:4471–3.
11. Jayasimhadri M, Ratnam BV, Jang K, Lee HS, Yi SS, Jeong JH. Conversion of green emission into white light in Gd_2O_3 nanophosphors. Thin Solid Films 2010;518:6210–3.
12. Lorbeer C, Mudring AV. White-light-emitting single phosphors via triply doped laf_3 nanoparticles. J Phys Chem C 2013;117:12229−38.
13. Nakamura S, Mukai T, Senoh M. Candela-class high-brightness InGaN/AlGaN double-heterostructure blue-light-emitting diodes. Appl Phys Lett 1994;64:1687–9.
14. Piao XQ, Horikawa T, Hanzawa H, Machida K. Photoluminescence properties of $Ca_2Si_5N_8:Eu^{2+}$ nitride phosphor prepared by carbothermal reduction and nitridation method,. Chem Lett 2006;35:334–5.
15. Dutta DP, Manoj N, Tyagi AK. White light emission from sonochemically synthesised rare earth doped ceria nanophosphors. J Lumin 2011;131:1807–12.
16. Maio JRD, Kokuoz B, Ballato J. White light emissions through down-conversion of rare-earth doped LaF_3 nanoparticles. Opt Express 2006;14:11412–7.
17. Yang CC, Lin CM, Chen YJ, Wu YT, Chuang SR, Liu RS, et al. Highly stable three-band white light from an InGaN-based blue light-emitting diode chip precoated with (oxy)nitride green/red phosphors. Appl Phys Lett 2007;90:123503–5.
18. Bruno A, Borriello C, Luccio TD, Nenna G, Sessa L, Concilio S, et al. White light-emitting nanocomposites based on an oxadiazole–carbazole copolymer (POC) and InP/ZnS quantum dots. J Nanopart Res 2013;15:2085–95.
19. Zhang C, Ma P, Li C, Li G, Huang S, Yang D, et al. Controllable and white upconversion luminescence in $BaYF5:Ln^{3+}$ (Ln=Yb,Er, Tm) nanocrystals. J Mater Chem 2011;21:717–23.

 Copyright © 2015 John Wiley & Sons, Ltd.

20. Lu X, Yang J, Fu Y, Liu Q, Qi B, Lu C, et al. White light emission from Mn^{2+} doped ZnS nanocrystals through the surface chelating of 8 hydroxyquinoline-5-sulfonic acid. Nanotechnology 2010;21:115702–802.
21. Wang C, Hu B, Li W, Yi H. Luminescence properties of ZnS/porous Si composites. Optik 2014;125:554–6.
22. Zagorovsky K, Chan WC. Bioimaging: illuminating the deep. Nat Mater 2013;12:285–7.
23. Chen D, Huang P. Highly intense upconversion luminescence in Yb/Er: $NaGdF_4$@$NaYF_4$ core–shell nanocrystals with complete shell enclosure of the core. Dalton Trans 2014;43:11299–304.
24. Chen D, Chen Y, Lu H, Ji Z. A bifunctional Cr/Yb/Tm:$Ca_3Ga_2Ge_3O_{12}$ phosphor with near-infrared long-lasting phosphorescence and upconversion luminescence. Inorg Chem 2014;53:8638−45.
25. Muhr V, Wilhelm S, Hirsch T, Wolfbeis OS. Upconversion nanoparticles: from hydrophobic to hydrophilic surfaces. Acc Chem Res 2014;47:3481−93.
26. Sun L, Liu T, Qiu Y, Liu J, Shi L, Wolfbeis OS. Direct formation of mesoporous upconverting core-shell nanoparticles for bioimaging of living cells. Microchim Acta 2014;181:775–81.
27. Wei Z, Sun L, Liu J, Zhang JZ, Yang H, Yang Y, et al. Cysteine modified rare-earth up-converting nanoparticles for *in vitro* and *in vivo* bioimaging. Biomaterials 2014;35:387–92.
28. Durgadas CV, Sreenivasan K, Sharma CP. Bright blue emitting CuSe/ZnS/silica core/shell/shell quantum dots and their biocompatibility. Biomaterials 2012;33:6420–9.
29. Wang G, Su X. The synthesis and bio-applications of magnetic and fluorescent bifunctional composite nanoparticles. Analyst 2011;136:1783–98.
30. Hsieh JM, Ho ML, Wu PW, Chou PT, Tsaib TT, Chi Y. Iridium-complex modified CdSe/ZnS quantum dots; a conceptual design for bifunctionality toward imaging and photosensitization. Chem Commun 2006;6:615–7.
31. Ruan S, Wan J, Fu Y, Han K, Li X, Chen J, et al. PEGylated fluorescent carbon nanoparticles for noninvasive heart imaging. Bioconjugate Chem 2014;25:1061−8.
32. Scocioreanu M, Baibarac M, Baltog I, Pasuk I, Velula T. Photoluminescence and Raman evidence for mechanico-chemical interaction of polyaniline-emeraldine base with ZnS in cubic and hexagonal phase. J Solid State Chem 2012;186:217–223.
33. Kumar SS, Khadar MA, Dhara SK, Ravindran TR, Nair KGM. Photoluminescence and Raman studies of ZnS nanoparticles implanted with Cu^+ ions. Nucl Instrum Meth B 2006;251:435–40.
34. Sajan P, Bushiri JM, Vinod R. Boosted UV emission at 349 nm from mesoporous ZnS. Appl Phys A-Mater 2013;113:321–5.
35. Sajan P, Vinod R, Bushiri JM. High luminescent yield from Mn doped ZnS at yellow–orange region and 367 nm. J Lumin 2015;158:110–5.
36. Bhirud A, Chaudhari N, Nikam L, Sonawane R, Patil K, Baeg JO, et al. Surfactant tunable hierarchical nanostructures of $CdIn_2S_4$ and their photohydrogen production under solar light. Int J Hydrogen Energ 2011;36:11628–39.
37. Bushiri MJ, Gopakumar V, Vaidyan VK. Blue shift and intensity enhancement in visible emission spectrum of c-axis oriented spray pyrolytically grown nanocrystalline ZnO thin films. Surf Rev Lett 2008;15:551–6.
38. Chen ZW, Lai JKL, Shek CH. Insights into microstructural evolution from nanocrystalline SnO_2 thin films prepared by pulsed laser deposition. Phys Rev B 2004;70:165314–20.
39. Arndt D, Zielasek V, Dreher W, Bäumer M. Ethylene diamine-assisted synthesis of iron oxide nanoparticles in high-boiling polyols. J Colloid Interf Sci 2014;417:188–98.
40. Murugadoss G, Ramasamy V. Synthesis, effect of capping agents and optical properties of manganese-doped zinc sulphide nanoparticles. Luminescence 2013;28:69–75.
41. Hafeez M, Rehman S, Manzoor U, Khan MA, Bhatti AS. Catalyst driven optical properties of the self–assembled ZnS nanostructures. Phys Chem Chem Phys 2013;15:9726–34.
42. Li Y, Lu A, Wang C, Wu X. Characterization of natural sphalerite as a novel visible light-driven photocatalyst. Sol Energ Mat Sol C 2008;92:953–9.
43. Peng L, Wang Y. Effects of the template composition and coating on the photoluminescence properties of ZnS:Mn nanoparticles. Nanoscale Res Lett 2010;5:839–45.
44. Murugadoss G, Kumar MR. Synthesis and optical properties of monodispersed Ni^{2+}-doped ZnS nanoparticles. Appl Nanosci 2014;4:67–75.
45. Luo Y, Duan G, Ye M, Zhang Y, Li G. Poly(ethyleneglycol)-mediated synthesis of hollow ZnS microspheres. J Phys Chem C 2008;112:2349–52.
46. Song HQ, Qing DD, Ping XJ, Song ZX, Min ZH, Lan L. White emitting ZnS nanocrystals: synthesis and spectrum characterization. Chinese Phys Lett 2010;27:5- 057306-4.
47. Park S, Jin C, Kim H, Hong C, Lee C. Enhanced violet emission from ZnS nanowires annealed in an oxygen atmosphere. J Lumin 2012;132:231–5.

 Copyright © 2015 John Wiley & Sons, Ltd.